



PhD-FSTM-2023-138

The Faculty of Science, Technology and Medicine

DISSERTATION

Defence held on 30/11/2023 in Esch-sur-Alzette

to obtain the degree of

DOCTEUR DE L'UNIVERSITÉ DU LUXEMBOURG
EN PHYSIQUE ET SCIENCE DES MATÉRIAUX

by

Saba Tabean

Born on 21 March 1991 in Miandoab (Iran)

EXPLORING CORRELATIVE MICROSCOPY METHODOLOGIES FOR ENHANCED IMAGING AND ANALYSIS WITH HELIUM ION MICROSCOPE

Dissertation defence committee

Dr Tom Wirtz, dissertation supervisor

Head of Unit, Luxembourg Institute of Science and Technology

Dr Santhana Eswara Moorthy, dissertation Co-supervisor

Senior Researcher, Luxembourg Institute of Science and Technology

Prof. Dr Alex Redinger, Chairman

Professor, Université du Luxembourg

Dr Sascha Sadewasser

Group Leader, International Iberian Nanotechnology Laboratory

Prof. Dr. Joachim Mayer, Vice-Chairman

Rector's Delegates, RWTH Aachen University

Abstract

Correlative microscopy plays a vital role in scientific research and material analysis by offering a valuable solution to integrate diverse imaging techniques, resulting in a comprehensive understanding of complex samples. Combining Secondary Electron (SE), Scanning Transmission Ion Microscopy (STIM), and Secondary Ion Mass Spectrometry (SIMS) in one apparatus using a He^+/Ne^+ ion beam, we can establish meaningful connections between the morphology, crystal structure, and chemistry of a given sample on a nanometre scale. This approach delves deep into the complexities of material characteristics such as semiconductors, biological processes, etc. However, one of these three correlative approaches, STIM, has potential applications that still need to be studied and compared to similar existing methods.

Before delving into STIM imaging, we initiated our study by examining ion-induced damage effects before and during imaging on the sample. For this aim we performed preliminary experiments related to Ga^+ and He^+ ion irradiation on thin lamellae of silicon and aluminium. Depending on the experimental conditions, we investigated the top and bottom surface morphologies, as well as a structural transformation from crystalline to amorphous material. Subsequently, to understand STIM applications, we compared STIM imaging with existing comparable imaging techniques such as Transmission Kikuchi Diffraction (TKD), Backscattered Electrons (BSE), and SE. Additionally, we expanded the capabilities of STIM imaging by conducting Time of Flight (ToF) measurements using a separate apparatus to explore the potential for complementary studies within the STIM technique.

Towards the conclusion of our research, we focused on the materials science applications of ion beam microscopy techniques namely SE, SIMS and STIM techniques. Our initial focus was on studying dopant profiling by analysing SE-generated contrast with a helium ion beam. In the subsequent stage of our correlative approach, we established connections between SIMS, SE imaging, and other techniques to investigate perovskite solar cell materials. In the final segment of our correlative approach, we attempted to correlate STIM with SIMS. While this endeavour had limited success, it did provide valuable insights in that direction.

Acknowledgements

Like all scientific endeavours, this thesis owes its completion to the unwavering support of numerous individuals. First and foremost, I extend my heartfelt gratitude to my supervisors. Dr Tom Wirtz, for entrusting me with this project, offering invaluable guidance, and pushing me to evolve as a scientist, and Dr Santhana Eswara Moorthy for the support, his availability for discussions, and his consistent feedback throughout my four-year journey toward a PhD. I also appreciate the valuable input and guidance from Prof. Dr Alex Redinger during our annual thesis committee meetings.

Special recognition is due to Olivier De Castro, Jean-Nicolas Audinot, Antje Biesemeier, Tatjana Taubitz, and Cherif Boubacar Coulbary, whose unlimited support in the lab was influential in my project.

I sincerely thank Michael Mousley, whose scientific expertise and work on the Galileo measurements greatly enriched our project discussions.

I am also indebted to Patrick Philipp and Gregoire Defoort for their generous assistance with the SDTrimSP simulations.

Gratitude extends to Quentin Jeangros, Christian Michael Wolff, Xin Yu Chin, Deniz Turkey, and Mustafa Othman from PVLab at EPFL University, who graciously hosted me for a secondment involving perovskite solar cells.

Furthermore, I appreciate the collaboration with Dustin Andersen and Daniel Primetzhofer's team for their contributions to MEIS experiments in Uppsala.

My heartfelt appreciation extends to current and former LIST colleagues for their engaging discussions and friendship, making these past four years more enjoyable.

Lastly, but most importantly, I want to express my deepest gratitude to my family and close friends, whose unwavering support sustained me through the challenges of these four years pursuing my PhD.

Acronyms

B

Backscattered Electron
(BSE)
Best Imaging Voltage
(BIV)
Binary Collision Approximation
(BCA)
Bright field
(BF)
Binary Collision Approximation
(BCA)

C

Confocal Laser Scanning Microscope
(CLSM)

D

Dark field
(DF)
Delay Line Detector
(DLD)
detection limit
(DL)
Direct current
(DC)

E

Electron Backscatter Diffraction
(EBSD)
Energy Dispersive X-ray Spectroscopy
(EDS)
Everhart-Thornley
(ET)
Electron Transport Layer
(ETL)
External Quantum Efficiency
(EQE)

F

Focused Ion Beam
(FIB)
2,3,4,5,6-pentafluorobenzylphosphonic acid
(FBPAC)

G

Gas Field Ion Source
(GFIS)
Grazing-incident wide-angle X-ray scattering
(GIWAXS)

H

Helium Ion Microscopy/Microscope
(HIM)
Hole-transport layer
(HTL)

I

Inverse pole figure
(IPF)
Ion Beam Analysis
(IBA)
Ion induced Secondary Electron
(iSE)
Indium tin oxide
(ITO)

J

Photocurrent density
(J_{sc})

L

Liquid Metal Ion Source
(LMIS)

M

Micro Channel Plate
(MCP)
Molecular Dynamics
(MD)
Medium Energy Ion Scattering Spectroscopy
(MEIS)
[4-(3,6- dimethyl-9H-carbazol-9-yl)butyl]phosphonic acid
(Me-4PACz)

P

parts per billion
(ppb)
photovoltaic
(PV)
power conversion efficiency
(PCE)
Metal-halide perovskite solar cells
(PSCs)

Q

Quasi-Fermi level splitting
(QFLS)

R

Region of Interest
(ROI)
Rutherford Backscattered Ions
(RBI)
Rutherford backscattering spectrometry's
(RBS)
Recoil interaction approximation
(RIA)

S

Selected area electron diffraction
(SAED)
Scanning Electron Microscopy/Microscope
(SEM)
Scanning Field Ion Microscope
(SFIM)
Scanning Transmission Electron Microscope-Electron
Energy Loss Spectroscopy
(STEM-EELS)
Scanning Transmission Ion Microscopy
(STIM)
STIM ion energy loss spectroscopy
(STIM-IELS)
Secondary Electron
(SE)
Stacking fault
(SF)
Secondary Ion Mass Spectrometry/Spectrometer
(SIMS)

Secondary Ions
(SIs)
Sputtering Yield
(SY)
Stopping and Range of Ions in Matter
(SRIM)

T

Time-of-Flight
(ToF)
Time-of-flight medium energy ion scattering
(ToF-MEIS)
Transmission Electron Microscopy/Microscope
(TEM)
Transmission Kikuchi Diffraction
(TKD)
Transport of Ions in Matter
(TRIM)

U

ultra-high vacuum
(UHV)
ultraviolet Photoelectron Spectroscopy
(UPS)

V

Open -circuit voltage
(V_{oc})

X

X-ray photoelectron spectroscopy
(XPS)

Preface

This thesis was conducted at the Materials Research and Technology Department of the Luxembourg Institute of Science and Technology (LIST), with a connection to the Doctoral Program in Physics and Materials Science at the University of Luxembourg. The supervision was provided by Dr. Tom Wirtz and Dr. Santhana Eswara Moorthy. The thesis supervision committee consisted of Dr. Tom Wirtz, Dr. Santhana Eswara Moorthy, and Prof. Dr. Alex Redinger. This PhD project was funded by the Luxembourg National Research Fund (FNR) by the grants PRIDE17/12246511/PACE. The research outlined in this thesis has been published in the following journals and showcased at various conferences.

Publication list

1. C N Shyam Kumar; **Saba Tabean**; Audrey Morisset; Philippe Wyss; Mario Lehmann; Franz-Josef Haug; Quentin Jeangros; Aïcha Hessler-Wyser; Nathalie Valle; Tom Wirtz. **Evaluation of secondary electron intensities for dopant profiling in ion implanted semiconductors: a correlative study combining SE, SIMS and ECV methods.** Semiconductor Science and Technology 2021. DOI: [10.1088/1361-6641/ac0854](https://doi.org/10.1088/1361-6641/ac0854).
2. **Saba Tabean**; Michael Mousley; Christoph Pauly; Olivier De Castro; Eduardo Serralta; Nico Klingner; Frank Mücklich; Gregor Hlawacek; Tom Wirtz; Santhana Eswara. **Quantitative nanoscale imaging using transmission He ion channelling contrast: Proof-of-concept and application to study isolated crystalline defects.** Ultramicroscopy. 2022, 233. DOI: [10.1016/j.ultramic.2021.113439](https://doi.org/10.1016/j.ultramic.2021.113439).
3. Michael Mousley; **Saba Tabean**; Olivier Bouton; Quang H Hoang; Tom Wirtz; Santhana Eswara. **Scanning Transmission Ion Microscopy Time-of-Flight Spectroscopy Using 20 keV Helium Ions.** *Microscopy and Microanalysis*, 2023, 29. DOI: [10.1093/micmic/ozac049](https://doi.org/10.1093/micmic/ozac049)
4. Xin Yu Chin; Deniz Turkay; Julian A. Steele; **Saba Tabean**; Santhana Eswara; Mounir Mensi; Peter Fiala; Christian M. Wolff; Adriana Paracchino; Kerem Artuk et al.

Interface passivation for 31.25%-efficient perovskite/silicon tandem solar cells.
Science, 2023, 381. DOI: [10.1126/science.adg0091](https://doi.org/10.1126/science.adg0091).

Conference participation

1. **Microscopy and Microanalysis (M&M) virtual Meeting**, online, August 2021: oral presentation
2. **European conference on Surface Science (ECOSS) 2020**, Luxembourg, August 2022: oral presentation
3. **MESSENA YSC 2021**, Luxembourg, June 2021: oral presentation
4. **PACE YSC 2022**, Luxembourg, October 2022: conference organizer and oral presentation
5. **International conference on atomic collisions in solids international symposium on swift heavy ions in matter (ICACS and SHIM 2022)**, Helsinki (Finland), June 2022: oral presentation
6. **International Conference on Materials for Advanced Technologies (ICMAT 2023)**, Singapore, June 2023: oral presentation

Table of Contents

Abstract.....	3
Acknowledgements.....	4
Acronyms	5
Preface	7
1 Chapter 1: Introduction and Background	11
1.1 State of the art 1: Physics background on ion beam irradiation effects and imaging contrasts	11
1.1.1 Introduction to gallium (Ga^+) and helium (He^+) ion beam irradiation in low keV energy for imaging purposes	11
1.1.2 Image formation mechanisms, contrasts and measurements using He^+ ions FIB.....	13
1.2 State of the art 2: Technical challenges background on correlative microscopy approaches.....	31
1.2.1 npSCOPE	33
1.2.2 Galileo.....	45
1.3 Problem statement and objectives of the thesis	48
2 Chapter 2: Experimental.....	51
2.1 Nanofab HIM-SIMS	51
2.2 Scios.....	51
2.3 Confocal Laser Scanning Microscope (CLSM)	51
2.4 SDTrimSP simulations	52
2.5 SRIM (Stopping and Range of Ions in Matter) and CASINO.....	53
2.6 TKD (Transmission Kikuchi diffraction)	54
2.7 ToF-MEIS (Time-of-flight medium-energy ion scattering).....	55
2.8 Electrochemical Capacitance-Voltage (ECV)	57
2.9 X-ray photoelectron spectroscopy (XPS).....	58
2.10 J-V curve measurements	58
3 Chapter 3: Irradiation damages investigations with Ga^+ and He^+ ion beams.....	60
3.1 Sample preparation workflow	61
3.2 Results and Discussion.....	62
3.2.1 Focused Ga^+ ion beam exposure.....	62
3.2.2 Focused He^+ ion beam exposure.....	75
3.3 Conclusions.....	79
4 Chapter 4: He^+ ion Channelling Contrast with STIM imaging.....	82
4.1 Sample preparation workflow and imaging parameters.....	82
4.2 Results and Discussion.....	83
4.2.1 STIM and SE imaging mode comparison	83
4.2.2 STIM, TKD and high-resolution BSE imaging mode comparison.....	86
4.2.3 STIM imaging resolution assessment.....	90

4.2.4	STIM imaging contrast variation with magnification.....	93
4.3	Conclusions.....	95
5	Chapter 5: Energy loss contrast in STIM imaging mode	97
5.1	Sample preparation workflow	97
5.2	Results and Discussion.....	99
5.2.1	ToF-MEIS results on Ga implanted Si	100
5.2.2	Galileo experiments	104
5.3	Conclusions.....	108
6	Chapter 6: Correlative approaches using HIM.....	110
6.1	Case study 1: Correlative study of SE, SIMS for dopant profiling in ion implanted semiconductors ..	110
6.1.1	Sample preparation workflow and imaging parameters	110
6.1.2	Results and Discussion	111
6.1.3	Conclusions from Case Study 1	116
6.2	Case study 2: A correlative SE and SIMS approach for perovskite crystallization kinetics and microstructure.....	117
6.2.1	Sample preparation workflow.....	117
6.2.2	Results and Discussion	118
6.2.3	Conclusions from Case Study 2	122
6.3	Case study 3: Correlative approach for cesium-formamidine metal-halide perovskites.....	123
6.3.1	Sample preparation workflow.....	123
6.3.2	Results and discussion	125
6.3.3	Conclusions.....	131
7	Chapter 7: Future work	132
7.1	Preliminary results.....	132
7.2	Conclusions.....	137
8	Annex	139
8.1	Galileo prototype.....	139
8.2	SIMS analysis	139
8.3	Schematic view of perovskite/crystalline-Si.....	140
8.4	QFLS and XPS.....	141
8.5	Current -voltage (J-V).....	142
8.6	Photocurrent map	143
8.7	C-AFM map.....	143
8.8	Stability and performance	144
9	References	145

1 Chapter 1: Introduction and Background

1.1 State of the art 1: Physics background on ion beam irradiation effects and imaging contrasts

1.1.1 Introduction to gallium (Ga^+) and helium (He^+) ion beam irradiation in low keV energy for imaging purposes

A focused ion beam (FIB) is a powerful nanofabrication and analytical technique used to precisely mill, etch, or pattern materials at the nanoscale. It is also utilized for imaging and analysing samples with exceptional spatial resolution[1]. There is a wide variety of fields for FIB applications. Ga^+ FIB is one of the widely used ion beams in FIB processes specially for sample preparation purposes. However, FIB-induced artifacts due to the radiation's intense surface damage after the ion irradiation can hinder analysis and produce misleading results. During the ion irradiation process, the projectile ions penetrate the material's surface to a specific depth (for instance, 50 kV Ga^+ ions can penetrate deep in silicon (Si) and create a damage layer of up to 45 nm with grazing incidence angle irradiation). This penetration depth depends on the incidence angle and projectile energy, resulting in amorphization, dislocations induced by ion implantation and atomic mixing near the surface area. Also, Ga^+ implantation causes lattice stress and swelling of the material below the surface which created distortion upwards. Accordingly, artifacts due to the compositional changes are possible[2]. Conventional Ga^+ FIB processing is known to change the crystal structure like amorphization of Si[3] and Al[4] and phase changes[5],[6]. Other artifacts such as the segregation of implanted Ga^+ to the grain boundaries of Al has also been reported. In this case, few hundred-nanometre gallium droplets can form while using high current Ga^+ ion beams[7].

The image quality in high-resolution Transmission Electron Microscopy (TEM), Scanning Transmission Ion Microscopy (STIM) or Secondary ion mass spectrometry (SIMS) imaging could be negatively affected due to the FIB-induced artifacts. TEM samples produced by Xe ion FIB milling beam compared to Ga^+ FIB milling produced samples show cleaner surface and fewer nanoparticle artifacts due to the re-deposition with Xe preparation in comparison with Ga^+ ion[8]. In a study[9], a thickness variation in the SiN_x layer was observed due to the

artifact produced by FIB sample preparation which could cause misinterpretation as a result of FIB milling process and intermixing of the layers[10], [11].

While ion irradiation results in radiation damage, it can also be used beneficially. For instance, it has been used to adjust different properties of materials specially semiconductors to improve the mechanical[12], [13], optical[10], [14], [15] electrical[10], [15], [16] and chemical properties[17],[18] , as well as nanofabrication[15], [17], [19], [20].Therefore, matter-projectile ion interaction studies will also help improve these applications. For example, designing material to be tolerant under radiation in nuclear reactors[21],[22]. Regarding producing nanostructured deformations, the FIB plays a critical role. A well-known example is the Ga⁺ FIB, which has been used for surface deformations for example surface hardening[12], wire straightening[23], and other nanostructure formations such as nanowire growth applications[24].

Another significant ion beam within our study scope is the helium ion beam. He⁺ ions are commonly employed as an imaging technique in Helium ion microscopy (HIM), which is a FIB instrument and will be discussed later in section (1.2.1). Generally, the distribution of FIB damage effects depends on parameters such as the penetration range of the ions in the material, the sputtering yield, and ion solubility in the material. When traversing through a material, He⁺ ions lose energy due to the electronic interactions with minimal displacement of sample atoms in comparison with Ga⁺ ions. Thus, the primary factor governing stopping power differs for helium ions, where electronic stopping power dominates, and gallium ions, where nuclear stopping power takes precedence. The stopping power of 35keV He⁺ ions is (11.6 eV/Å in c-Si sample) approximately 12 times lower than Ga⁺ ions (~140 eV/Å in c-Si sample) with the same kinetic energy, therefore ion ranges , and radial scattering of He⁺ are roughly 12 times higher than for Ga⁺ in the material[25]. For C and Si material irradiated by He⁺ and Ga⁺, He⁺ ions present two orders of magnitude lower sputtering yield in comparison with Ga⁺ ions[25]. Moreover, after a certain amount of exposure of Ga⁺ ions, sputtering causes continuous surface recession, resulting in a steady-state Ga⁺ ion implantation profile[1]. Whereas due to the closed shell electron configuration of He⁺ ions, repulsive interactions occur between He⁺ and the target material, which will result in the limited solubility equilibrium within the host material[26]. As a result of low equilibrium solubility, the implanted He⁺ ions produce He gas bubbles with identical dimensions to those of He

exposed region[25]. The 20 keV He⁺ ion concentration peak in Silicon is around 200 nm deep, while the vacancy distribution extends to 100 nm depth, at high fluences like 2×10^{16} ion/cm². The results showed high quantity of extended defects in 130 nm deep, but no bubbles observed. This agrees with the estimations made by Stopping and Range of Ions in Matter (SRIM) calculations for Stopping and Range of Ions in Matter/Transport of Ions in Matter[27]. In summary, for He⁺ ion beam energies on the order of keV, the damage profile resulting from He⁺ ion implantation in silicon, along with the subsequent recovery kinetics, can be categorized into domains of high and low fluence. A dose of around 1×10^{16} ion/cm² is required to switch from low to high dose regimes[28]. In the high enough fluence domain, growing bubbles cause substantial morphological alterations such as surface swelling. By "high enough fluence," we are referring to cases where the ion dose exceeds 10^{17} ions/cm²[27], [29]. Furthermore, the target material could experience morphological modification without reaching steady state radiation damage profile. Also, despite Ga⁺ ions, He⁺ ions escape by scattering and diffusing from the irradiated region into the surrounding Internal surface which has been created due to the He⁺ bubbles. This behaviour of He⁺ ions result in both internal and surface damage to the crystal structure of the target. Details of the irradiation effects due to the FIB He⁺ ions were already investigated for Si[27], [30], [31], Cu[29], Ni-Mo/Si[32], and graphene[33].

1.1.2 Image formation mechanisms, contrasts and measurements using He⁺ ions FIB

He⁺ ion beam implementation for imaging and microanalysis emphasizes the importance of understanding beam interactions with matter that discussed in the previous section. In the next sub sections, we will discuss the imaging contrast induced by He⁺ ions beam. In the following section we will discuss the different Secondary Electron (SE) contrasts induced by He⁺ ion beam and make a comparison with the SE contrast generated by electron beam.

1.1.2.1 Secondary Electron (SE) and ion induced Secondary Electron (iSE)

The utilization of SE imaging stands out as the most adaptable and broadly relevant imaging method using charged particles. SEs are emitted from the sample with energies below 50 eV, while Backscattered Electron (BSE) have higher energies. Also, SEs produced by electrons/ ions can be excited both directly by the primary beam and indirectly by backscattered particles. In the case of imaging with ion beam, most of the SE signal comes from incident ions hitting the surface, offering richer surface information, superior

resolution, and a higher signal-to-noise ratio in comparison with SE signal in Scanning Electron Microscopy (SEM)[34]. In addition, the shorter escape length of iSE increases the likelihood of their escape from the surface and consequently leading to a higher yield of SE. The stopping power, which determines the rate of energy loss of the incident particles, differs for electrons and ions. The SE and iSE signals carry different information, and their yields vary with beam energy. Ions produce a larger iSE signal because of higher stopping power, shorter penetration range, and higher likelihood of escaping near the surface. Typically, the yield of iSE exceeds that of SE at higher velocities. Among various incident energies, helium ions exhibit the highest efficiency in generating iSE when the incident energy is approximately 50 keV. Whereas for electron beam the incident energy is around 1 keV for SE efficient production. In addition, the dimensions and configuration of the interaction volume are crucial for the behaviour of ions and the production of SE. A small, localized interaction volume leads to high spatial resolution imaging, while a large and broad volume degrades the resolution of SE images, as well as the contrast. The dimensions and configuration of the interaction volume depend on factors such as the type of ion, its energy, and the target material.

Figure 1.1 presents a comparison of five distinct ions, hydrogen, helium, neon, argon and gallium bombarding a molybdenum sample with a 40 keV incident beam energy[34]. The lightest ion, H^+ , has an interaction volume extending about 500 nm and mostly forward-looking from the surface. In the case of Ga^+ , as the heaviest among mentioned ions, the deepest extent of penetration is 80 nm and Ga^+ irradiation exhibits significant backscattering. In comparison, as the beam energy (E) rises, the size of the interaction volume for electrons expands as $E^{1.6}$, while for ions, it increases proportionally to $E^{0.6}$, resulting in a smaller interaction volume for ions[34].

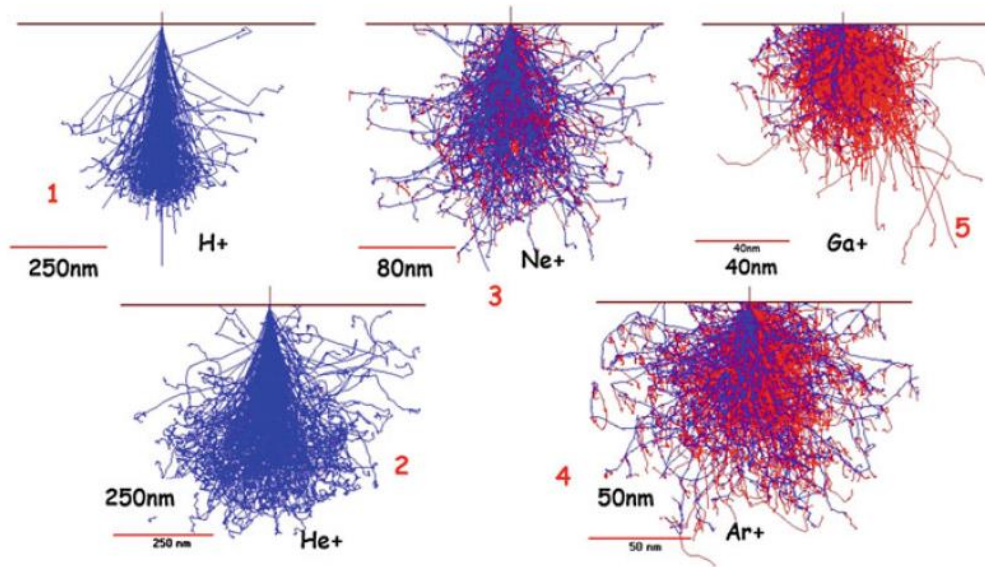


Figure 1.1: Comparison of interaction volume of H^+ , He^+ , Ne^+ , Ar^+ , and Ga^+ in molybdenum at 40 keV[34].

As mentioned in the previous paragraph, the absence of backscattered electrons contribution in iSE spectra is another important point which leads to higher resolution and enhanced surface detail in iSE images compared to electron-generated SE images. Also, we should consider the depth of field limitation in SEM due to the need for a highly convergent electron beam to minimize aberrations. As a result, this limitation confines the depth of field to a minor portion of the horizontal field of view. However, with ion beams applications, the convergence angle can be significantly smaller without suffering from diffraction effects because of the smaller ion wavelengths. When the aperture size is decreased, it improves the depth of field; however, an excessively small convergence angle decreases the beam current. As a consequence, finding a compromise becomes a requirement. Under practical operating conditions, ion-generated images can achieve a depth of field that approaches the scale of the horizontal field of view, leading to a significant improvement in information content[34].

Additionally, electronic dissimilarities on the surface are more detectable through iSE emission as opposed to the electron induced SE. This difference is significant in dopant profiling, offering enhanced sensitivity and spatial resolution[35] which manifests as a contrast in dopant profiling within the SE image. The profiling of SE intensity depends on the local emission yield of secondary electrons, which correlates with changes in the work function due to doping[36], [37]. Hence, altering the electronic structure near the surface

through doping would modify the SE contrast. The imaging contrast between regions with varying doping levels is weakened by the presence of surface states on a terminated crystal. In cases of p-type doping, the bands bend downward at the surface, while in n-type doping, they bend upward.

Both experimental and theoretical evidence confirm that in images, p-type regions appear bright, whereas n-type areas appear darker. This contrast is attributed to the elevated and reduced SE yield of p and n regions, respectively[38], [39]. Furthermore, for weak doping, the SE contrast can be entirely eliminated through fixation at a singular Fermi level, whereas it may remain observable when the level of doping reaches a saturation point for the surface states[36]. Consequently, SE contrast for dopant profiling has emerged as a swift and efficient 2D nanoscale imaging technique, holding significant potential as a favourable alternative among of methodologies employed in the industry.

In previous studies[36], [40], [41], dopant contrast evaluation involved employing SEM and HIM on layered samples with known dopant concentrations. However, ion-implanted samples, characterized by varying concentrations demand an investigation into vacancy/dopant clustering due to implantation. The SE intensity dopant profiling in such samples holds promise and deserves further exploration[42]. Investigations on dopant profiling compared SE contrast in SEM and HIM to explore post-ion implantation damage within semiconductor materials showed the implantation damage triggers amorphization and the emergence of defects. The introduced dopant does not take up positions in electrically active substitutional sites; instead, it attaches to vacancies and defects, rendering it electrically inactive. Following the implantation, a subsequent firing procedure becomes essential for integrating the dopants into the operational substitutional sites[42].

1.1.2.2 Ion and electron induced channelling contrast in SE imaging

Channelling contrast refers to the fluctuations in signal intensity detected in crystalline samples. The alteration in signal intensity is a consequence of change in the incident ion beam direction with respect to the grain orientations in a polycrystalline specimen. This phenomenon is exhibited by both ion and electron projectiles. However, the concept of ion channelling differs significantly from electron channelling. The channelling effect for electrons is directly connected to the diffraction phenomenon. In contrast, the channelling

effect for ions is specifically linked to the particle range, which varies depending on crystal directions.

The contrast in ion channelling is directly affected by the incident ion range in crystalline materials. When dealing with low-index crystal-oriented grains, the ion range is greater, resulting in fewer SEs being emitted from the surface, leading to a lower SE signal. In contrast, for off-axis grains, ions come to a stop closer to the surface, causing the emission of numerous SEs and resulting in an increased signal. On the other hand, BSEs are the main contributors to electron channelling contrast. These BSEs either diffract or channel to create an electron channelling pattern. Electron channelling patterns are visual representations of the crystal lattice's symmetry as seen from the path of the incoming electron beam. These channelling patterns exhibit high contrast and visibility when the crystal's thickness is on the order of nanometres. However, as the specimen's thickness increases, the crystallographic contrasts decrease dramatically. Therefore, using the backscattered electron signal mode is the most effective way to observe electron channelling contrast. When the electron beam is perpendicular to the surface of a grain aligned with the on-axis, the emission of BSEs in the electron channelling pattern peaks producing a bright signal. Also, as the higher BSE signal enhance the SE signal, images obtained through ion channelling and electron channelling exhibit inverse contrast behaviour for on-axis oriented grains.

Figure 1.2 illustrates the SE images of a copper (Cu) sample generated using both Figure 1.2(a) ion and (b) electron beams within an FEI Helios 600 Dual Beam instrument. When employing electron channelling, bright grains are observed for low index aligned orientations pointed with arrow in Figure 1.2(b). Conversely, ion channelling tends to result in dark grains for low index aligned orientations pointed with arrow in Figure 1.2(a). Notably, the channelling width is greater for 30 keV Ga^+ ions compared to 5 keV electrons.

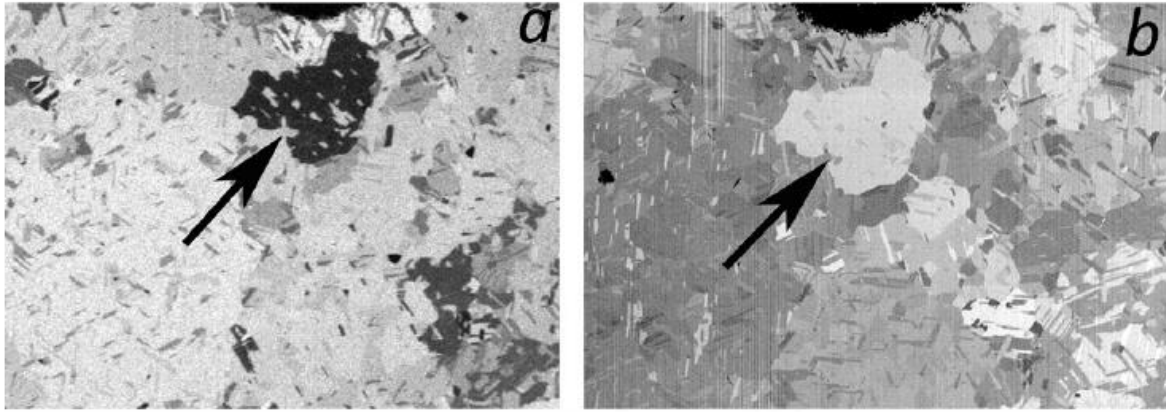


Figure 1.2: (a) iSE contrast (b) SE contrast resulted from ion and electron channelling respectively from a Cu sample. Both images have a horizontal field width of approximately 25 μm [43].

Channelling contrast serves as a valuable tool, unveiling alterations in the crystallographic orientation of a material, while also offering insights into defects within the crystal such as grain boundaries and dislocations[44]. Moreover, it presents hints regarding the surface quality. For instance, the contrast diminishes or vanishes when the surface is contaminated or mechanically damaged. The initial ion microscope[45] was established specifically to showcase channelling contrast for the purpose of determining mineral orientation and interfaces of minerals. Ion channelling offers an alternative means of exploring materials and the ion channelling contrast has been extensively studied[43].

1.1.2.3 The transmission imaging modes and contrast using He^+ ion focused beam

Transmission imaging signals rely on the interaction and scattering of particles passing through the sample. Bright field (BF) mode captures the non (or a very low angle) deflected beam for imaging, while dark field (DF) mode uses the strongly deflected portion to create the image. ADF (Annular dark-field) integrates the transmitted beam within a specific polar angle region across a whole annulus. On the other hand, by considering the deflected beam within a defined polar and azimuthal angular sector the image can be created. The transmitted beam tends to scatter surrounding the axis of incidence in a symmetric way in amorphous materials with perpendicular incidence angle. The material characteristics and sample thickness affect the average polar angle of scattering. Distinct combinations of materials and thicknesses result in unique scattering polar-angle distributions, which generate a contrast comparable to the mass-thickness contrast in TEM. In BF mode, areas of the sample with low or negligible scattering display high intensity in the image, while areas

that scatter beyond the detector's collection angle appear with low intensity. Conversely, in ADF mode, regions of the sample scatter within the specific angular range appear bright, while areas with minimal scattering appear dark. BF imaging offers an increased count rates for the similar beam current using the thin samples, whereas ADF imaging can be useful to improve the contrast for special compositional characteristics by adapting the collection angle to correspond to the scattering distribution for a specific materials and thickness[46]. Crystalline materials exhibit additional contrast mechanisms due to the dependence of the stopping power to the crystal orientation[47]. Certain crystal orientations align atoms in rows or planes, facilitating penetration of the projectile atom. These orientations, known as the channelling directions in channelling concepts, will be elaborated more deeply in the following section. Channelling directions exhibit decreased secondary electron[48] and backscattering, in comparison to random orientations. Conversely, ions experience enhanced range and the probability of the transmission when channelled along these directions. Also, the crystal orientation effects on the radiation damage after ion beam exposure, sputtering and ion collecting efficiency which has been studied before the channelling discovery. However, the scientists initially mixed these effects by diffraction, whereas it is not the same, and the channelling and diffraction are entirely different phenomena with very different energy scales. Also, the mentioned effects cannot be regarded as channelling effects since we cannot rely on steering ions in the few first atomic layers on the surface, which is thought of as the geometrical transparency of the lattice.

In addition to the aforementioned contrast mechanisms, using the transmitted particle's energy introduces a novel approach that improves the details obtained from transmission imaging modes. This energy measurement provides insights into the interaction between the projectile and the sample and improves the signal-to-noise ratio[49], [50]. In keV energy range, a significant fraction of the transmitted particles are neutrals[51], and so, magnetic or electrostatic spectrometers are unsuitable. Instead, energy-sensitive detectors or detection systems capable of implementing Time-of-Flight (ToF) measurements are required for ion energy-loss spectrometry and energy-resolved imaging.

1.1.2.3.1 Channelling Theory

The basic theory of ion channelling was developed in the 1960s by two physicists, Peter Sigmund[52], and Jens Linhard[53]. They developed the theory after the calculation done by

Robinson and Oen[54]. Robinson and Oen's calculated the slowing down of atoms in crystalline solids for individual paths in low energies. They did the calculations with binary collision simulations. In addition to the Robinson and Oen's theoretical work, Dearnaley [55] did the transmission experiments on Si crystal with 2.1 MeV H^+ . The results showed the spectrum in Figure 1.3(a), is symmetric and expectedly widened by straggling in energy loss when measured in a random direction (not parallel to any strongly channelling crystal axis or plane). On the other hand, Figure 1.3(b) showed a long tail toward higher energies in energy spectrum of transmitted H^+ when using a beam with the incidence angle parallel to a $\langle 110 \rangle$ axis. Thus, it is evident that the route parallel to $\langle 110 \rangle$ experiences a lower average energy loss. Linhard interpreted the long tail presence as the evidence which explains the long-range controlled motion at such a high velocity[56]. Also, variations in ion intensity recorded with respect to crystal alignment showed peaks, which is indicative of the channelled ions presence[57]. The peaks were seen for both transmitted and reflected ions. Also, Nelson and Thompson[58] demonstrated the peaks in the ion intensity plots using 75 keV H^+ ion beam. They observed high H^+ ion intensities transmitted through thick (300-400 nm) single-crystal gold films in the $[110]$ directions[57].

After bringing up the channelling concept by Linhard[53] and Sigmund[59], Lehmann and Leibfried[60], together with Nelson and Thompson[58] explained the motion of channelled ions by modelling the ion's interaction with the crystal using continuum potential. The continuum potential is acquired by calculating the average interaction potentials between ions and atoms along the channel axis or plane[61].

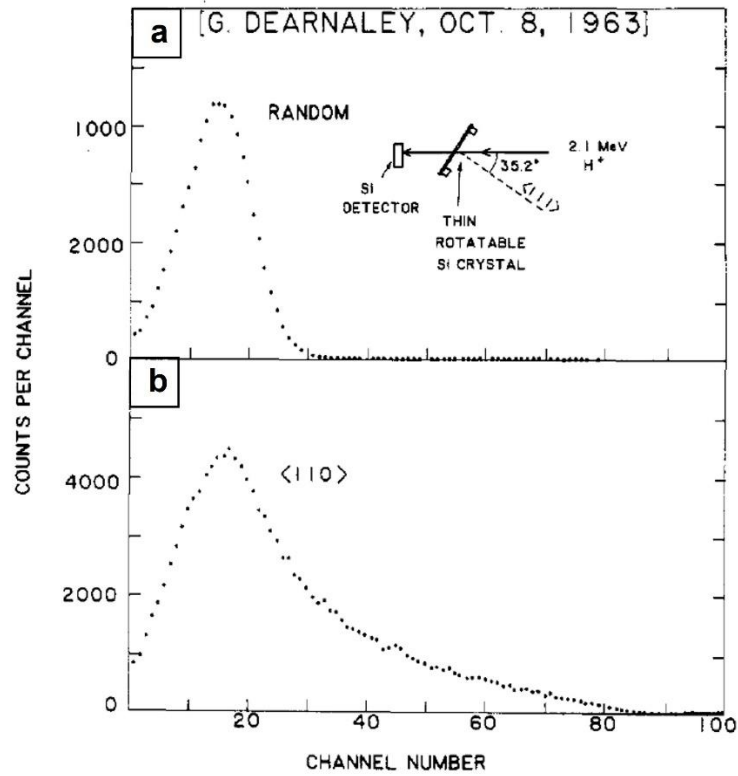


Figure 1.3: Transmission of 2.1 MeV H^+ through a 30 μm Si (111) crystal for random direction of beam (a) and (b) incidence angle parallel to a $\langle 110 \rangle$ axis [56].

Looking more closely at Sigmund and Linhard's writings, we can describe channelling as a smooth steered motion by a positive nuclear particle. The positive nuclear particle may have specific stability along the major axis of a crystal that encounters the periodic forces mainly focusing and occasionally defocusing (repulsive coulombic forces along the path). Furthermore, the sum of the forces causes oscillations, and any oscillation occurring within the channels is considered as channelling.

Lehmann and Leibfried[60] well described the theoretical treatment of channelling. Note that the positive nuclear particles must not go too close to the rows or planes of atoms to be channelled, otherwise they will be deflected strongly. The path is parallel to the aligned row of atoms or plane of nuclei (Figure 1.4), which avoids the positive charged particle from nucleus collisions and direct them into a specific crystal direction. This results in deeper penetration of positive nuclear particles in the target. Thus, the so-called channelling effect leads to an extreme reduction of all physical processes demanding close collisions, for example nuclear reactions, wide-angle scattering, and X-ray emission[56], [61].

For channelling conditions, a formula derived for critical angle frequently used in the literature is discussed below[62]–[65]. When a positively charged particle enters a crystal at the φ angle, which is depicted in Figure 1.4. it begins to channel. The transverse kinetic energy will be converted with a coefficient of φ^2 to transverse potential energy in r_{min} . Which will conclude in the formula:

$$\varphi^2 = \left(\frac{Z_1 Z_2 e^2}{Ed} \right) \log \left[\left(\frac{Ca}{r_{min}} \right)^2 + 1 \right]$$

C is a numerical constant. a is the Thomas-Fermi screening length. Z_1 is the nuclear charge of incident ion. $Z_2 e/d$ is the average nuclear charge density along the aligned target atom row and E is the energy of incident beam. As φ increases, r_{min} decreases until $r_{min} \leq \rho^2$ (the 2D vibrational amplitude). In this condition, atomic collisions could be possible, and the channelling stops as the smooth steer motion disappears. Thus, the critical angle for channelling is acquired by replacing $r_{min} = \rho^2$. By this formula, the incident angle can be tuned to increase the collision for special applications, for example, to increase the alpha particle emissions[66], to control the nuclear reactions[67], sputtering yield and Rutherford backscattering[68]. In contrast, the perpendicular direction for the incident beam also can be tuned to lower the collision occurrence possibility.

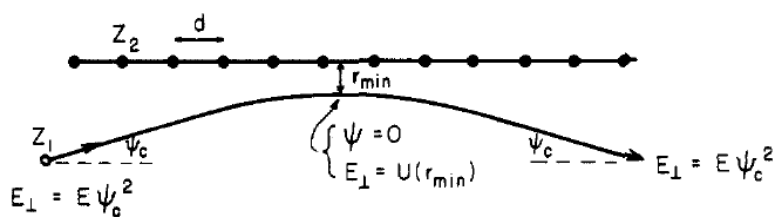


Figure 1.4: Steering process schematic[56]

According to Lindhard's study on the effect of a crystal lattice on the motion of charged particles, the transmission curve is likely to have several distinct features. A critical channelling angle is one such feature which is associated with the width at half-maximum of the observed peak. In this regard, the intensity transmitted in relation to the tilt angle for 1.8 keV D^+ ions on a 225 Angstrom gold single crystal is shown in Figure 1.5[57]. The

characteristic half-width is found to be $\sigma_\theta = 3.1^\circ \pm 0.2^\circ$ for the [001] peak in Figure 1.5, using 1.8 keV D^+ ions beam on a 22.5 nm thick gold foil single crystal. ANDREEN et al. measured the critical angle for channelling in the low-energy range for H^+ , D^+ , and He^+ ions transmitted through single-crystal gold foils.

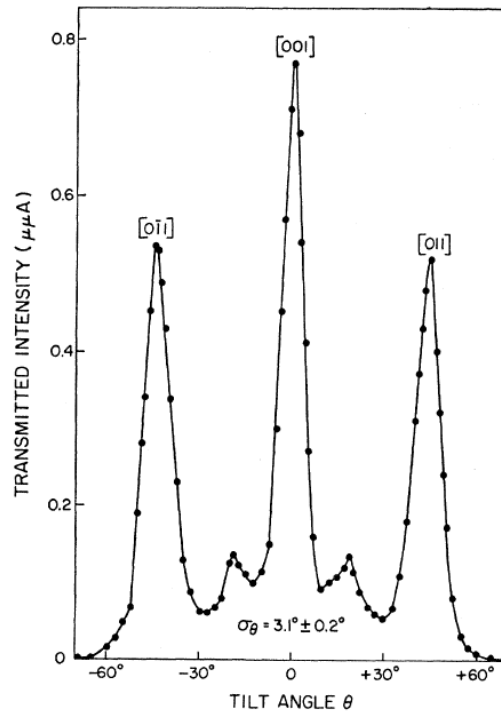


Figure 1.5: D^+ ions transmitted intensity in the [100] axis as a function of the tilt angle with incident ion energy of 1.8 keV on a 22.5 nm thick gold foil single crystal[57].

Few studies systematically examine where channelling occurs outside the principal crystal directions. A few experimental channelling maps that display the degree of channelling as a function of the incidence beam angle have been measured[69], [70]. Also, investigating ion penetration into materials at energy levels where the occurrence of many simultaneous collisions could be significant is well suited to Molecular Dynamics (MD) methods[71]–[74]. Particularly, it has been studied that MD in the Recoil interaction approximation (RIA), which exclusively considers interactions of energetic ions with the atoms in the lattice, is an effective yet accurate method for characterizing ion penetration even at reasonably low energies [71], [74], [75]. Results indicate that channelling theory effectively predicts the active channels at a given energy. The predictions are not only good at high energies but also down into the sub-keV regime, provided the ion covers a substantial distance. However, we must keep in mind that the quantitative comparison between the theory and MD for the

channelled ions as well as the channelling directions are reasonable but not perfect. Since the channelling theory is based on multiple assumptions the theory does not fully match the experiments. For instance, it has been assumed, that the ions can be divided into channelled and non-channelled types. This disregards varying de-channelling probabilities and different mean energy deposition and ion ranges in various channels. Moreover, it ignores the possibility that non-channelled ions may interact with the crystal more strongly than they would with a random target (the "channelling shoulder" effect), to varying degrees depending on the ion species, target, and energy. In addition, the scattering of previously non-channelled ions into channels results in broadening the channelling areas in the channelling maps. This is most noticeable at low energies and is also not considered by channelling theory. The MD simulations are thus supported by channelling theory. However, it does not give all the quantitative information.

Hall et al.[76] used ion transmission through a SiN membrane to measure the thickness of the membrane down to roughly 5 nm. Also, they demonstrated via Transport of Ions in Matter (TRIM) modelling that the proportion of transmitted ions rises linearly with decreasing SiN membrane thickness. This finding is consistent with the idea that primary ions passing through thicker membrane areas will scatter more intensely, which would be stopped by the beam-limiting aperture. The setup in HIM incorporates a beam limiting aperture positioned below the sample[76]. As a result, the highly scattered ions would not contribute to the image formation. This approach of in situ thickness assessment should be applicable to a diverse range of materials in addition to SiN because the brightness alteration is produced by the ion beam's scattering[77] and solid-state nanopores[76], [78].

1.1.2.3.2 Channelling applications

The channelling effect finds application in specific ion beam analysis techniques, and it has been elucidated through analytical theories and computer simulations at the atomistic level. Generally, the channelling phenomenon is a simple effect and once discovered, there were discussions and advancements in solid-state applications. Practically every use of channelling is dependent on a characteristic of the steered motion: specifically, the channelled beam's exceptional ability to discern atoms that shifted only more than r_{\min} distant from the aligned row (or plane). Recall that r_{\min} is the predictable function. There is currently a lot of interest in channelling for materials with more complex structures than those that have previously

been simulated, such as high temperature superconductors. Furthermore, simulations in $\text{YBa}_2\text{Cu}_3\text{O}_7$ have been reported[79]. The impact of imperfections of a crystal on the quantity of channelling and consequently on the number of close collisions, are a well-known example of channelling applications[61]. Furthermore, there are interesting topics[56] such as: hyper channelling, detecting incoherent precipitation, Kumakhov radiation, locations of lattice site, Mosaic spread, nuclear lifetime, phase changes and orientation of crystals detection, energy loss measurements, radiation damages, surface structure analysis, and x-ray detection from channelled ions, which are of interest as an application in channelling concept, and some will be discussed below.

The energy loss per unit path length, is one well-known feature of channelling and it will be extensively covered in chapter 5. Study on the implanted impurity distributions in the crystalline materials is a well-known example of energy loss study's application. As ion implantation is the main method for delivering dopant atoms into semiconductors, dopant distributions must be carefully regulated to fulfil the demands of device downsizing. This has important implications for the fabrication of semiconductor devices[61].

One of the motivations behind the study of channelling is the investigations on the effect of channelling of various grain orientations in bulk targets with respect to the incident beam direction in HIM. The interpretation of HIM or FIB images should consider the orientation of the crystalline targets[81]. Specifically, channelling has the potential to enhance the contrast of the resulting image[82], [83] and may be utilized to learn more about the target's crystal orientation[84]. By comparing channelling and non-channelling situations, information about the sample's crystalline structure can be obtained[85]. This goal requires a comprehensive study of the different orientations in crystals in HIM imaging[86].

Finding incidence directions that prevent channelling would be one practical use of the channelling theory as it accurately predicts active channels. Also, the isotope effect on channelling has been studied in the literature, although the channelling theory is independent of the masses of the atoms[87], [88].

Transmission-mode imaging allows us to interpret the information about ion channelling and can be helpful to several applications of channelling phenomena. Using the transmitted ion intensity using a 35keV beam energy to quantitatively illustrate the in situ total thickness variation of the SiN membrane is one of the applications of STIM imaging data in the

literature[89]. However, very few systematic studies of channelling in orientations, except major low-index ones, have been done. STIM, allows us to image subsurface features and reveal information about the crystallinity of the nature of the sample. Studying channelling contrast with STIM is worthwhile since the findings indicate that channelling may vary in nano systems, particularly metallic clusters. The variations occur due to surface reconstructions, various annealing rates for point defects, and beam heating of small clusters with minimal heat transmission to the surrounding environment[86].

1.1.2.4 Time of Flight (ToF) measurements using He⁺ ion beam

The significance of ToF and energy loss measurements[90] has been demonstrated in previous research across various fields[91], [92]. For instance, within Ion Beam Analysis (IBA) techniques[93], [94], the measurement of stopping power offers a means to examine the structural and compositional characteristics of thin films or surface layers in bulk samples. Stopping power within IBA finds utility in both computational and experimental investigations of radiation damage and effects in materials under extreme conditions[95], as well as applications in electronic device manufacturing[96], nuclear physics[97], astrophysics[98], and medical physics[99].

As ions traverse through matter, they experience energy loss due to interactions with the electrons and nuclei of the target material. A formula exists to quantify the mean energy loss per unit path length, considering energy transfer governed by binary collisions with nuclei or electrons.

The following formula has been used to calculate the total stopping power (S), and the parameters are described below[100]:

$$S = S_n + S_e := \frac{dE}{dx}$$

$$S = S_n + S_e = n \int T(b)d\sigma(T)$$

- "n" represents the atomic density of the target material.
- "S_e" and "S_n" refer to electronic and nuclear stopping power respectively.
- "b" signifies the impact parameter.
- "T(b)" denotes the impact parameter-dependent energy transfer in a single collision.
- "dσ" stands for the corresponding differential scattering cross-section.

- For convenience, the stopping cross-section (ϵ) is used which is normalized to the target's atomic density in the target n :

$$\epsilon = 1/n \, dE/dx.$$

Once the sample thickness is known, the electronic energy loss can be employed to deduce the sample's composition using two complementary experimental approaches: (i) by analysing transmitted projectiles or (ii) by analysing backscattered projectiles, with typical scattering angles of θ_t less than 1° and θ_b greater than 150° , respectively. It's observed that transmitted ions generally experience minor deflections corresponding to large-impact-parameter collisions, while backscattered ions undergo at least one significant-angle scattering event, indicating a small impact parameter. The substantial difference in these probed impact parameters along the projectile's trajectory can result in energy loss discrepancies[101]–[103].

At sufficiently high primary energies, the influence of multiple scattering contributions becomes negligible. As a result, we can make a straightforward assumption: the projectile moves nearly linearly through the target, with minimal deflection. Similarly, in the case of backscattered projectiles, we can claim that their incoming and exiting paths also follow straight lines, albeit with an additional significant-angle back-scattering occurrence. For both transmission and backscattered geometries, the projectile transmits through the electronic system for a significant portion of its trajectory at comparatively considerable distances from atomic nuclei.

At lower-level energies, multiple scattering effects must be taken into account, resulting in an extended path length. Previous research works present diverse sets of electronic stopping cross-section data for numerous target systems[104]. This variability could arise from differing experimental methods, resulting in different contributions to energy loss depending on the impact parameter. However, uncertainties originating from dissimilarities in crystallinity, composition, or thickness inhomogeneity of the samples could also explain the variations. Furthermore, the crystal orientation in polycrystalline targets can impact the electronic energy loss in both transmission and backscattering geometry. For instance, distinct energy loss components from transmission geometry attributed to channelling and random orientations using Ne beam with primary energy of 300 keV through polycrystalline Cu foil[105]. In contrast, studies of proton and He^+ ion energy loss in polycrystalline Au for primary energies ≤ 20 keV did not exhibit such differentiation in energy loss

components[106], despite a slight distinction between channelled and random orientation energy loss[107].

Bruckner et al.[100] showcased energy spectra of transmitted and backscattered protons and He⁺ ions from Au and W samples. Two distinct contributions to the energy spectrum were observed for He⁺ ions passing through the gold foils., whereas this wasn't the case for protons. By manipulating scattering geometry and investigating different samples, the lower energy loss contribution was attributed to Au foil texture effects. The influence of sample microstructure was also evident in an analysis of energy loss in single crystalline Si in both random and channelling geometry using protons and He⁺ ions within a similar energy range[50]. Similarly, to Bruckner's study, the distinctions between transmitted and backscattered geometries were higher for He⁺ ions than for protons, ascribed to charge state-dependent stopping.

Figure 1.6 illustrates the energy spectra obtained through ToF data in Medium Energy Ion Scattering Spectroscopy (MEIS), presenting the conversion of ToF to energy loss for transmission and backscattered geometries. The experimental setup employed 50 keV proton projectiles on a gold foil with a thickness of 509 Å. In the case of transmission data, measurements were taken at $\theta = 0^\circ \pm 0.5^\circ$, while for backscattering geometry, the angle was $\theta = 160^\circ \pm 2^\circ$.

The peak position of the energy distribution (E_f) for transmitted projectiles can be utilized to determine the total energy loss (ΔE) in the film, where $\Delta E = (E_0 - E_f)$. This, in turn, allows for calculating the electronic stopping power. The origin of the peak could be attributed to either the most likely or the average energy loss. Here, E_0 signifies the initial energy of the projectile. For backscattering geometry, the total energy loss within the film can be inferred by calculating the width of the gold (Au) peak, denoted as $\Delta E'$. This involves the utilization of the formula $\Delta E' = k \cdot \Delta E_{in} + \Delta E_{out}$, where k represents the kinematic factor. Notably, both the energy loss on the incoming trajectory (ΔE_{in}) and the exiting trajectory (ΔE_{out}) contribute to this calculation.

Additionally, within the energy range from 20-350 keV, multiple scattering complicates a direct assessment of the electronic Stopping Cross Section. In Figure 1.6 the experimental and Monte Carlo simulation data are compared for both transmission and backscattering energy spectra. The simulation code, specifically TRIM for backscattering, enables the differentiation between electronic and nuclear stopping mechanisms. The optimal fit for

both the position and width of the Au peak is represented by the solid red line in Figure 1.6. The slight variation, indicating an increased specific energy loss in transmission geometry, can be elucidated to some extent to the presence of surface contaminants like adsorbed H₂O or similar compounds, which remain stable under the current low-intensity beam conditions. In contrast, the higher energy loss observed in backscattering geometry is attributed to the assumption of more significant energy loss during close interactions between ions and target nuclei.

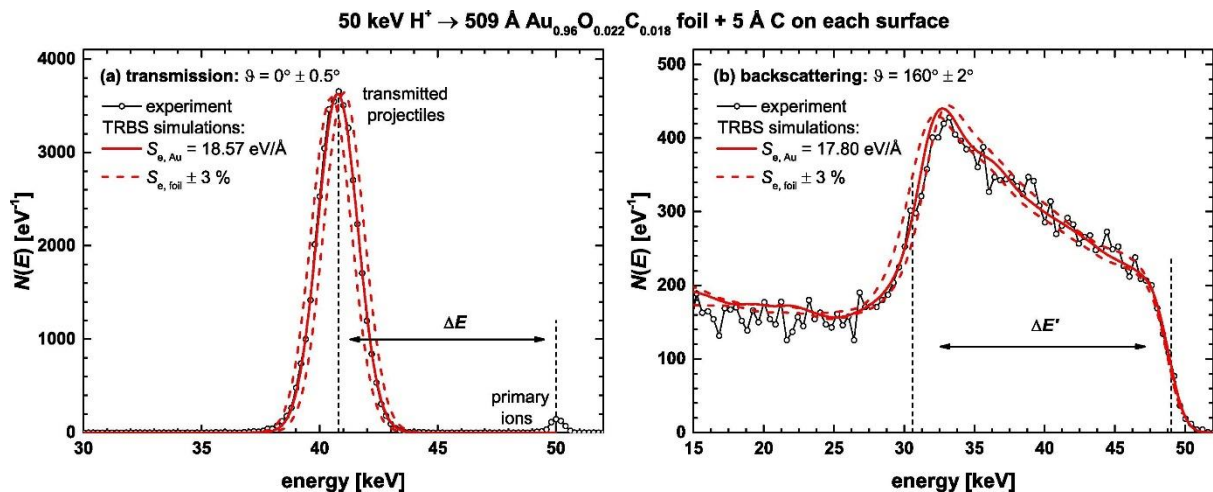


Figure 1.6: (a) Transmission (b) Backscattered energy spectra for 50 keV H⁺. The solid red lines in the graph depict simulations that offer the closest match to the corresponding spectra. Conversely, the dashed lines represent a range of electronic energy loss variation, namely $\pm 3\%$, serving to illustrate the attainable level of fitting accuracy[100].

An additional insight obtainable from ToF spectra involves quantitatively determining concentrations for recoil species. This determination entails predicting the location of specific recoil species while factoring in two key elements beyond scattering kinematics. These elements contain the energy dissipation of both the projectile and recoiling species within the target, along with the recoil cross-section. Hence, the energy and, subsequently, the observed ToF of recoils arising from varying depths are influenced by the specific projectile and recoiling species, as well as their stopping powers within the provided material.

Furthermore, in the context of crystalline materials, researchers have indicated that the stopping power exhibits dependence on the trajectory[50], [108]. For instance, in the case of a silicon sample, when the crystal axis [100] is parallel to the incoming beam, a considerable number of projectiles will undergo channelling. This results in ions undergoing minimal scattering angles around the incident beam's position, leading to reduced energy loss as compared to crystals oriented randomly. Upon rotating the sample by angles $\theta_x = 6^\circ$

around the x-axis and $\theta_y = 12^\circ$ around the y-axis, the incident beam no longer aligns with any low-index crystal axis. This geometric arrangement is termed (pseudo)-random. When ions experience scattering at wider angles, the crystalline structure's impact on their outward trajectory becomes more pronounced, resulting in effects like blocking and planar channelling. In exploring channelling and blocking patterns, Abel et al.'s [109] research revealed that ions channelled near the centre of the channel exhibit periodicity relative to the crystal thickness. Additionally, their work demonstrated that the distribution of channelled ions was unique at varying distances from the channel centre. The distances from the channel centre altered alongside changes in crystal thickness. This investigation involved the use of 1.9 MeV helium ions on a thin iron crystal oriented along the {110} planar channels. Similarly, Krause et al. [110] presented findings regarding the angular distributions of transmitted ions. They established that these distributions could be categorized based on the reduced crystal thickness, and certain peaks in the angular distributions could be ascribed to crystal rainbows. Crystal rainbow theory was developed to describe mentioned crystal rainbows within the context of ion channelling. This theory predicts the specific patterns of angular distributions related to the crystal's thickness [110], [111].

Another way to investigate the transmission helium ion signal for energy loss measurements is to use a stationary broad beam. Mousley et al. [112] investigated the stationary broad beam transmission mode imaging with energies of 20 keV. Also, some research has been conducted on STIM ion energy loss spectroscopy (STIM-IELS) using MeV helium ions in 1980 [113]. More recently, Au nanoparticles within entire cells have been observed with a 25 nm resolution utilizing MeV STIM-IELS [114]. The use of MeV He ion beam in radiography and radiotherapy is one of its intriguing applications [115]. When comparing MeV and KeV ion beams, the KeV ion beam is more common since MeV ion beams require a significant infrastructure while keV does not. Despite the widespread use of KeV He ion beams, there is a lack of research on evaluating the transmission imaging capabilities of such beams while simultaneously obtaining the energy loss of the transmitted ions. In 2021, Holeňák et al. [49] demonstrated that neutrals make up roughly 66% of the transmitted signal for 100 keV He⁺ passing through 25 nm C. Similarly, Allegrini et al. [116] used multiple layers of graphene foils and found a neutral fraction close to 100% for 20 keV hydrogen transmission. To

measure the energies of both transmitted ions and neutrals, a TOF measurement was employed with a linear flight path to account for possible neutralization within the sample. Since standard electrostatic lenses and deflectors cannot control the trajectories of neutrals, a straight post-specimen flight path is advantageous as it eliminates the need for the transmitted helium to be electrically charged.

1.2 State of the art 2: Technical challenges background on correlative microscopy approaches

Correlative microscopy is a powerful approach that involves the integration of multiple imaging techniques to obtain a comprehensive and multifaceted understanding of a sample's structure, composition, and behaviour. The multidisciplinary approach is particularly valuable in scientific research and various applications due to its ability to provide complementary information that individual techniques might not capture on their own[117]. Correlative microscopy is an excellent approach for examining complex materials such as solar cells [118], [119] and semiconductors[120].

A correlation approach involves SE and SIMS techniques to analyse the concentration of active dopants, a crucial factor for understanding the attributes and effectiveness of complex samples. Within the semiconductor industry, SIMS stands as a widely employed method for high-sensitivity dopant profiling. Advancements in correlative characterization methodologies have led to enhanced resolution in SIMS imaging[121], [122]. Ongoing works aim to improve correlative techniques for dopant profiling, emphasizing both improved sensitivity and spatial resolution. Additionally, efforts stay in accurately quantifying SIMS intensities[123], [124]. Nevertheless, the SIMS procedure requires calibration using reference samples to establish dopant concentration. Even with calibration, SIMS provides data only on total dopant concentration, unable to differentiate between active and inactive dopants within the material. The electronic contribution of dopants in the host semiconductor is what distinguishes active dopants from inactive dopants. An effective approach to distinguish the active and inactive dopants lies in correlating SIMS data with SE intensity profiles, a concept explored in greater detail in chapter 6, Case Study One.

Correlative microscopy approach is a well-known approach to characterize defects, interfaces in solar cell materials, and it is used to perform in situ studies to optimize solar cell designs and improve energy conversion efficiency[126]. SIMS with diverse high-

resolution microscopy methods enable the acquisition of chemical data with exceptional sensitivity through SIMS. SIMS combined with high-resolution images from other microscopy techniques such as, TEM, SE, and STIM in HIM and SPM could be an excellent correlative approach. For instance, an investigation on sodium doped CuInSe_2 thin films[125], mainly focusing on their grain boundaries, used correlative approaches with SIMS. This study used cathodoluminescence imaging, SIMS, and Kelvin probe force microscopy. By using SIMS and a correlation approach, they discovered that sodium (Na) doping positively impacts CuInSe_2 (CIS) photovoltaic material. Specifically, Na doping prevents the detrimental decomposition of CIS when exposed to air and heals oxidized grain boundaries[125]. Another case is, multi-junction solar cell materials, which is a complex system, comprise features at multiple length scales, from nanometres to micrometres. One of the notably efficient multi-junctions photovoltaic (PV) systems is represented by metal halide perovskites, which presents numerous benefits. The benefits include a high absorption coefficient with sharp absorption edges[126], ambipolar charge transport accompanied by substantial diffusion lengths[127], [128], and the capability to adjust the bandgap energy[129]. Incorporating the perovskite material into solar cells configuration involves the application of a thin perovskite film onto the frontal surface of a crystalline silicon (c-Si) cell. This strategic introduction of the perovskite thin film decreases thermalization losses and achieves an exceptional power conversion efficiency (PCE) that surpasses the 30%. The correlative SIMS image approach on metal halide perovskites will be discussed in chapter 6, Case study two and three.

A highly effective correlation method has been successfully done using the npSCOPE[130], which stands as the central focus of this thesis project and will be discussed in the following section(1.2.1). This correlation strategy involves integrating SE, SIMS, and STIM imaging. The complementary approach enhances the information acquired through SE imaging. In a previous study on biological samples comprising nanoparticles, the STIM mode of the npSCOPE proved beneficial by providing improved contrast compared to SE imaging[130]. This enhanced contrast facilitated improved positioning and navigation of regions of interest within the flat section samples. The contrast observed in STIM images resembled to findings in TEM images of comparable samples. Additionally, the combination of STIM and SIMS data enabled the precise identification of nanosized objects and the determination of their

chemical composition. Based on these capabilities, the correlative approaches in the npSCOPE instrument showed the potential for applications in the field of nanotoxicology[130].

1.2.1 npSCOPE

In this section, I introduce npSCOPE[131], an innovative in-situ correlative instrument, along with the different parts of the machine conducted on this novel instrument. By integrating different functionalities into a single instrument, npSCOPE offers enhanced flexibility and significantly reduces the analysis time for complex samples requiring complementary investigations from nanoscale grain boundary analysis in solar cell materials[132] to the study of biological systems interacting with nanomaterials.

The npSCOPE is based on the HIM Zeiss column, employing a Gas Field Ion Source (GFIS) as a crucial component and combining it with specifically designed SIMS and STIM technologies. HIM is being established as an alternative to SEM, offering high-resolution images with diverse applications. Ions, being heavier than electrons (He^+ ion is 7300 \times more massive than an electron), have smaller wavelengths. Small wavelengths enable imaging of sub-nm sized objects by achieving a very small probe size. For example, the probe size for He^+ is < 0.5 nm, and Ne^+ is < 2 nm using the GFIS. While positive ions are commonly used in ion beam microscopy techniques[34], negative ions[133] and special cases like buckyballs[134] can also be used. Specific criteria constrain the selection of available ions in GFIS systems. Ions suitable for GFIS applications must have high ionization potential and low reactivity. Hydrogen and helium, among various other elements meeting these criteria, are commonly employed. Additionally, neon and nitrogen are also acknowledged as suitable ions for GFIS due to their ability to achieve higher milling rates, rendering them especially valuable for milling applications. Figure 1.7(a) shows the schematic of a GFIS in HIM. The electrode, which is a wire made of a single crystal tungsten, functions as an emitter tip cooled down to 60-90 Kelvin and is optimized using the Scanning Field Ion Microscope (SFIM) mode. Tip activation would produce a trimer (Figure 1.7(b)) if the high voltage given to the tip were steadily increased. Trimer is a three-atom pattern arranged in a triangle format at the front edge. Only one of the three helium ion beams selected from trimer using an aperture and final adjustments. The ion current generated by the source is approximately linear with

helium gas pressure and reaches a maximum value of 50-100 pA. Typically, the beam current remains highly stable, fluctuating by only a few percentage points over extended periods of several minutes. This configuration enables the attainment of optimal source brightness, measured at $4 \times 10^9 \text{ A cm}^{-2} \text{ sr}^{-1}$, and primary currents within the range of 0.1 to 100 pA[48], [121].

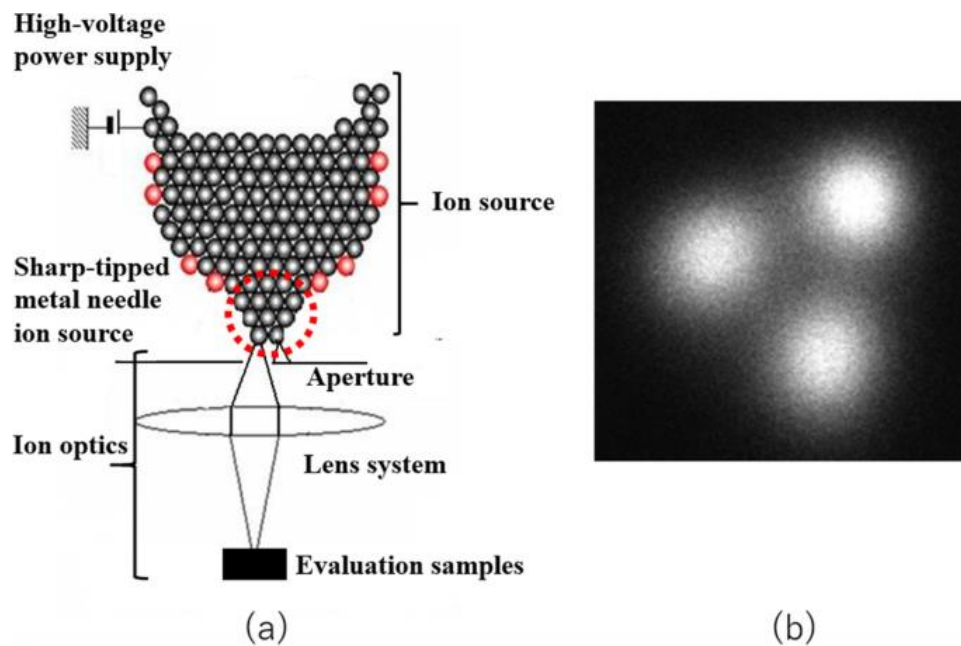


Figure 1.7: (a) Schematic of a GFIS and ion optics (b) image of trimer generated by Helium ions at the tip of the source[135].

The relationship between the voltage applied to the extractor and the emission current of the trimer follows a specific pattern. The Best Imaging Voltage (BIV) is determined as the voltage where the emission current reaches its highest value. The tip shape defines the relation of the electric field with the voltage. The field also acts as a barrier to prevent gas molecule and atoms from accessing the tip leads to hinder the contamination of the tip [34].

Figure 1.8 displays the pictures of the npSCOPE instrument. The GFIS column is positioned vertically above the analysis chamber, which is a stainless-steel vessel compatible with ultra-high vacuum (UHV). The chamber has a high precision 5-axis sample stage for precise positioning (X, Y, Z, rotation, tilt). The instrument features three key detectors:

1. An efficient Everhart-Thornley (ET) detector with a standard distance above the sample.
2. A unique mass-filtered detection system and a double-focusing magnetic sector SIMS with adjustable extraction and transfer optics.

3. A 2D position-sensitive detector which is developed for STIM imaging, mounted on a mobile support beneath the sample stage.

In addition, a low-energy electron flood gun is also included in the instrument to allow charge compensation while imaging non-conductive samples. As the SIMS and STIM detection systems are the key innovations in the npSCOPE instrument compared to a standard HIM, further elaboration on these systems will be provided in the subsequent subsections.

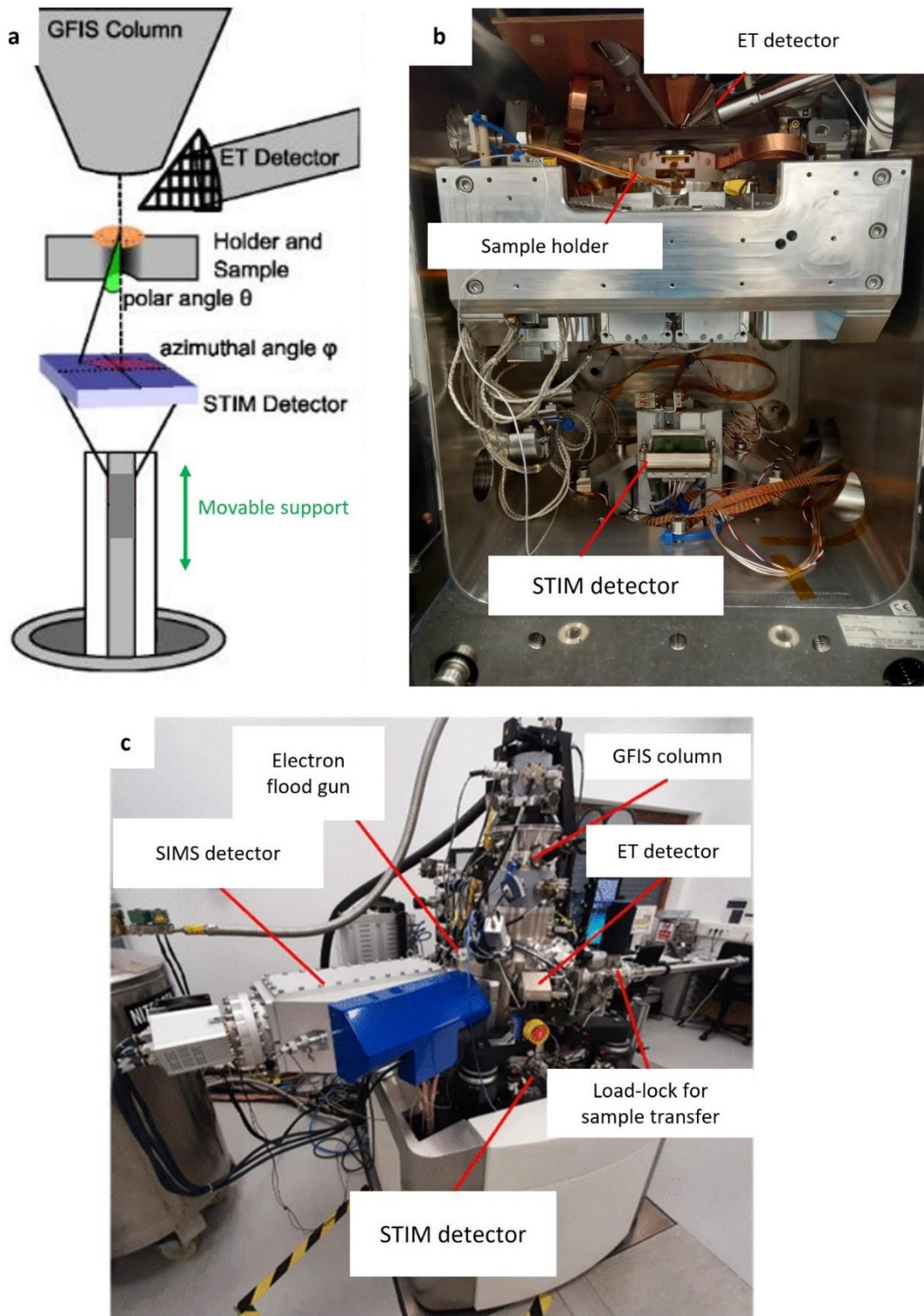


Figure 1.8: (a) Schematic representation (b) interior picture (c) exterior picture of npSCOPE instrument integrates GFIS technology with various detectors for high-resolution imaging and analytics[131].

1.2.1.1 SIMS (subsystem) in npSCOPE

Energy Dispersive X-ray Spectroscopy (EDS), a chemical microanalysis technique, which is often used with electron beams, is not practical for ion beams of keV energies due to very

low emission of characteristic X-rays. Rutherford Backscattered Ions (RBI) is an alternative approach for microanalysis based on ion-beam. However, Rutherford backscattering suffers from limitations, such as the decreasing spacing between element peaks as atomic number increases, which makes the heavy elements detection more challenging. Additionally, ions undergo elastic and inelastic collisions in the specimen, affecting the energy spectrum reaching the detector. The composition and the thickness of the specimen, as well as the beam energy influence the spectrum, with thicker samples and high-atomic number materials being less suitable for Rutherford backscattering spectrometry (RBS) analysis, especially at low beam energies. Another alternative instead of EDS is SIMS, which involves scanning a beam of primary ions across a material and it is a surface characterization method to acquire chemical information. SIMS utilizes an energetic beam of focused primary ion projectiles (such as Ga^+ , Ne^+ , Cs^+ , O^-) which is directed to the sample and that collide with a material in a high or ultra-high vacuum environment. Figure 1.9 Depicts an illustrative representation of the process where an ion beam impacts the surface of a target. Upon impinging, the momentum is transferred from the primary ion to the solid surface, which causes the sputtering of surface atoms and molecules and generating positive or negative secondary ions in addition to sputtered neutral atoms or molecules and secondary electrons. Finally, the technique distinguishes and classifies individual ions and ion clusters based on their mass-to-charge ratio[136]. In SIMS if the beam size is smaller than the dimension of collision cascade, the spatial extent of the collision cascade could determine the lateral resolution of acquired images. For a 20-30 keV Ne^+ beam, this extent is approximately 8 nanometres[137].

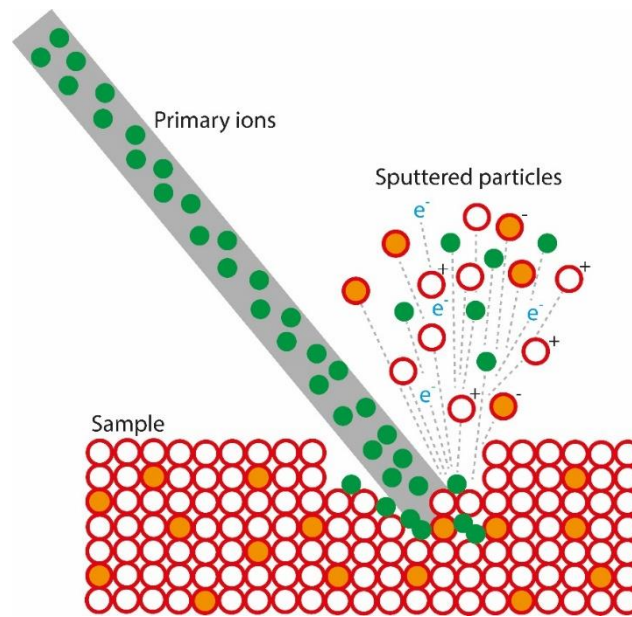


Figure 1.9: A schematic representation of the process involving high-energy primary ions bombarding the surface, leading to surface sputtering and the emission of neutrals, positive and negative ions, electrons, and the recoil of the incident projectiles[138].

The SIMS employed for npSCOPE represent an improved iteration of the previous SIMS system designed for HIM, which is documented in other references[139]. A simplified overview of the SIMS system in npSCOPE is shown in Figure 1.10. A compact double-focusing magnetic sector mass spectrometer with cutting edge SI and transfer optics are employed. The extraction optics is positioned between the GFIS column's end nozzle and the sample. It can be controlled by a piezo-driven positioning system. The optics are meticulously designed to extract secondary ions efficiently while operating at low potentials to deviate from the primary ion beam. The transfer optics facilitate a step for post-acceleration, increasing the energy of the secondary ion beam (to a few keV) as it moves toward the spectrometer's detection section. Consequently, a floating setup is required for the entire SIMS system. Furthermore, when the SIMS optics are withdrawn, SE imaging at a minimum working distance could be enabled. The npSCOPE's SIMS system is different from previous SIMS versions used in standard HIM systems. It includes a single continuous detector placed along the magnetic sector's focal plane. The detector uses Micro Channel Plate – Detection limit (MCP-DL) technology. The innovative FPD allows simultaneous full mass spectrum collection for every single pixel on the sample surface. It provides notable benefits compared to previous multi-collector detection systems. These benefits include:

1. Enabling various post-processing techniques through the acquisition of hyperspectral SIMS images containing the full mass spectrum for each individual pixel.
2. Maximizing sensitivity by detecting the entire signal for each peak.

Reducing analysis time considerably, with a full mass spectrum of the entire FOV generated in just 1 second using the FPD, as opposed to the previous SIMS generation with four individual detectors, which typically took 2-3 minutes.

A TIC detector is incorporated into the SIMS system after the transfer optics. The TIC detector enables detection of non-mass filtered SI signals in positive mode, as well as an integration of SI and SE counts in negative mode. The SIMS unit can be easily switched between TIC and FPD modes. The TIC detector is commonly utilized as a rapid imaging method, offering supplementary contrast data in addition to the SE-imaging mode. The SIMS system offers various modes of operation, including mass filtered image, mass spectra, depth profiles and eventually 3D chemical map acquisitions.

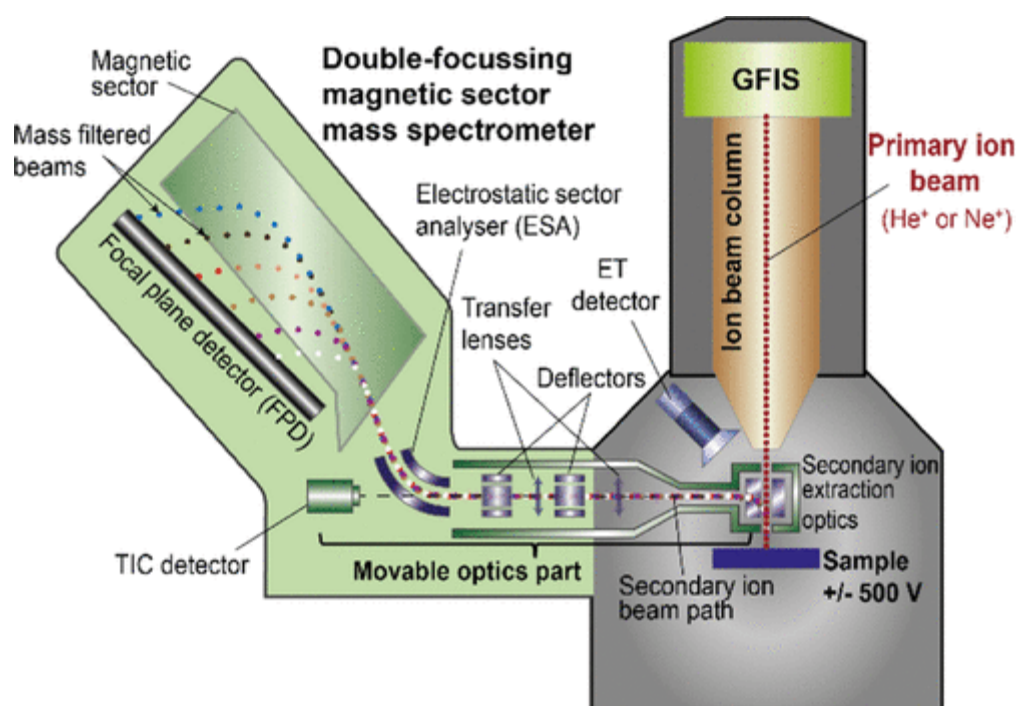


Figure 1.10: Cross section schematic of the compact double focusing magnetic sector SIMS system on the npSCOPE. However, the real setup of the SIMS is horizontal, it has been vertically flipped for illustration [131].

1.2.1.2 STIM in npSCOPE(subsystem)

Both SE and SIMS methods are surface imaging techniques, and they fail to provide detailed information about subsurface features in the material. Scanning Transmission Ion Microscopy (STIM), on the other hand, has the potential to enable sub-surface imaging using transmitted He^+ ions and neutral atoms[46]. The neutralization of He ions allows the study of charge exchange processes. STIM introduce novel contrast mechanisms not available in other microscopy methods. For example, the SEs exiting from the backside of the sample creates a new contrast. Additionally, transmitted ion signals can be utilized to produce bright-field and dark-field images by adjusting the collection angle through detector movement relative to the sample. Also, STIM can provide advantages in applications, such as semiconductor manufacturing[140]. In ion transmission mode, ions with high energy (e.g., 10 keV or more) penetrate materials to a significantly smaller extent compared to electrons of the same energy. However, if the specimen is made thin enough, despite interaction with the material, a considerable portion of the incident ion beam manages to traverse it, offering the opportunity to capture transmission ion image. The usable thickness values depend on the ion energy and material properties, with lower atomic number and density materials allowing for thicker specimens. Despite the lower usable thickness compared to electron beams, ion transmission mode still provides quality images.

1.2.1.2.1 STIM in comparison with TEM

Observing crystalline materials in transmission ion mode yields familiar images resembling TEM images of similar materials. For instance, Figure 1.11 shows the (a) bright field and (b) dark field TEM images of an MgO cube which indicate alternating bright and dark bands, known as thickness fringes [34], [141] which are consistent with TEM images. The dimensions and fringe spacing allow for the calculation of the extinction distance. Dislocation structures can also be observed, appearing as dark lines in the bright field image. Despite the similarities between STIM and TEM, employing ions offer a number of benefits. The exchange of charge between the projectile and the target provides us with valuable insights into the target. However, in TEM, the charge transfer processes do not offer substantial information because electrons are readily absorbed by the material, resulting in

limited data that can be utilized to gain information into the sample. Conversely, when ions are used, they can exchange charge and become neutralized. This allows us to collect neutral atoms, providing valuable data about the charge exchange process. This is achieved by analysing the position and fraction of neutralization events on the sample. Charge exchange plays a significant role in the investigation of biological samples, as it enables the generation of contrast through charge exchange mechanisms.

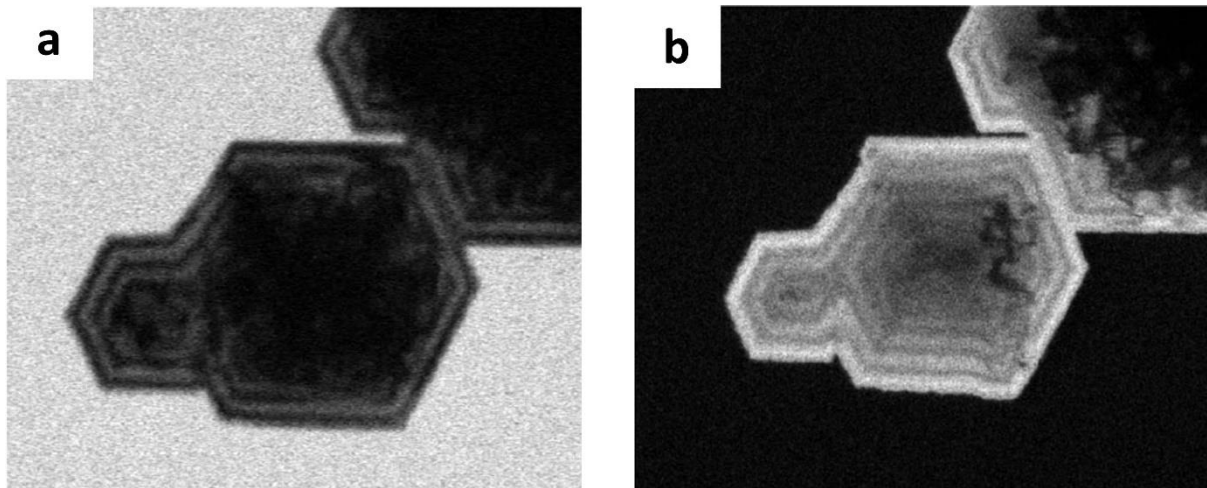


Figure 1.11: (a) Bright field and (b) dark field 40 keV He^+ ion transmission imaging from MgO crystalline sample. The field of view for both images are 200nm. The thickness fringes are presented in both images[142].

Another advantage of STIM is the ability to discern between interstitial or substitutional dopants which is possible due to the ion channelling contrast. Interstitial atoms obstruct the path of channelled ions, leading to their detection through channelling contrast within STIM imaging. In contrast, substitutional ions do not impact the channelling process. Whereas in TEM, such investigations are complicated.

Furthermore, the scattering cross sections of ions is larger by orders of magnitude when compared to electrons having the same energy. This larger cross section allows lower doses to accomplish a sufficient level of contrast which is particularly beneficial for beam-sensitive samples. Furthermore, TEM faces a limitation wherein samples are typically required to be conductive. Thin insulating films in close proximity to conductive materials can still be imaged by TEM. On the other hand, ion microscopy offers the advantage of using an electron flood gun to mitigate charging effects, enabling imaging of even bulk insulating samples. Lastly, STIM enables the comprehension of fundamental studies of ion-solid interactions. Such investigations are unfeasible with TEM[143].

1.2.1.2.2 STIM signal characterization

Various techniques mostly on SE-based methods are employed to detect the STIM signal, each having its own strengths and limitations[76], [142], [144]–[147]. Using SE-based methods eliminate the need for additional detectors, allowing for the utilization of higher beam currents compared to more sensitive detectors. On the other hand, in SE-based methods direct measurement of counts is impossible, and there is a lack of positional information on the detector. Moreover, additional measures need to be taken to minimize the contribution from SE electron signal originating from the top surface of the sample[121]. The HIM has demonstrated the ability to achieve mass-thickness and thickness-fringe contrast in transmission mode using a combination of Bright field and Dark field conversion detectors[143]. An annular microchannel plate detector was employed in a separate study to investigate gold-silica core-shell nanoparticles in ADF mode[148] which entail the utilization of a physical aperture. The aperture limits the favourable angle during BF imaging and modifying the length between the sample and the annular detector to control the favourable angle range during DF imaging. Recently, a position-sensitive detector comprising a silicon diode array to detect the transmission signal has been implemented in the HIM[149]. The position-sensitive detector employs a stationary beam of ions to quantify the intensities of particles arriving at the detector through scattering[150]. Additionally, when combined with a scanning beam, it has been effectively used for STIM imaging[151].

The implementation of a diode array in HIM enables the detection of both ions and neutrals, providing information about position of the arriving counts on the detector. However, individual arrival times cannot be recorded. Notably, STIM investigations in HIM have utilized detection of direct ion and neutrals, including the use of an annular Micro Channel Plate (MCP) for dark-field imaging[148]. More recently, a integration of an MCP and a Delay Line Detector (DLD) has been employed for STIM imaging to concurrently capture on-axis and off-axis data (each called BF and DF respectively)[46]. The schematic representation can be found in Figure 1.12. The MCP provides adjustable gain on the detector, thereby extending the scope of imaged intensities and the ability to detect neutrals. On the other hand, the DLD, despite its higher cost, offers the benefits of measuring information about the location and the arrival times for each count. This information enables finalization and selecting certain count groups from the five-dimensional dataset, consisting of 2D positional

information of sample and detector as well as the arrival time. In addition to STIM imaging employed in HIM, transmission ion microscopy has been explored utilizing stationary broad-beam of He^+ at energies lower than 50 keV[152]. This method involved a detector equipped with an MCP, a phosphor screen, and an attenuation grid. This configuration facilitated the utilization of higher beam currents while providing positional information. However, it did not capture arrival time information.

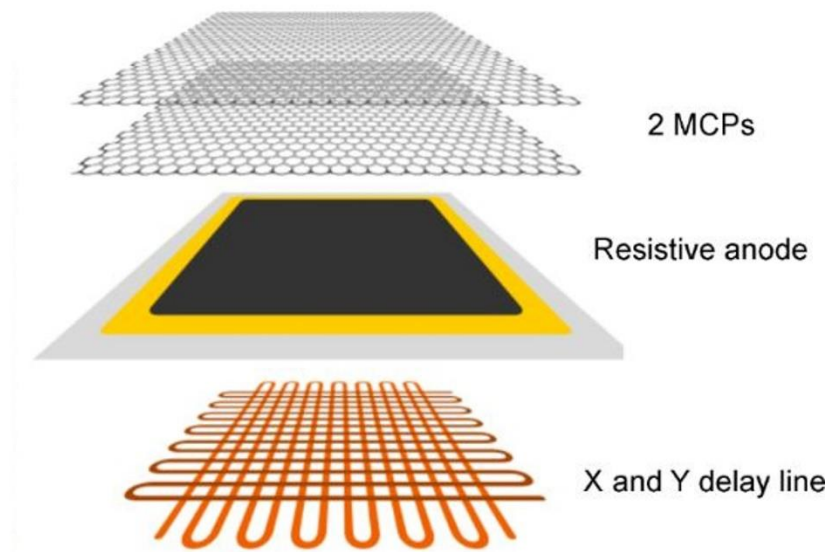


Figure 1.12: The schematic representation of a recently developed STIM detector.

The STIM detector in npSCOPE, employing MCP-DL technology, offers a comprehensive investigation of various contrast mechanisms due to its 2D delay line readout structure, providing position and time-sensitive detection capabilities. The STIM detector, positioned on a vacuum-compatible vertically adjustable rail, allows for distance adjustment between the sample and the detector. This adjustment enables the flexibility to record either high or low scattering angles with improved angular resolution. The He^+ ion or neutral particle that enters the MCP channel creates SEs. The subsequently amplified SEs then reach the delay line structure, generating output signals. The time of arrival of the electrical pulses at the termination point of each delay line determines the x and y coordinates of the collision position on the STIM detector for each event involving ions or neutrals. This information enables the creation of a 2D dataset that links the detected events to their respective x, y raster positions of the incident beam on the surface of the specimen, ultimately resulting in a 4D dataset. Using these 4D datasets, STIM images can be constructed by specifying a

range of scattering angles, giving rise to on-axis (BF) images, as well as off-axis images that may or may not exhibit DF characteristics depending on the sample's scattering radius. So, post-recording analysis allows for image formation relies on the transmitted signal at low angles (BF mode) or the high angles (DF mode) using minimum cut-off polar angle which is defined by the user. In Figure 1.13 we show an example of BF (image a in the left side in Figure 1.13) and DF (image b in the middle in Figure 1.13) from a polycrystalline gold membrane with 50 nm thickness. The DF, known as annular dark field mode, can provide strong contrast for specific mass-thickness combinations, such as a nanoparticle composed of a heavy element, precisely sized, embedded within a matrix of light material. By selecting specific angular ranges in both the polar and azimuthal directions, it is possible to acquire STIM images that correspond to particular scattering directions. The scattering radius is determined by the sample's chemical composition, which establishes both the scattering angle and the distance between the sample and the detector. Furthermore, post-processing the dataset allows investigation of transmission properties. This exploration focuses on individual characteristics within an image and involves studying intensity distribution in a specific subsection of the sample area. The goal is to understand the transmission behaviour of isolated features.

The STIM images showcased in this thesis captured in npSCOPE are derived from 4D datasets. When integrated with a pulsing system within the primary beam, the dataset can include ToF information, leading to the creation of 5D datasets.

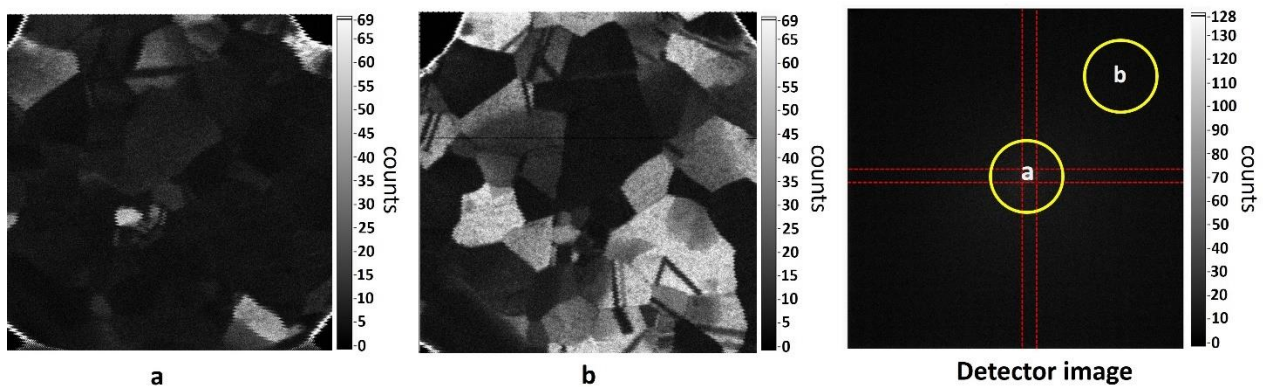


Figure 1.13: Image on the right shows the distribution of all signals received on the detector. The marked a, b yellow circles point out to the regions on the detector image for the respective STIM figure a and b from a poly-crystalline gold membrane. Image a shows BF with $\vartheta \leq 1^\circ$, with azimuthal angle centre $\phi = 45^\circ$ in (b).

Alternatively, the STIM setup can be configured by positioning the detector at a specific distance from the sample, to detect exclusively forward scattering within small angle. In this instance, BF imaging utilizes the whole detector region, enabling increased initial ion currents, quicker imaging, enhanced signal-to-noise ratio, and enhanced angular resolution. For more details regarding the STIM sub-system, refer to the research conducted by Serralta et al.[46]. In the STIM images showcased in this thesis, sample-detector distance was set at 256 mm. This configuration corresponds to a scattering angle ranging from 0 to 97 mrad for all azimuthal angles, with the corners of the detectors extending up to 137 mrad.

We should note that, in the majority of materials, where we use the commonly used 30 keV He^+ beam the straggling range extends from tens to a few hundreds of nanometres as indicated by Stopping and Range of Ions in Matter (SRIM) simulations[153]. Consequently, in samples with a thickness of less than 100 nm, a significant portion of the initial beam transmits the target and can be utilized to create the image. During this process, the interaction among the helium ions with the target atoms' electrons and nuclei occur. The interaction undergo collision which could be inelastic and elastic, which are influenced by various factors, including the material's properties, density, local thickness, and atomic arrangement. As a result, the part of the beam transmitted can offer the mass-thickness contrast[154], and provide some insights into the sample's crystalline structure[146]. Moreover, the transmitted signal allows for the localization of buried structures within the sample, which would otherwise remain undetectable using SE and SIMS which are signals affected by the surface features.

1.2.2 Galileo

Galileo as a STIM prototype was developed at LIST by Michael Mousley et al.[157], and its schematic layout is shown in Figure 1.14(a). For a labelled photograph, please refer to the annex section (Figure 8.1). In this configuration, He^+ ions are generated using a Cemecon duoplasmatron source operating at 1 kV arc voltage and 20 kV acceleration voltage. In our experimental arrangement, the ion beam exhibited a spot size of approximately 5 μm on the sample, which was adequate for our proof-of-concept investigation. However, by using a higher brightness ion source such as GFIS, we could potentially achieve a spot size on the sub-nanometre scale.

Within Galileo prototype, the 20 keV ions can be deflected by two sets of deflectors (D1 and D2) before being focused by the first einzel lens (L1). Subsequently, the ions pass through a Wien filter[158], followed by a 90° sector deflector[159] that bends the ion beam by 90°, effectively removing the neutrals from the beam. The beam is then focused on an aperture (5 mm diameter, A0200P from plano-em.de).

The dispersion within the beam caused by the Wien filter removes the undesired, permitting only the passage of He⁺ ions. After the aperture, a final set of deflectors (D3) performs raster scanning, while a second einzel lens (L2) focuses the beam onto the target. The base pressure within the sample chamber is 2×10^{-8} mbar, which increases to 1×10^{-7} mbar while applying the beam to the sample via gas injection in the source. The gas within the chamber consists of a mixture of residual air and helium. Please note when measuring pure helium pressure, the readings from the gauges need to be multiplied by a factor of 5. Therefore, the actual pressures will range from 1 to 5 times the measured values. The transmitted ions or neutrals, travel a linear flight path of 0.53 m from the sample to the detector. We employ a circular DLD from Surface Concept GmbH, Germany, which features an active area diameter of 40 mm. According to the detector specifications, the estimated pixel size is 26.55 mm × 25.42 mm, resulting in an area of 6.75×10^{-10} m². With a separation distance of 0.53 m, each pixel covers a total angular width of 5×10^{-5} rad.

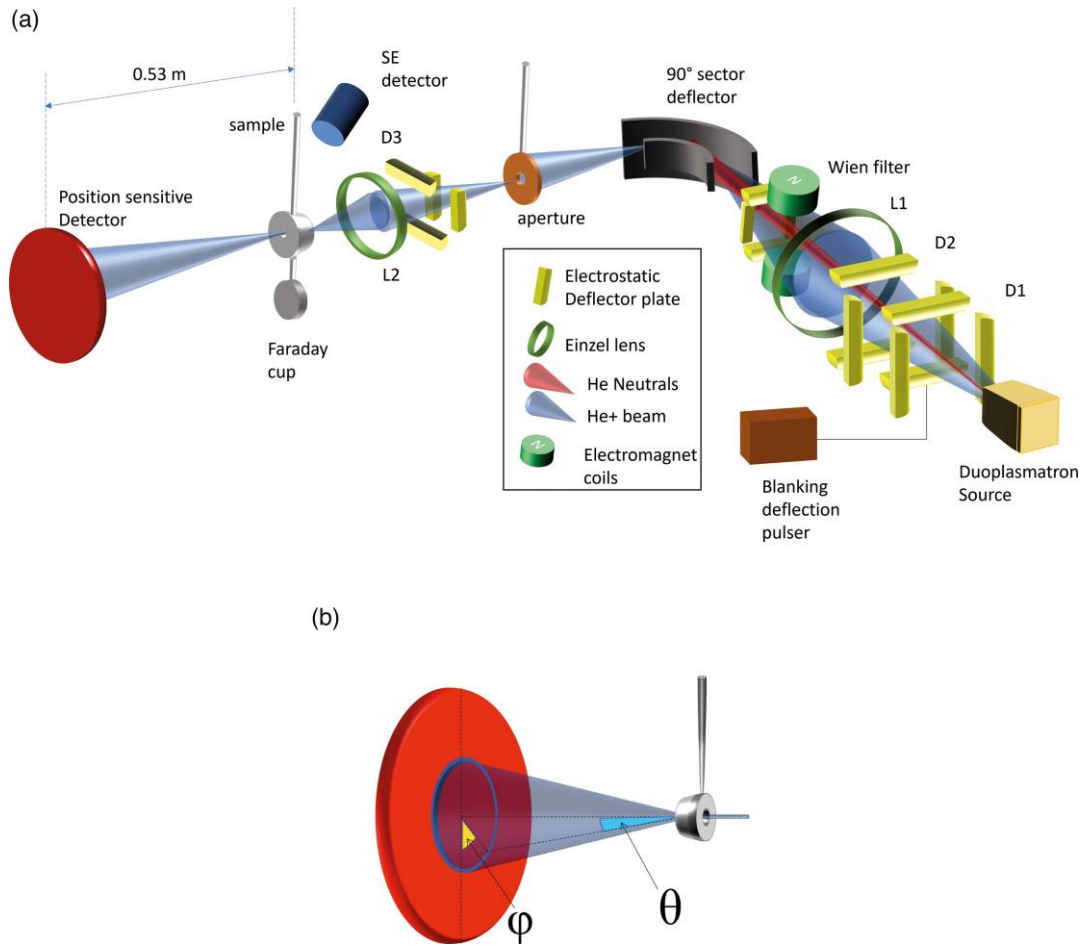


Figure 1.14: (a) Galileo prototype schematic. (b) The scattering geometry

During TOF measurements, the beam is controlled using the vertical deflector plates. The Ionoptika PUL03 fast pulser applies directly a 200 V pulse to the lower vertical blanking plate, which blocks the beam. The periodic unblanking occurs for a 100 ns time window.

The trigger pulse for unblanking serves as the start signal for TOF measurements. The detector generates four signals, one at each end of the two delay lines, which function as stop signals. With the start and stop signals, the TOF and impact position can be calculated for each event. The detector has the capability to record 3D datasets (θ , ϕ , t), as shown in the coordinate system diagram in Figure 1.14(b). Using these datasets, it becomes possible to create images by counting signals within a defined time frame and TOF spectra containing counts from a specific region of interest (ROI) within the sample area. During beam scanning, a (θ , ϕ , t) dataset is captured at every raster position, resulting in a 5D dataset containing a list of counts with complete (x , y , θ , ϕ , t) data. These data can then be utilized

to generate TOF spectra (t), images in the (x , y) sample plane, or images in the detector plane (θ , ϕ)[160].

1.3 Problem statement and objectives of the thesis

As we discussed the topic of transmission ion imaging extensively, there needs to be more studies to investigate the capabilities of helium ion transmission for nanoscale imaging and characterization purposes.

Before delving further into He^+ ion transmission imaging potential capabilities, it's crucial to acknowledge the limited research conducted on the **investigation of artifacts** that may arise in the process of **He^+ ion transmission imaging** or those stemming from sample preparation, which can influence the contrasts observed in He^+ ion transmission imaging. Note that sample preparation is usually done by heavier ions, such as Ga^+ in FIB instruments, which is common in FIB sample preparation for TEM samples. Artifacts, in this context, denote **alterations to the material's microstructure, morphology, and chemical composition** due to the ion beam's interaction with target materials. Such changes impact imaging contrast and result in misleading information about the sample properties. For example, the imaging signals for STIM originate from the sample's backside. Therefore, if the transmitted He^+ ion changes the material's characteristics on the sample's exit surface, it can create an artifact in transmission imaging contrast. Hence, our first objective is to conduct experiments using Ga^+ and He^+ ion beams with energies typically used in imaging and sample preparation to **investigate the exit surface** of two distinct samples. The details of this experiment are outlined in Chapter 3.

Another area with insufficient research is the exploration of transmission ion imaging at the nanometre scale resolution. The technique hasn't been thoroughly investigated to determine the extent of information it can provide, especially when there's the potential to correlate this information with other techniques like SE or SIMS, a dimension that remains unexplored. Thus, our second objective is to **explore novel contrast mechanisms He ion transmission imaging** techniques. Our optimal choice is the npSCOPE. This selection is primarily driven by its unique capabilities, encompassing correlative microscopy involving SE, STIM, and SIMS. What sets it apart is the instrument's nanometre-scale probe size, enabling transmission imaging with nanoscale resolution. This investigation of transmission

imaging contrast at such a high level of detail represents an unknown domain, and it offers an opportunity to uncover the types of information and contrast achievable with diverse samples within transmission geometry using He^+ ions. Additionally, it allows us to identify the strengths and weaknesses inherent in this imaging technique and determine the questions it can help address. Therefore, in chapter 4, we delve further into STIM imaging, and to enhance our understanding of STIM imaging contrast, we compare it with other imaging modes, including SE, Transmission Kikuchi Diffraction (TKD), or BSE. Moreover, in our research to explore correlative approaches involving STIM within npSCOPE and its integration with two other techniques available in the same instrument, we conducted a series of case studies focused on semiconductors in chapter 6. In these case studies, our initial attempt was to establish a **correlation between SIMS and SE imaging**. The ultimate goal was to extend this correlation to include **STIM**. However, it's worth noting that the successful correlation of these three techniques proved challenging and will require further investigation in the future.

ToF measurements offer additional valuable information (e.g., energy loss variations for different crystal orientations) achievable through transmission geometries. As a response to a research gap examining the transmission imaging capabilities of keV He^+ ions while simultaneously capturing the energies of transmitted ions, ToF measurements can help to gain further insights within Galileo, aligning with the energy ranges of transmission imaging in npSCOPE. This approach enables the acquisition of new information and novel imaging contrasts acquiring of 5D dataset while adding information to the 4D STIM imaging in npSCOPE. This objective has been addressed in chapter 5.

2 Chapter 2: Experimental

2.1 Nanofab HIM-SIMS

The NanoFab HIM-SIMS instrument used in this study is also a HIM prototype (Zeiss ORION NanoFab, Peabody, USA) like as npSCOPE. However, the SIMS add-on system is using a magnetic sector mass spectrometer system utilizing a multi-collector configuration. The multi-collector comprises four individual detectors, each equipped with a channeltron and a mass-to-charge ratio filtering slit at its entrance[161]. Further details about the working principles and comprehensive information about SIMS in this specific instrument can be found in the previous section.

2.2 Scios

The Scios system was employed to prepare thin lamella samples in chapter 3. Scios is a high-vacuum dual-beam FIB-SEM platform developed by Thermo Fisher Scientific, and commercially available [162]. It incorporates a vertically oriented SEM column with a field emission source, allowing landing energy of the electron beam ranging from 200 eV to 30 keV and providing a lateral resolution of 1-2 nm at 1 keV. The instrument includes subsystems for detecting SE and BSE signals. Ga-FIB is also part of the system, positioned at 52° relative to the perpendicular axis of SEM. The ion beam landing energy ranges from 500 eV to 30 keV in Ga-FIB, which offers a probe current from 1.5 pA to 65 nA. It serves various purposes, such as ion beam-induced SE imaging, milling, and patterning purposes, and analytical tasks like SIMS. The smallest achievable probe size is 3 nm at 30 keV. Additionally, specific GIS can be used for tasks like in situ platinum coating or precursor injection for fabrication purposes. The eucentric beam coincidence point is situated at 19 mm and 7 mm FIB and SEM WD, respectively. This positioning allows for tilt movements of the sample stage without lateral shift of the ROI. As a result, nanofabrication can be performed using the ion beam while simultaneously conducting SEM imaging of the same ROI.

2.3 Confocal Laser Scanning Microscope (CLSM)

The CLSM used in our experiments is the VK-X1100 Optical Profilometer, manufactured by Keyence. VK-X1100 is a laser microscope to measure surface roughness and film thickness at

nanometre-level precision. Laser microscopes employ a specialized optical system, which includes a light source, a light-receiving component, an objective lens, a half mirror, and a pinhole, employing the confocal principle to capture height information from the sample.

This instrument utilizes a 404 nm laser beam for two-dimensional scanning along the X and Y axes, dividing the field of view into pixels (1024×768 pixels). To facilitate vertical movement within a fixed range, a motor controls either the objective lens or the sample. Throughout this process, simultaneous data capture involves tracking the objective lens's position and monitoring the light received by the light-receiving element.

A crucial component, the pinhole, is positioned in front of the light-receiving element, serving to eliminate out-of-focus light and exclusively detect in-focus pixels. The lateral resolution of this system is around 120 nm, while the Z-resolution typically falls within the range of 6-8 nm.

2.4 SDTrimSP simulations

SDTrimSP is a Monte Carlo program designed for simulating ion interactions with a target material. It operates assuming that the target structure is amorphous or randomized, with atoms held at zero temperature and with an unlimited lateral dimension. The program employs the binary collision approximation to address atomic (nuclear) collisions, which means that the asymptotes of its real trajectory determine the change in the ion's flight direction resulting from a collision. SDTrimSP is used to calculate the damage formations and ion implantation ranges, which results from the interaction between impinging ions and the target material. Therefore, it is a useful technique to simulate the impact of ions on a target, which can be compared to our experimental results as a function of energy and impact angle, the ion dosage, and the target thickness. This method is used to compute the collision cascades in the target and simulate the sputtering processes, ion induced mass redistributions, sputter yield amplification, ion beam mixing and dynamic compositional changes[163].

We used SDTrim simulations[164] To understand and interpret our experimental results in chapter 3. The ion irradiation doses for simulations were slightly different than the experimental values (a re-check of the experimental conditions revealed a minor error in the dose calculation). The sample thicknesses for the simulations were varied according to

the fluence until forward sputtering observations. Therefore, a sample thickness of 150 nm, 200 nm, and 300 nm were determined for low, medium, and high doses. The parameters of the simulations of Ga on Si and Al can be found in Table 2.1 below. For He⁺ irradiation, the physical processes cause local density discrepancies due to the cavitation and higher concentration of “He bubbles” formation in the material. It should be noted that because He ions have a low mass, physical processes that take place during irradiation process prevent the Binary Collision Approximation (BCA) code—which we used—to be reproduced. For these reasons, He on Si and Al were not investigated computationally. Please note that, these calculations were performed by Grégoire Defoort and Patrick Philipp at LIST.

Sample	Ion's type	Ion energy (keV)	Angle of impact (°)	Fluence (ions. cm ⁻²)	Target thickness (nm)
Silicon	Gallium	30	45	7.9×10 ¹⁶	150
				1.5×10 ¹⁷	200
Aluminium				2.4×10 ¹⁷	300

Table 2.1: SDTrimSP simulations parameters

2.5 SRIM (Stopping and Range of Ions in Matter) and CASINO

SRIM is a software tool for performing calculations and simulations related to the transport of ions in various materials. This comprehensive software package encompasses the estimation of ion stopping and penetration depths within target materials, simulation of ion implantation processes, modelling of sputtering phenomena, analysis of ion transmission behaviours, and application in ion beam therapy[163]. SRIM is a versatile and indispensable tool for understanding and predicting ion interactions within different material environments. We used SRIM[155] software in chapter 5 to simulate the He⁺ ion-solid interactions using 25 keV for He⁺ primary energy and 50 nm Au membrane thickness. The ‘monolayer collision steps/surface sputtering’ type is employed for SRIM calculation. In addition, we used CASINO software (V3.3.0.4) (CASINO.

<https://www.gel.usherbrooke.ca/casino/index.html>). CASINO is a quantum Monte Carlo program, and we used it to simulate the interaction between electrons and solid materials, as well as transmission of electrons using a 30 keV electron beam with a diameter of 4.7 nm. The 'Mott by equation (Browning 1994)' physical model was used in the simulation, and the specimen was specified as a 500 nm x 500 nm x 50 nm slab of Au. SRIM and CASINO simulations were performed by Michael Mousley (LIST).

2.6 TKD (Transmission Kikuchi diffraction)

TKD is a scanning electron microscopy technique to obtain crystallographic information and orientation mapping at the nanoscale level. The TKD were obtained in a FEI Helios Nanolab600 FIB/SEM equipped with a Schottky field emission gun and an EDAX Hikari Electron Backscatter Diffraction (EBSD) camera at the University of Saarland with the support of Dr Christoph Pauly. The EBSD that is being used in this instance is a classical EBSD detector, and the designed geometries are for measurements of reflection rather than transmission. The tilt angle depends on a compromise for the best lateral resolution (at normal incidence) and what will adequately illuminate the EBSD camera screen (towards higher angles). The spatial resolution of TKD is often dependent on sample thickness and atomic number. Thin samples containing light elements produce the best resolution due to minimal electron scattering. A resolution of 10 nm or less has been reported in the literature[165]–[167], depending on the samples' thickness and atomic number.

For our experiments setup the voltage for acceleration was adjusted to 30 kV. Setting the voltage to 30kV aids in reducing the lateral scattering of the electron beam during transmission. Also, a beam current of 5.5 nA was employed. Under these conditions, the resolution of the SE mode image for the FIB/SEM was found to be 4.8 nm. The resolution was assessed using edge profile analysis on a tin ball calibration sample, and TKD images were obtained by tilting the sample stage. The tilted stage makes 25° angle between the sample surface and the incident electron beam. We used the software OIM Data Collection v7 to do the measurements, performed with different step sizes in the 5–7 nm range. Also, we employed EDAX OIM Analysis v7 for data analysis. To remove inconsistent data points, a standardization clean-up using grain contrast index (CI) was conducted, followed by a CI filter to exclude data points with a CI less than 0.09. Subsequently, each data set was

rotated. During the cleaning up, the measured orientations remained unchanged. We investigated the texture of the gold film, which was discovered to have {111} fibre texture. Considering that the strong pole in the centre of the {111} pole figure is attributed to {111}. Another characteristic is the ring created by individual poles at 70.5° . The angle of 70.5° represents the inclination between planes belonging to the {111} family within the cubic lattice. However, a local out-of-plane bending of the film was observed. The measured data showed a central pole that deviated from the pole figure's centre. This was observed from different {111} pole figures from additional ROI. To overcome the deviation from a flat surface and prevent misinterpretation, we rotated the dataset in OIM analysis to compare measured orientations between several ROIs. The final stage involved cleaning up the data to produce a single average grain orientation that could then be sent for additional processing. The same microscope was used for BSE imaging at 5 kV and 86 pA of beam current. The BSE images were acquired in immersion mode using a solid-state single-segment detector. To comprehend the interactions between ions and solids, as well as between electrons and solids, and their link to the experimental outcomes, we performed Monte Carlo simulations with parameters that would correspond to the parameters we used in the experiments.

2.7 ToF-MEIS (Time-of-flight medium-energy ion scattering)

The ToF-MEIS[168], [169] apparatus (Figure 2.1) at Uppsala University is a surface and near-surface analysis technique employing ion beams. ToF-MEIS was developed[170] based on principles similar to RBS's. However, the operational energy falls within the 50-500 keV range, categorized as medium energy. This range allows us to utilize the channelling and blocking techniques for direct surface analysis. The TOF-MEIS apparatus encompasses a beamline with a chopper system and an ultra-high vacuum chamber. This setup is linked to a 350 kV air-insulated accelerator provided by Danfysik. Successful transmission of ion beams to the MEIS configuration has already encompassed masses ranging from 1 to 51 atomic mass units.

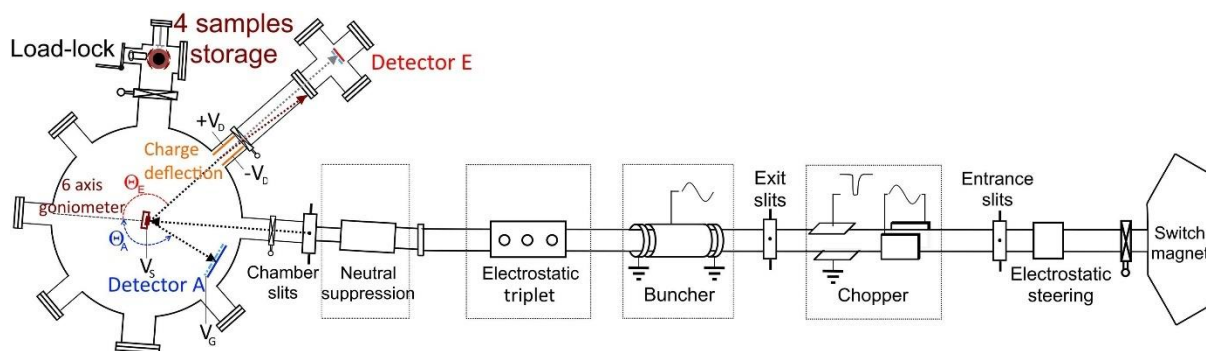


Figure 2.1: A top view of the ToF MEIS apparatus located at Ångström Laboratory, Uppsala University, is presented, highlighting the key mechanical components[168].

The accelerator generates ion beams, which are typically chopped into short pulses through an electrostatic chopper. This is accomplished by utilizing a gating pulse, leading to pulse durations that can be as short as 1–3 nanoseconds. A combination of slits positioned before and after the chopper, along with initial electrostatic steering within the beam line, is employed to achieve a focused, parallel pulsed beam. As a result, time resolution of 1 nanosecond can be attained.

The integration of multiple sets of horizontal and vertical slits enables the confinement of the beam's cross-sectional area to dimensions well below $(1 \times 1) \text{ mm}^2$. This setup also delivers a notably superior beam divergence of less than 0.056° . To provide a point of comparison, even the smallest utilized membranes possess an area of $(3 \times 3) \text{ mm}^2$. Particle ToF is measured from the chopper gating electrode to the detector. Two turbo pumps maintain the beamline at a pressure of approximately $3 \times 10^{-6} \text{ mbar}$. One pump is positioned before the chopper, while the other is placed prior to neutral suppression. Consequently, the incident current on the sample can be minimized to a 2–3 fA. Within the experimental chamber, the base pressure measures below $1 \times 10^{-8} \text{ mbar}$. It's important to note that no specific on-site sample cleaning procedures were carried out for the experiments presented in ToF-MEIS. Each ToF detector is an MCP-DLD sourced from Roentdek. The configuration features a delay-line anode detector, which features a 60 mm diameter DLD behind the sample. This setup collects the transmitted ions/neutrals. Additionally, an auxiliary DLD is used to enhance energy resolution.

The TOF-MEIS system was configured for pulsing and chopping, aiming to attain a pulse width of around 1 nanosecond. This was verified by examining the undisturbed beam and consistently confirmed during the experiments by assessing the photon peak width. It's

important to highlight that the images generated by the DLD exhibit several lines, a result of the detector's construction, and these lines are not indicative of the actual data for the channelling patterns (refer to Figure 2.2).

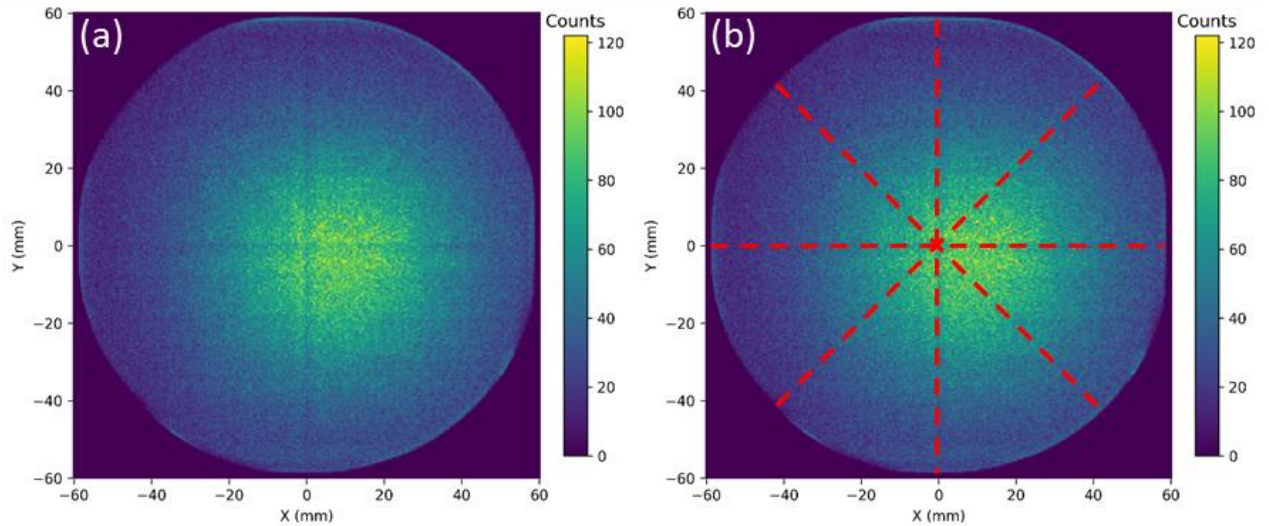


Figure 2.2: Examples of the lines present in the channelling images due to characteristics of the detector's structure. a) displays the collected data, while panel b) emphasize the line positions.

The time-of-flight for an impact is measured from the chopper gating signal to the MCP, covering a flight distance consisting of the distance from the exit slits to the target ($L_1 = 7$ m) along with the target-to-detector distance (L_2).

The energy information is derived from the ToF, leading to an enhanced energy resolution for longer flight times. For instance, proton detection at 100 keV will result in an energy resolution of approximately 0.9 keV with a time resolution of 0.3 ns. Specifically, this improvement is observed at lower beam energies and when heavier projectiles are used.

In our experiments, transmission mode in ToF-MEIS was performed as the default setup for our energy-loss experiments chapter 5. Another setup is employed for backscattering. In this configuration, the detector was positioned in front of the sample to establish a direct line of sight with the sample surface. This setup enables the creation of a backscatter spectrum, where the arrival time of the backscattered ions changes based on the mass they interact with and the depth of their backscattering within the sample.

2.8 Electrochemical Capacitance-Voltage (ECV)

ECV profiling method is utilized for assessing active carrier concentration profiles within semiconductor layers. This technique establishes a depletion region at the electrolyte-

semiconductor Schottky contact, creating a capacitor-like structure with ionized donors and electrically active defects or traps. Measuring the capacitance offers insights into doping and electrically active defect densities, and depth profiling is accomplished by electrolytically etching the semiconductor, without limitations on depth.

In our experimental setup, ECV measurements were conducted employing the ECV CVP21 instrument from WEP. Cleaved sample pieces, measuring approximately $2 \times 2 \text{ cm}^2$ in size, were used. The etchant used was a $0.1 \text{ mol l}^{-1} \text{ NH}_4\text{F}$ solution.

2.9 X-ray photoelectron spectroscopy (XPS)

XPS referred to as electron spectroscopy for chemical analysis, is a method employed to examine the surface chemistry of a material, enabling the measurement of both the elemental composition and the chemical and electronic states of the constituent atoms within the material.

In our experiments, XPS depth profiles and Ultraviolet Photoelectron Spectroscopy (UPS) measurements were conducted using an Axis Supra (Kratos Analytical) instrument. XPS measurements employed a 20 eV pass energy and a 0.1 eV step size, with the samples grounded to minimize charging effects. To obtain XPS depth profiles, 2 keV argon ions were used, and the sputter rate was calibrated on the perovskite material. Subsequent etching steps were defined at depths of 0, 11.25, 22.5, 45, 90, 135, 180, 225, and 270 nm. The XPS depth profiles were acquired with an 80-eV pass energy and a 0.2 eV/step. To mitigate Ar^+ beam-induced damage, a low-energy electron flood gun was employed to charge-neutralize the sample during measurement. UPS measurements utilized He I radiation at 21.22 eV, with a pass energy of 10 eV and a step size of 0.025 eV. Similar to XPS, the samples were electrically grounded in all cases to minimize charging effects.

2.10 J-V curve measurements

J-V property assessments performed under standard test conditions utilizing a class AAA Wacom sun simulator equipped with two lamps (halogen and xenon). To ensure accuracy, we employed independently certified SHJ cells for the calibration of our in-house solar simulator. For precision, shadow masks were utilized to delineate an illuminated region measuring 0.25 cm^2 for single-junction cells and 1.21 cm^2 for tandem cells. The

measurements were executed with a scan rate of 100 mV/s, which included an integration time of 0.1 seconds and a 0.1-second delay for each data point. The voltage step size was set at 0.02 V. Additionally, a three-point weighted maximum power point tracking measurement was carried out, facilitated by a LabVIEW code developed in-house. In the case of tandem cell measurements, the cells were positioned on a temperature-controlled stage held at a constant 25°C.

3 Chapter 3: Irradiation damages investigations with Ga^+ and He^+ ion beams

This chapter describes the experiments to study the interaction of the He^+ and Ga^+ ions with crystalline Al and Si thin films. In this regard, the experimental approach investigates the morphology on the back and the front side of the irradiated region. Ga FIB was used to prepare the electron-transparent samples and TEM, as well as CLSM, were used to characterize the FIB-induced modifications in samples. The thickness of the samples (300 nm) and the energy of the ions (25 keV) were identical for all samples, but the applied ion doses were varied and categorised as low, medium, and high doses.

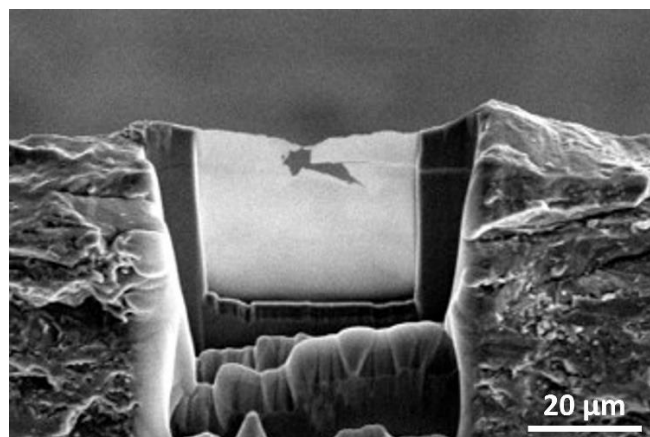
Despite existing research on the effects and artifacts of Ga^+ ion irradiation that were discussed in section 1.1, there needs to be studies addressing alterations in the morphology of the thin film's backside (< 300 nm thickness) following ion irradiation. We are particularly concerned about these changes to the backside of thin films, as our research will centre on transmission imaging. Transmission imaging is significantly influenced by the exit surface of ions, i.e., the backside of the samples such as those used in STIM imaging. This is the primary motivation behind our interest in examining the rear surface of the sample. Additionally, our choice to study two types of ions, Ga^+ and He^+ , stems from practical considerations. We use Ga^+ ions for sample preparation in transmission imaging, mainly found in FIB instruments. Furthermore, we have selected He^+ ions because we intend to employ helium ion transmission imaging techniques. Hence, in this Chapter, we will focus on the effects due to Ga^+ and He^+ irradiation in thin films.

Silicon as a simple material to investigate, is a significant material in He^+ irradiation investigations. Moreover, Silicon is backbone in semiconductor industry as it is essential for the development of radiation-hardened electronic devices[171] and enhancing the reliability of semiconductor materials in radiation-intensive environments. Additionally, the study of irradiation effects on Silicon holds significance in various other fields, such as material science[27], [30], [31] and nuclear technology[172], [173] For instance, Silicon serves as a neutron multiplier or target material in nuclear reactions, leading to the production of helium as a by-product of neutron irradiation. Al (mass 27) was chosen as the second model sample as it has a mass similar to Si (mass 28), but a different crystal structure (Al is face-

centred cubic, while Si has a diamond cubic structure) and nature of bonds (Al has metallic bonds, while Si has covalent bonds). Therefore, Al and Si are interesting model samples to compare. Comparing Si and Al, we observe differences in bond formation and crystal structure. Previous studies[174], [175] have demonstrated that, due to the more close-packed structure of Al atoms, they are less prone to displacement than Si. Further research[176], [177] has indicated that in the case of Si undergoing amorphization, a significant number of atoms can experience permanent displacement over distances smaller than the interatomic separation, as well as large displacements. However, since pure metals do not undergo amorphization, such minute displacements are not achievable in Al[178]. Additionally, the reaction of Al's surface to radiation is considerably slower, as it necessitates the creation and accumulation of permanent defects to bring about noticeable alterations in surface morphology[179].

3.1 Sample preparation workflow

Two sets of samples were prepared, one from hyper pure polycrystalline Silicon and another from annealed Aluminium. Polycrystalline Silicon was selected as a model sample to study the ion-matter interactions. To make a comparison, annealed Aluminium foil was used as another model sample. For the sample preparation process, the Si and Al samples were polished to make thinner parts to be easy for TEM analysis. The $50\text{ }\mu\text{m} \times 50\text{ }\mu\text{m}$ samples of Al and Si (Figure 3.1) with 300 nm thickness were prepared on a TEM sample support frame by rough milling using a Ga^+ ion beam in Scios. To remove the severely damaged and amorphous layer created by high current Ga^+ ion beam, final smooth polishing was done for both sides. The smooth polishing was done for 2 minutes with an 8 keV Ga^+ ion beam and 75 pA current for 2 minutes.



After sample preparation, one set of samples was irradiated with helium ions in a Zeiss Orion microscope with a 0° incidence angle. Squares of 10 $\mu\text{m} \times 10 \mu\text{m}$ were scanned by a roughly 14 pA of He^+ FIB current with 1 μs dwell time within 512 \times 512 pixels frame size and 25 keV beam energy. Likewise, Ga^+ ion irradiations were performed in Scios with a 45° angle with respect to the sample surface. The frame consists of 512 \times 442 pixels and the samples are exposed to 1 nA of Ga^+ FIB current with 1 μs dwell time and 25 keV beam energies in three different doses. Table 3.1 shows the applied doses for experiments.

Ion dose	Experimental values (ion/cm ²)
low dose	5.2×10^{16}
Medium dose	1×10^{17}
High dose	1.6×10^{17}




Table 3.1: Ion doses exposed to the Al and Si samples in experiments.

3.2 Results and Discussion

3.2.1 Focused Ga^+ ion beam exposure

Figure 3.2 shows TEM images of polycrystalline silicon FIB-prepared lamella after Ga^+ irradiation. High resolution TEM analysis was performed on the irradiated samples by the FEI Tecnai F20 at 200 keV in LIST. Please note that the TEM image from non-irradiated Silicon samples is shown in Figure 3.15(a). The irradiation was performed in three doses, as shown in Table 3.1, resulting in an increase in defect density with increasing dose in TEM images. Furthermore, diffraction patterns are shown in Figure 3.2 (d, e, f). A low amount of amorphized material is seen in low-dose sample (Figure 3.2 (a)). However, the crystalline structure is largely unaffected, and the faint rings can be attributed mainly due to amorphization at the surfaces due to sample preparation Figure 3.2 (d). The diffraction patterns of medium and high-dose exposed samples show progressive transformation of polycrystalline to amorphous Silicon. Silicon amorphization is more prominent in the medium dose diffraction pattern (Figure 3.2 (e)), and at the high dose (Figure 3.2 (f)), the crystalline structure of Si transformed entirely to an amorphous phase. Figure 3.2 (c) shows

a significant change in the crystal structure in the high dose exposed sample, with noticeable bend contour formation towards one edge and a thin remaining amorphous material (mostly in the centre). The bend contour could be attributed to local residual crystallinity. The high density of imperfections is consistent with lower atomic density of Si, which facilitates the displacement of atoms and defects formation. Comparing the bordering non-irradiated area in Figure 3.2 (a) and Figure 3.2 (b), the defects not only emerge in the irradiated area but also in the neighbouring grains, presumably to overcome the induced strain created by the volume change in the irradiated region.

TEM images of medium and high-dose Ga⁺ ion irradiated Aluminium samples are shown in Figure 3.3. The irradiated area's crystallinity in Figure 3.3 is similar to the pristine sample. The unvaried structure indicates a strong tendency of Aluminium to remain crystalline.

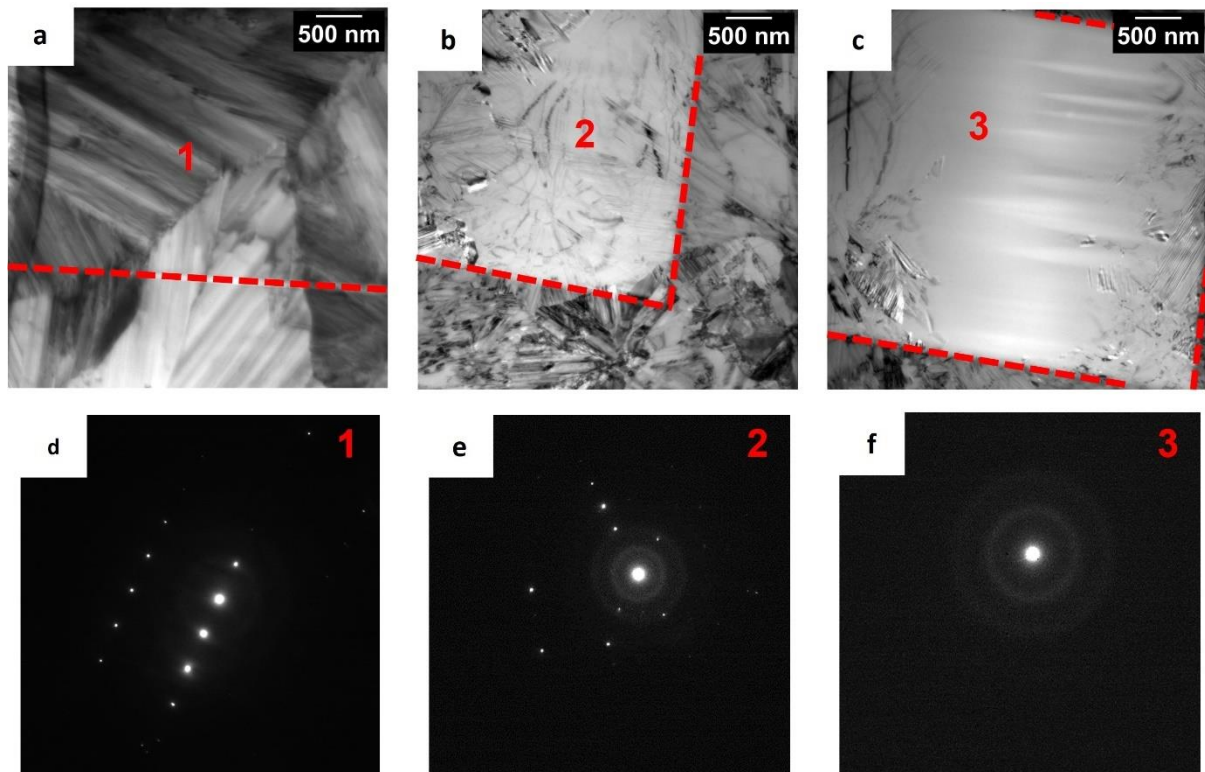


Figure 3.2: TEM images of a) low dose b) medium dose c) high dose irradiated Silicon 300 nm samples. Figures d, e and f are diffraction patterns obtained from the irradiated area shown in Figures a, b and c, respectively.

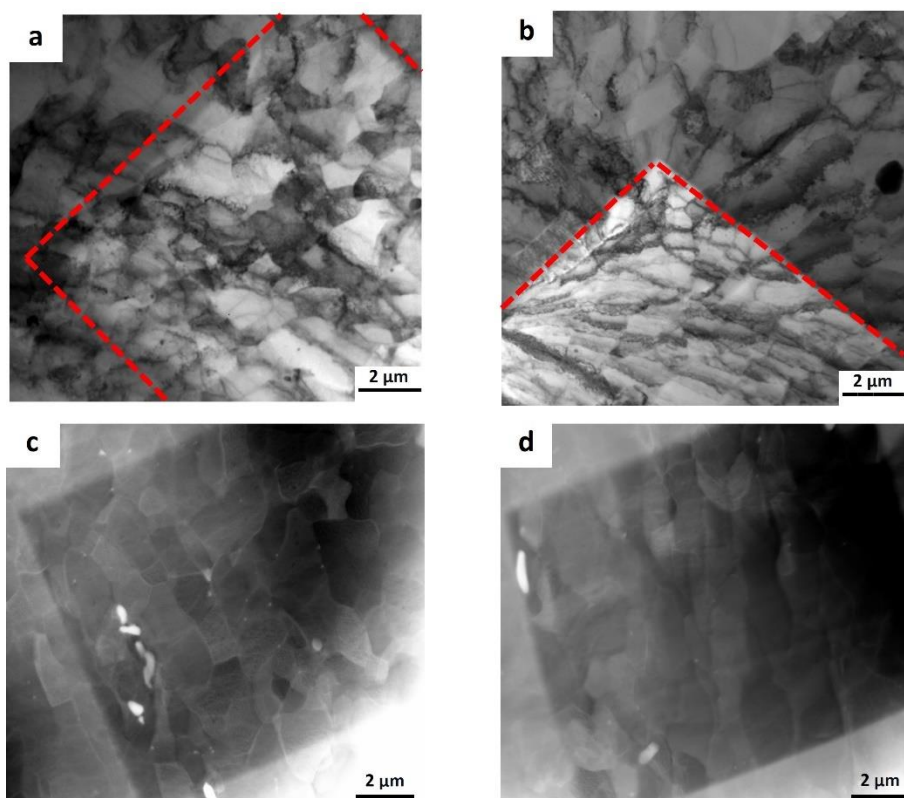


Figure 3.3: TEM images of a) medium dose b) high dose Ga^+ irradiated Aluminium 300 nm samples, and STEM images of c) medium dose d) the high dose Ga^+ irradiated Aluminium 300 nm samples

Figure 3.4 (a, b) present the CLSM images, which is used to show the topographic changes in the Ga^+ irradiated Silicon samples. The images illustrate the front and backside of the FIB-prepared lamella Silicon (Figure 3.4 (a, b)), which contains craters formed after high and medium dose Ga^+ ions irradiation. The front and back side images have been zoomed in Figure 3.4 (c, d) to reveal a better understanding (Arrows one and two points to the high and medium doses, respectively). The red dotted lines in Figure 3.4 (c, d) indicate the approximate FIB-prepared lamella area with roughly 300 nm thickness. Similar results for Ga irradiation in Al are given in Figure 3.5. A schematic (Figure 3.6) illustrates the morphological change in the front and back sides of the Al and Si samples discovered by CLSM images to better comprehend the CLSM images. The overall phenomena are sketched in more detail in Figure 3.6 (a, d), outlining the morphological change. As shown in Figure 3.6 (a), in low dose Ga^+ ion beam irradiation of Si, the material sputtered and created a 59 nm surface step. The back side did not undergo any morphological change. However, a change on the backside is seen for both medium and high dose exposed samples (Figure 3.6 (b, c)). In the high dose exposed sample, a depth of 507 nm was found on the front side of the crater's edge (Figure

3.6 (c)). Moreover, because of the apparent bulging on the back side, the crater's depth has a 516 nm height difference at the back. Additionally, the bulging on the top surface was seen with a 47 nm step in the centre of the irradiated area in the medium dose exposed sample Figure 3.6 (b). Correspondingly, a 239 nm height difference is present on the back side in the middle of the irradiated area. Although, on the crater's edge, a 128 nm step was created on a top surface because of sputtered material. As shown in Figure 3.6 (d–f), in contrast to the Silicon samples, the morphology of the back side of the Aluminium samples is analogous in high and medium dose samples (Figure 3.5). The overall backside morphology of the samples remained same as they all sputtered away from the surface. Furthermore, as a consequence of sputtered material from surface, a step of 70, 137, and 250 nm can be seen on the samples' front side from CLSM analysis which is shown in Figure 3.6 (d–f). According to TRIM simulation results, 6.8 Al atoms per Ga^+ ion and 5.2 Si atoms per Ga^+ ion are sputtered away which are compatible with the observations of the higher crater depth in Al samples compared to Si.

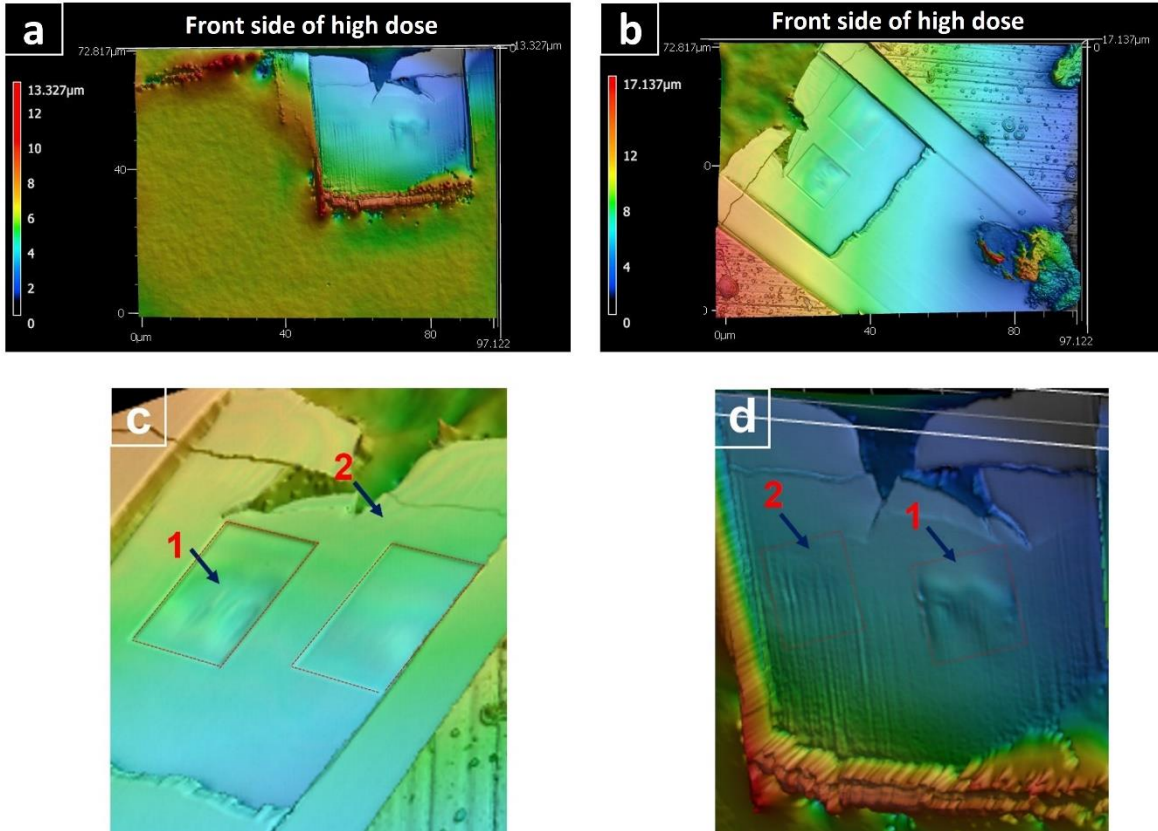


Figure 3.4: CLSM images for high and medium dose Ga^+ irradiated Si samples (a) front side (b) backside, (c) and (d) are zoomed in views of (a) and (b) respectively. Arrows one and two point to the high and medium doses, respectively

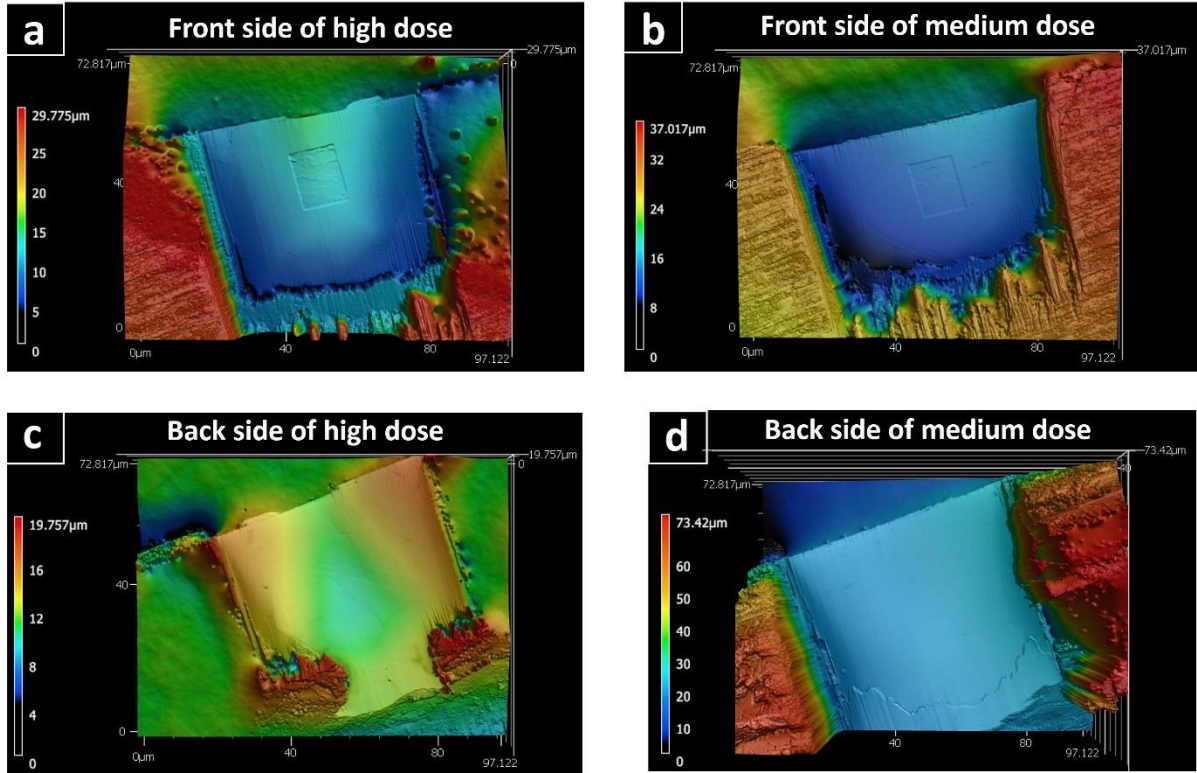


Figure 3.5: CLSM images of Ga⁺ irradiated Al samples (a, b) front sides (c, d) backsides for high and medium doses, respectively. The shift in colour observed in the central portion of the lamella-prepared sample in (a, c) is attributed to a slight curvature in the middle of the lamella, although this does not impact the outcomes of our experiments.

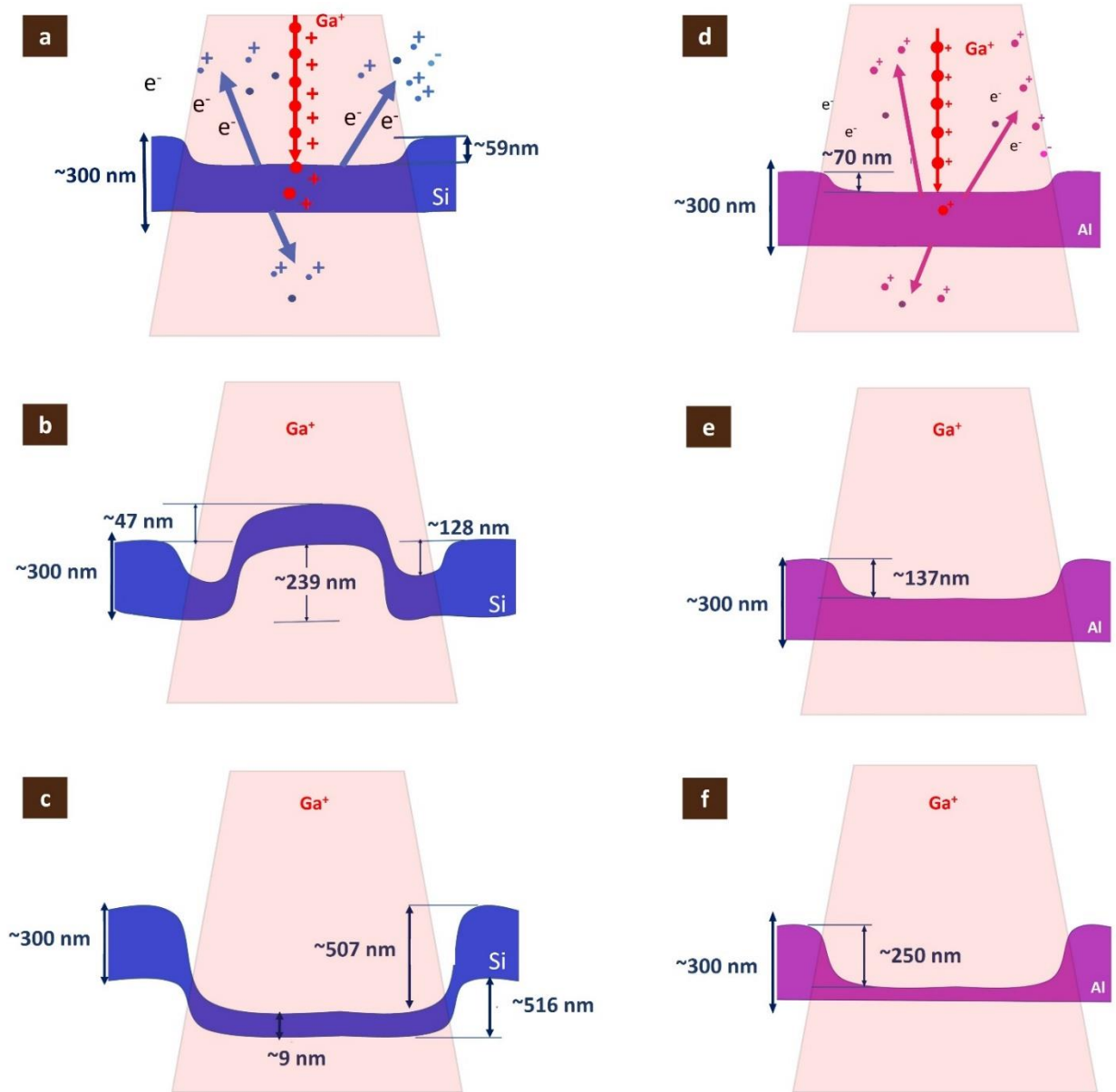


Figure 3.6: Schematic illustration of topographic evolutions observed after (a, d) low dose (b, e) medium dose (c, f) high dose Ga^+ ion irradiation on Si (left) and Al (right).

For further discussions on observed morphological changes on Ga^+ exposed Silicon and Aluminium, we used SDTrimP simulations. The simulations helped us to determine several parameters such as crater depth, crater recession, concentration of implanted Ga^+ in the sample in the crater, forward sputtering yield, normal sputtering yield, and Ga^+ ions transmission. To accurately determine the noted parameters, the particles were tracked from the surface and the back end of the sample. The samples for all doses were initially given the same 300 nm thickness, but no forward sputtering was noted. Forward sputtering

represents atoms scattered from the back of the sample, which could cause a morphological change on the backside. So, we took this hypothesis as a starting point and adapted the thickness of the sample to the dose to observe forward sputtering. As a result, we used three different sample thicknesses for low, medium, and high doses.

The simulation results (Figure 3.7) for Ga^+ irradiation on Si and Al samples, respectively, shows that the forward sputtering observed for the low dose is extremely small due to the insufficient dose to sputter through an adapted sample thickness of 150 nm. The breakthrough observed in medium dose (200 nm thickness) shows the higher forward sputtering yield in both Si and Al. Also, the lower forward backscattering of high is sort of an artifact of simulations due to the higher thickness of the high dose exposed sample. Ga^+ ions must travel a longer distance to reach the exit surface on the backside when the thickness is greater.

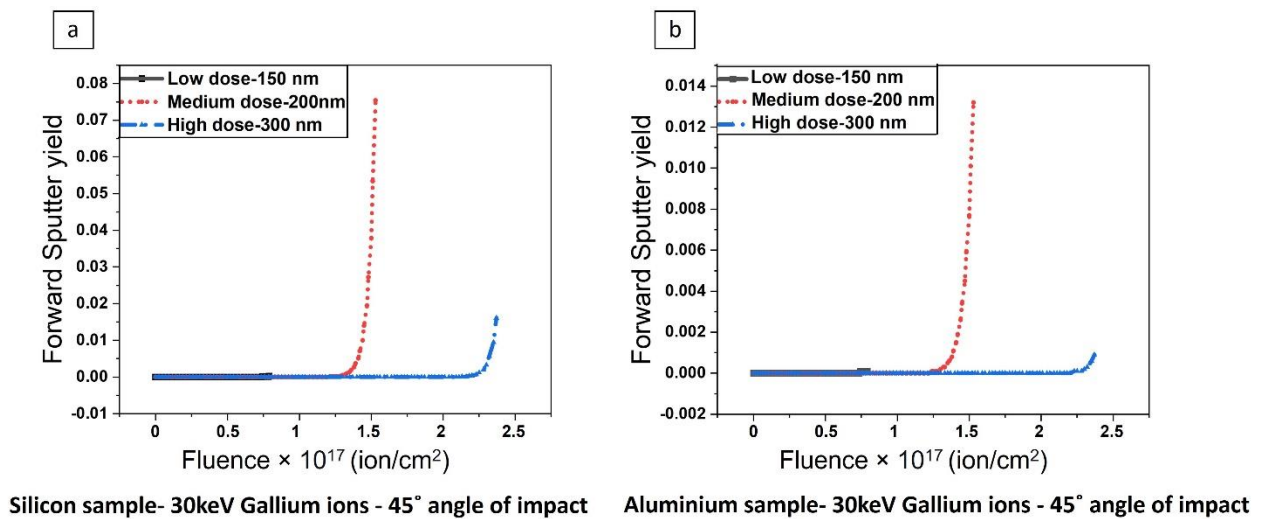
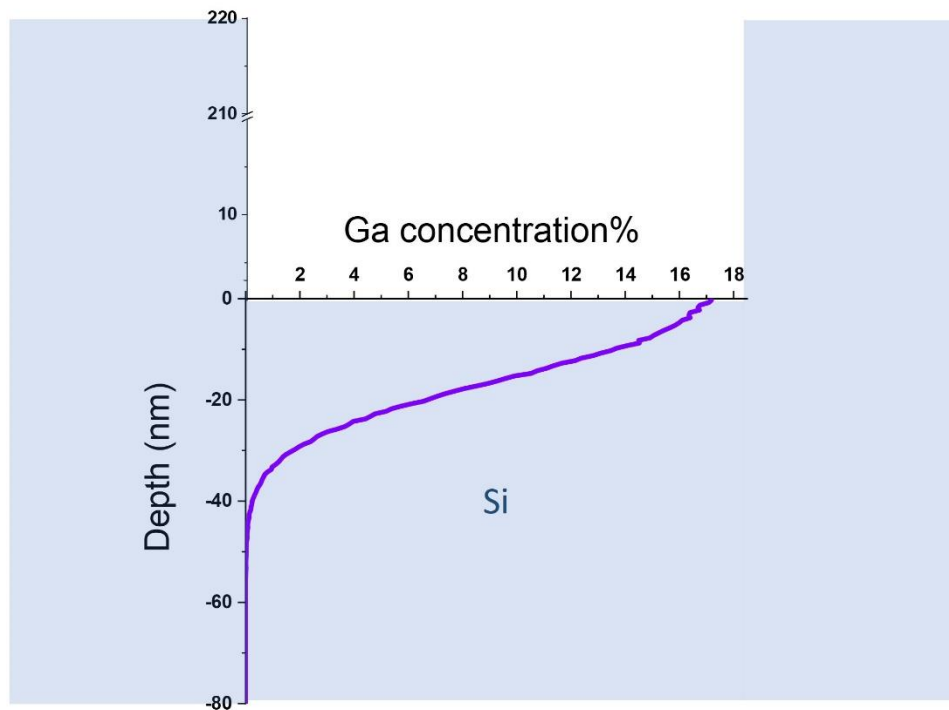


Figure 3.7: Simulated forward sputtering yields for each dose for (a) Silicon and (b) Aluminium.

Figure 3.8 (a, b) shows the simulated Ga concentration profiles plotted as a function of depth for Si and Al samples after high dose irradiation. As we can see for both samples, the evolution of Ga concentration from the surface toward the bulk is appearing, and regardless of the Ga^+ fluence the concentration profile is similar. The concentration of Ga on the bottom of the crater is 17% for the Si sample. Also, for the Al sample the concentration of Ga at the bottom of the crater is 15% Ga. In addition, we observed a slight surface effect in Figure 3.8 (b), a higher Ga concentration at the bottom of the crater in Al sample than in Si. This is likely a simulation artifact. In Figure 3.9 we plot the predicted recession of the crater on the front side formed by the sputtering of the sample since the recession depth allows us

to track the crater bottom. The results show identical trend but a variation from actual experimental results (Table 3.2). As the crystalline structure is neglected in simulations, the predicted recession depths appear to be inconsistent with experimental measurements.

a



b

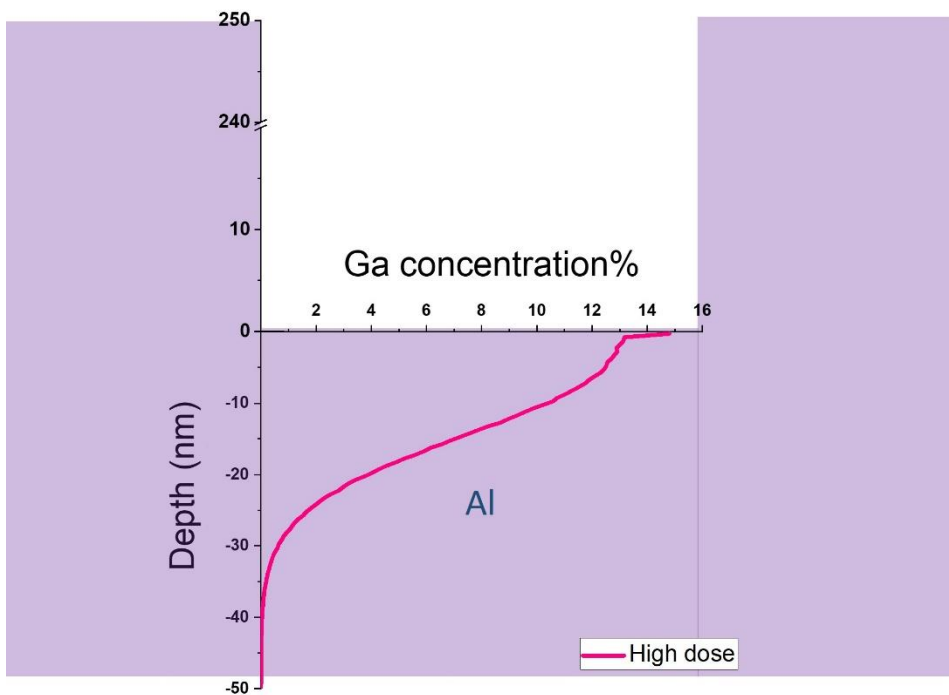


Figure 3.8: Concentration measurements at the bottom of the craters for high dose Gallium irradiated (a) Silicon and (b) Aluminium.

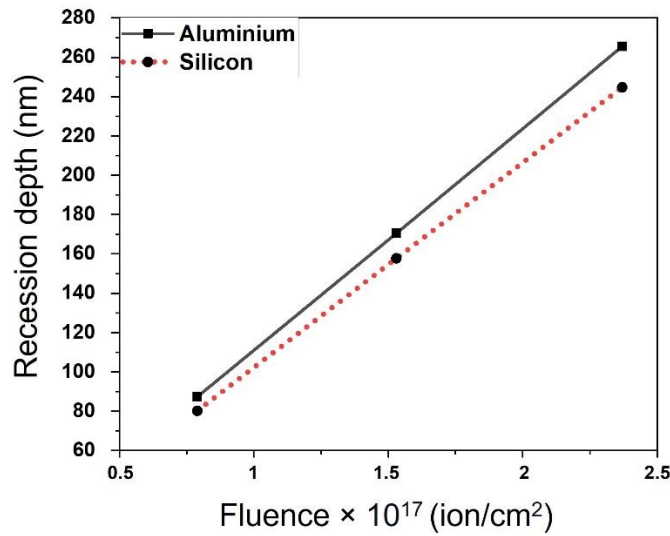


Figure 3.9: Simulated recession for Silicon and Aluminium samples with respect to the fluence

Sample	Low dose (nm)	Medium dose (nm)	High dose (nm)
Si experimental	59	128	507
Si simulation	80	145	220
Al experimental	70	137	250
Al simulation	90	170	250

Table 3.2: Recession depth on the front side after Ga⁺ irradiation

Transmission yields of Ga in Si and Al as a function of irradiation dose are shown in Figure 3.10. The Gallium transmission observed at high doses occurs at 1.99×10^{17} ions/cm² for Si, and 1.9×10^{17} ions/cm² for Al for a sample thickness of 250 nm. Moreover, a greater sputtering rate of aluminium would result in a reduced required dose of gallium ions to reach the sample's exit surface. This explains why gallium ions can transmit at lower doses in Aluminium. Additionally, the slightly higher back-scattered gallium in silicon serves as additional reason (Figure 3.11). Furthermore, Figure 3.12 shows the phase diagram of Gallium in Aluminium and Silicon. As it is obvious Ga dissolves more in Al than in Si, however the higher solubility of Ga in crystalline Al is not taken into account in the simulations, which can also decrease the transmission in parallel. Furthermore, the phase diagram indicates the lower melting point of the Al, which is proof of a higher sputtering rate of Al due to the weaker atomic bonds. So, in Al samples, Ga⁺ ions are less likely to pass through the material since they collide and dissolve within the target atoms. The sample becomes thinner as the

dose rises, making it simpler for Ga^+ ions to pass through the material. In experimental results, we should consider the impact of the crystal structure on the channelling process of Ga^+ ions since this would affect the transmission process. More transmitted atoms and channelled Ga^+ ions can interact more on the backside, producing a rough morphology even at lower doses.

The final thickness for simulation results in high dose irradiated Si and Al samples with 300 nm thickness are 80 and 50 nm (Table 3.2), respectively. While for experimental results, the remaining sample thickness is ~ 9 and ~ 50 nm (Figure 3.6) respectively. This is consistent with the explanation mentioned above regarding the channelling of Ga^+ ions in Si, which results in higher transmission, forward sputtering, and thinner samples compared with simulations. On the other hand, there is a very good agreement between the predicted and experimentally determined final sample thickness for the Al sample.

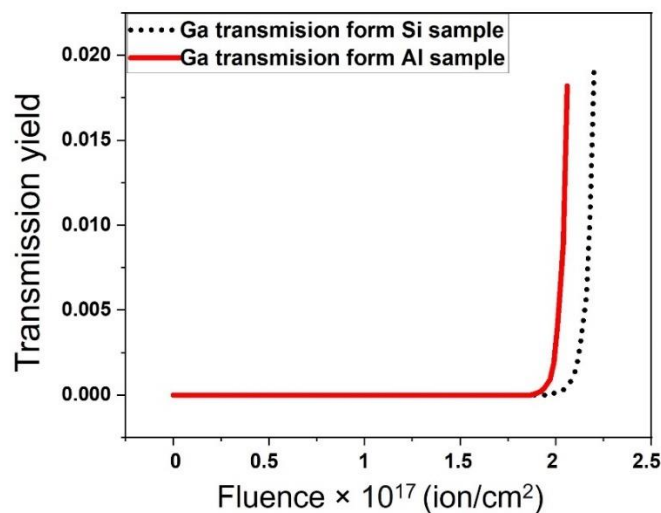


Figure 3.10: Transmission of Gallium for the high dose in 250 nm sample for Silicon (black dotted line) and Aluminium (red line)

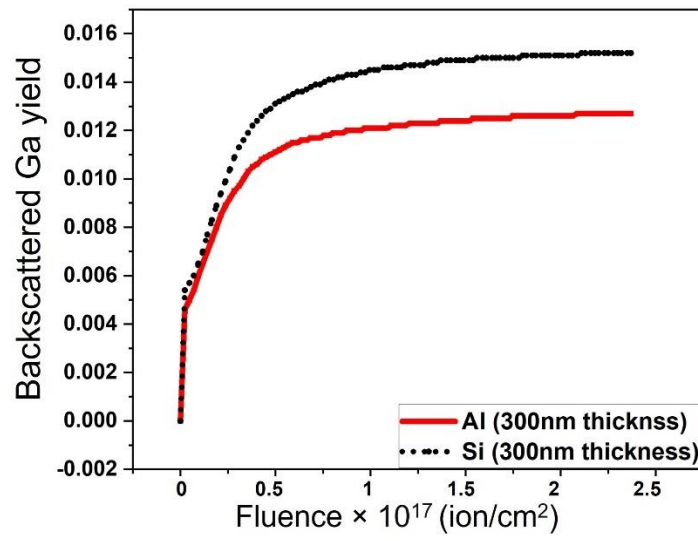


Figure 3.11: Backscattered Ga from Al and Si 300 nm samples

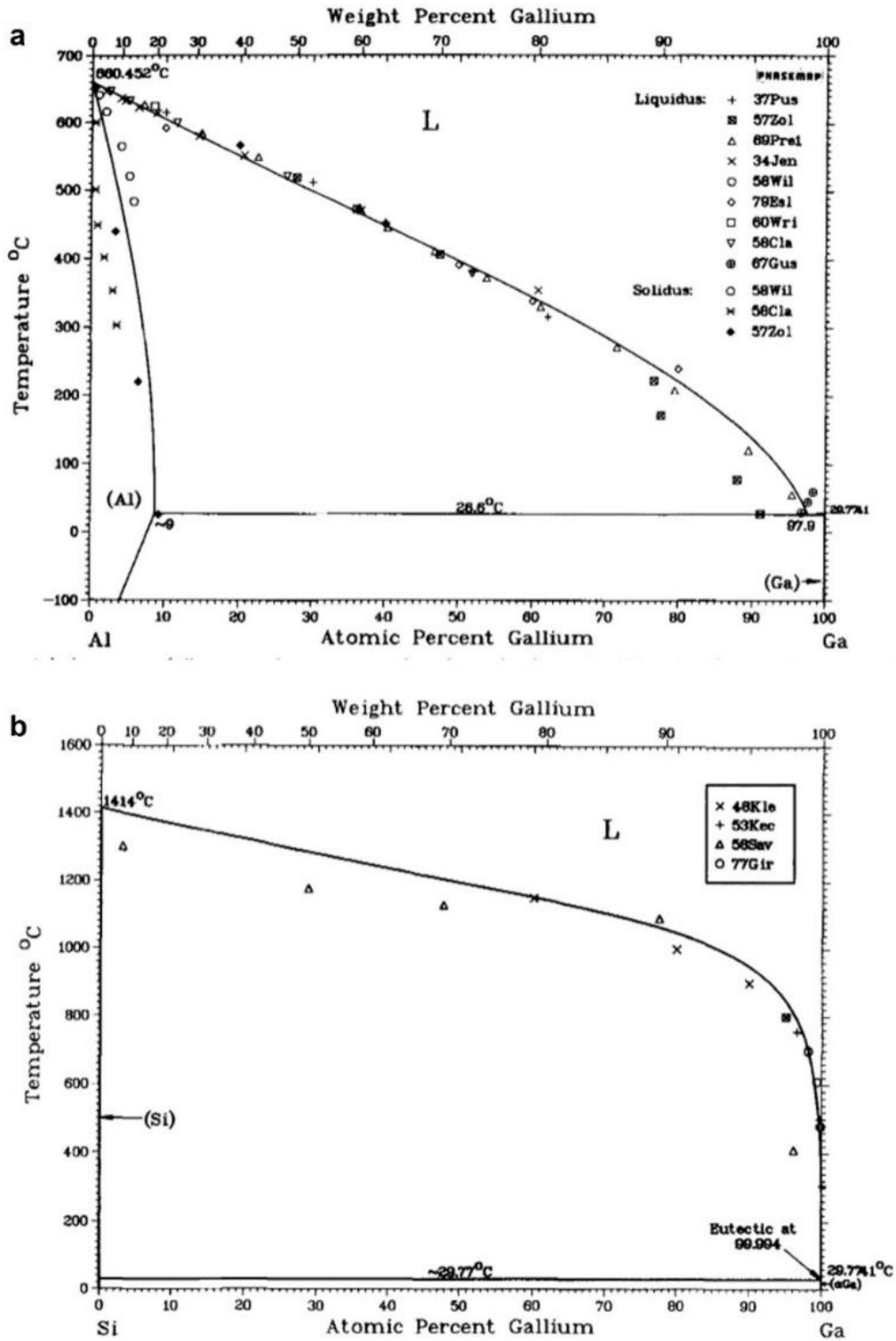


Figure 3.12: Phase diagram of a) Al-Ga[180] b) Si-Ga[181].

3.2.2 Focused He⁺ ion beam exposure

TEM images of Silicon and Aluminium lamella samples after He⁺ irradiation is shown in Figure 3.13 and Figure 3.14, respectively. Although the same doses as Ga⁺ irradiation were applied in He⁺ irradiation (Table 3.1), the images reveal only a little change of crystal

structure in the irradiated region in both Si and Al samples. The apparent difference in Si samples is the darker contrast, which should get lighter as it goes thinner in the irradiation region (Figure 3.10 (a, b, c)). The darker contrast could be due to the hydrocarbon deposition during He irradiation, as it forms an amorphous layer (compare the diffraction patterns of Figure 3.13 (d) with Figure 3.15(a)). The amorphous hydrocarbon layer decreases the intensity of transmitted electrons which explains the darkening seen in the irradiated areas, while the pristine areas appear brighter as they are thinner. The hydrocarbon deposition was observed in Si but not in the Al sample. Note that the chamber had been plasma cleaned prior to both Si and Al samples irradiation; however, because the samples had been exposed to various conditions—different chambers and distinct days of the experiment—for the Si samples, some contaminations may have remained in the chamber.

Regarding diffraction patterns (Figure 3.13(d, e, f)), no discernible crystallographic change was observed in the silicon samples. Furthermore, after He^+ beam exposure, in low dose irradiated sample, the amorphous material (attributed to hydrocarbon) is noticed which stayed approximately same in all three doses of Silicon samples. Nevertheless, the amorphous material was not observed in any of Al samples according to their diffraction patterns (Figure 3.14 (d, e, f)).

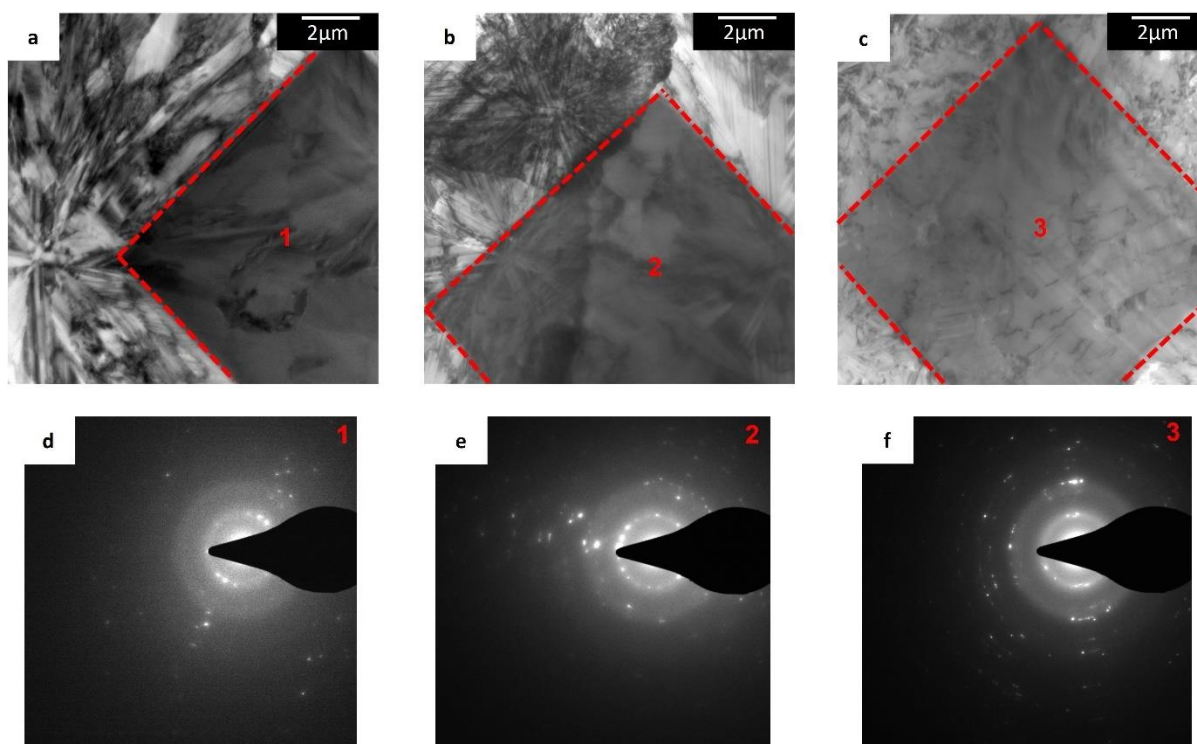


Figure 3.13: TEM images and diffraction patterns of ~ 300 nm Si samples after (a, d) Low dose, (b, e) medium dose, (c, f) high dose He⁺ irradiation.

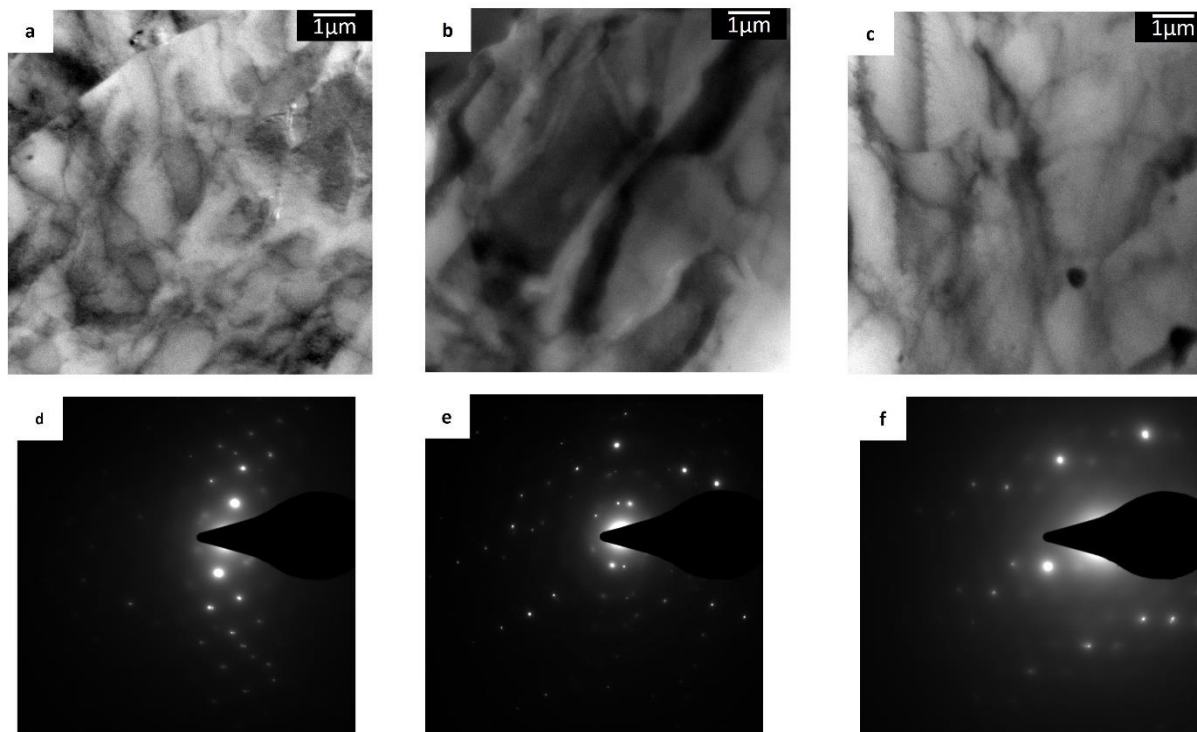


Figure 3.14: TEM images and diffraction patterns of ~ 300 nm Al samples after (a, d) Low dose, (b, e) medium dose, (c, f) high dose He⁺ irradiation.

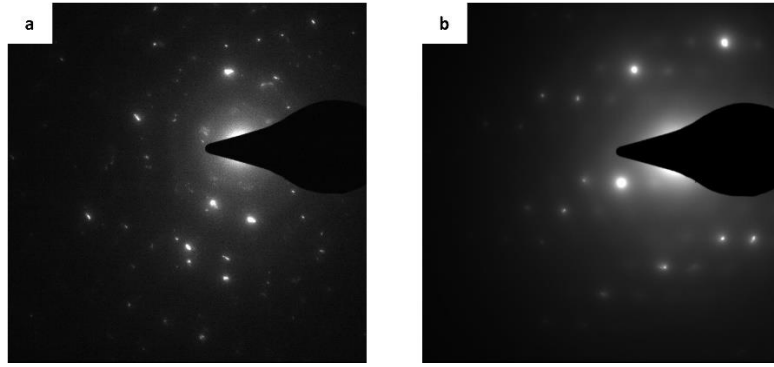


Figure 3.15 : Diffraction patterns from non-irradiated (a) Si, (b) Al.

The schematic in Figure 3.16 briefly displays the CLSM results on silicon samples subjected to helium ion irradiation. An approximate 160nm of crater depth observed in high dose irradiated Si. The crater locations in medium and low dose were noticeable in CLSM, however the depths were too small to be measured precisely. According to the results, neither the amount of amorphous Si nor the exposure to ion dose was sufficient to cause deformation or bubbles. For bulk Si, it has been widely reported that exposure to high dose of He ions results in bubble formation. In literature[29] a distinct behaviour has been observed with 32 keV He⁺ ions irradiation on a bulk Si sample covered in a protective layer, which prevents the He⁺ ions from escaping the sample. Some dislocations in the 1×10^{16} ion/cm² dosage exposed sample began in an area within the ion-stopping range. They also reported significant dislocation band between 150 nm and 310 nm subsurface developed in 5×10^{16} ion/cm². As the ion dose increased to 5×10^{17} ion/cm² nanobubbles with a 1-3 nm size began to develop within the amorphous zone according to their report. The difference with our case is that the sample was thin in our experiments which allows the He⁺ ions to efficiently escape from the both top and bottom surfaces since He⁺ has a high vacancy-enhanced diffusion in crystalline silicon[182]. Also in another study[183], with lower applied doses, with 30 keV energy He⁺ ion beam on bulk Si samples irradiated with $1.9\text{-}2.9 \times 10^8$ ion/cm², the crystal structure could not be effectively destroyed by He⁺ ions.

For the aluminium samples, it appeared that there was bulging on the rear side of the samples subjected to medium and high doses. However, we have some uncertainty regarding these findings because our CLSM analysis faced challenges in accurately depicting the morphological changes. This difficulty arose from the non-uniform sample preparation

and the fact that the sample area itself exhibits topography due to the milling process. Wilson et al[184], showed that He^+ traps in the bulk Al samples just like as bulk Si. Knowing that Al has metallic crystal structure which makes the vacancy diffusion easier than the one is Si, therefore the He^+ should exit the Al exit surface more easily than Si and do not create any morphological change on the backside. Girka et al.[185] showed that aluminium sputtered on a surface may be redeposited as cone-shaped particles. The redeposition specifically takes place on the slopes of cones, where target and impurity atoms were simultaneously degraded due to non-homogeneous erosion of a radiation-damaged surface.

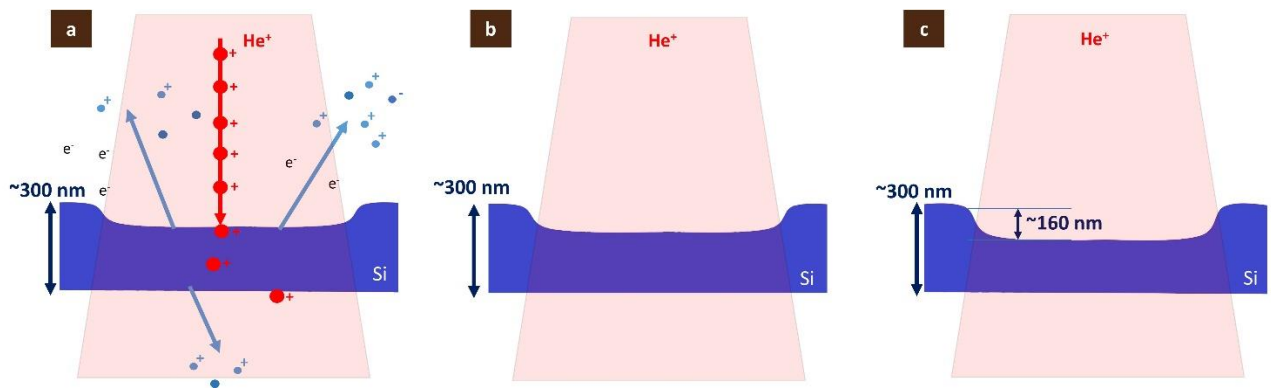


Figure 3.16: Schematic illustration of topographic evolutions observed after (a, d) low dose (b, e) medium dose (c, f) high dose He^+ ion irradiation on Si.

3.3 Conclusions

While gallium irradiation has been the subject of various studies on different samples, there is a gap in research when it comes to investigating the irradiated parts' backside. In summary, our primary focus in this study has been on examining physical deformations and phase change-induced plastic deformations occurring on the rear side of the samples. This emphasis aligns with our main research objective, which revolves around transmission ion imaging and its sensitivity to alterations in back surface texture.

After Ga^+ irradiation on the Silicon sample, we can denote the observation of the alteration on the back surface of the silicon samples. Given that the thickness of the silicon samples after each low, medium and high dose Ga^+ exposure (Table 3.1) varies and that it is substantially thinner. However, the cause is not the lower thickness but a predominant mechanism so-called hammering effect[186], which is evident from the bulging of both samples after exposure to medium and high doses. The observed bulging in high dose exposed sample on the back may be attributed partially to the energy deposited by gallium

ions when interacting with the sample's rear surface. In both medium and high doses of Ga^+ irradiated Si samples, the hammering effect was noticeable. However, the actual observable causes of deformation in Si exposed to a medium dose were the amorphous transformation and expansion changes. To further explain the surface blowing observation, we have a combination of phases because not all material has transitioned to the amorphous state. As a result, the amorphous layer leads to surface deformations by carrying the material above with it. This difference in volume caused by amorphization may result in stress and a compositional gradient that creates the curvature of the medium dosage sample. Whereas in high dose, one potential explanation is that the amorphized Silicon together with the implanted Ga^+ and atomic displacements would push the remaining layer backward. Finally, the curvature was not observed even with a thinner remaining layer (9nm) since all the Si is amorphous and the structure is homogeneous, and the stress has released. In addition, a threshold dose should exist between medium and high doses, where the morphology on the back would switch from blowing to bulging in Si at this threshold.

Regarding the experimental results, we should note that, despite our anticipation of observing a recession on the backside, the forward sputtering was unable to produce the recession. Neither for the medium dose case nor for the high dose. Our expectation was due to the presence of a crystalline structure and the minimal occurrence of forward sputtering in our simulations. It is crucial to note that the simulation did not consider the crystal effect associated with the channelling process, which further facilitates the ion travel within the material. Consequently, it is plausible that a greater degree of transmission occurs than what is predicted by the simulation. In addition, Due to the higher transmission of Ga^+ ion in experiments in compare with simulation, a reduction in the amount of material sputtered from the surface is possible in experiments. This, in turn, increases the observed hammering effect at higher Si doses.

In the Ga^+ irradiated Aluminium samples, a substantial change in the texture of the backend was not observed in experiments. To better understand, we compare the simulation results of Al with Si samples. Regarding to simulation results, Si has a lower sputter yield compared to Al, which yields in lower transmission of Ga^+ ions through Al. The higher Forward sputter yield (medium dose exposed sample) of Si compared with Al could be a reason for the different observations. Furthermore, the observed morphological differences between Al and Si align with their distinct atomic bonding nature and the difference in the displacement

capability of Al atoms compared to Si atoms during irradiation. In conclusion of simulation and experimental results, as the forward sputtering yield is generally low, the most prominent phenomena for Al is backward sputtering, implantation, and sputtering, and for the Si, is backward sputtering, implantation, and amorphization.

In the context of He^+ irradiation on Si, there was no observable alteration on the back side of the samples following exposure to He^+ . This suggests that utilizing a He^+ ion beam for imaging on this particular material will maintain the integrity of the backside topography and won't introduce any misleading artifacts using the mentioned ion dosage range. However, when it comes to the aluminium samples, the effects of He^+ irradiation remain uncertain, as the CLSM analysis couldn't definitively reveal the changes occurring on the backside. Also, the presence of a darker region on the irradiated area in the CLSM images of He^+ irradiated Si samples was attributed to surface deposition of hydrocarbons.

4 Chapter 4: He⁺ ion Channelling Contrast with STIM imaging

The present chapter aims to discuss the nanoscale contrasts induced by ion channeling in STIM images acquired through npSCOPE using He⁺ ions in keV energy. Our example study used a thin polycrystalline gold membrane with discrete crystalline defects. The goal is to localize and image the subsurface characteristics to learn more about the sample's crystalline nature, which will be covered in more detail with analytical correlation in the final chapter. Firstly, we will compare the contrasts in STIM and SE images. In addition, the lateral resolution of STIM images, measured experimentally, is compared to simulated beam-broadening obtained from Monte Carlo simulations. Subsequently, we report a quantitative exploration at the nanoscale, examining the transmission of He⁺ ions as well as neutrals through areas which contains crystalline defects and regions without crystalline defects. This is achieved through a correlative approach that employs STIM with electron diffraction on identical regions.

4.1 Sample preparation workflow and imaging parameters

The sample was a 50 nm thick freestanding Au membrane (UltrAuFoil®, Quantifoil Micro Tools GmbH) on a 300 mesh Au grid. Before the experiments, it was annealed for 2 hours at 700 °C to obtain large grains with isolated twin defects. For STIM and SE imaging, the npSCOPE prototype[89], [131] was used. 25 keV He⁺ primary ion beam passing through a 10 μm beam limiting aperture with spot control 5 setting and a helium pressure of 2.6×10^{-6} Torr were used for most of the STIM images. A beam current of about 0.05 pA was employed on the sample to decrease the ion beam damage to the STIM detector. The primary ion beam energy was 30 keV, and spot control 4 was used to record the SE and STIM pictures in Figure 4.1, resulting in a beam current of 0.5 pA and 0.1 pA on the sample for SE and STIM imaging, respectively. The aimed beam current was gained by tuning the He gas pressure, which was set at 2.6×10^{-6} Torr for SE imaging and 2.7×10^{-7} Torr for STIM imaging mode. The Everhart-Thornley (ET) detector in npSCOPE was used to record the SE images in a raster matrix of 1024 x 1024 pixels with a frame average of 8 and a dwell time of 20 μs per pixel. The STIM images were recorded in a single frame scan with a 512x512-pixel raster matrix and a dwell time of 110 μs per pixel. The sample-to-detector distance for the STIM images shown in this chapter was 256 mm. The distance corresponds to a scattering

angle ranging from 0 to 97 mrad for all azimuthal angles (extending to 137 mrad on the corners of the detectors). All the STIM images demonstrated in this article are from 4D datasets described comprehensively in chapter 1.

4.2 Results and Discussion

4.2.1 STIM and SE imaging mode comparison

First, we compared STIM and SE images from a sample of a thin freestanding perforated polycrystalline gold membrane (with ~ 50 nm thickness). This study was done to comprehend the STIM image contrast, which will aid us in understanding the channelling contrast. The STIM image in Figure 4.1(a) shows an excellent clear contrast in different grains, which is due to the different orientations in each grain since the sample contains different orientations in each grain. If we compare the STIM contrast from Figure 4.1(a) with the corresponding SE contrast in Figure 4.1(b), it is clear that the variations in the number of transmitted channelled ions from one grain to another result in evidently better contrast in STIM imaging. The STIM contrast manifests rich microstructural details, which are visible in SE images also, but only to some extent.

The apparent contrast is due to the channelling effect in transmission mode. What we should also consider is that the SE images are mapping a value from 0 to 255 value. However, the STIM images have a colour scale bar showing each pixel value's actual counts received on the detector. The straight dark lines which exist in some certain grains in STIM images (e.g., the green circle and the green rectangular in Figure 4.1(a, d) respectively) show the twin bands in the parent grains. The twin bands show up as dark lines due to the local change in crystal orientation in the twin band, which will result in different amounts of ion transmission. To explain further, when the twin band's contrast is dark, the local decrease in ion channelling in the grain in which they are embedded is the reason for that. Also, the twin band can have an orientation that is more favourable to channelling than the parent grain resulting from brighter lines in darker grains (e.g., the red circle in Figure 4.1(a). As mentioned in literature[83] the SE and STIM images are expected to have inverse contrast; the more SE are produced, the fewer ions are transmitted. This effect is apparent in both sets of ROIs. However, to understand better, in addition to STIM and SE in the last column, we showed the inverted SE contrast in Figure 4.1(c). The inverted SE image shows the

difference between the original pixel value and 255 (see Figure 4.1(c, f)). The contrast ranges for the images were adjusted differently. The minimum and maximum values for the contrast were set to 75 and 225, respectively. In contrast, for the SE images, the parameters were set to 30 and 180. In case any pixel values deviated beyond these ranges, they were displayed using the closest colour, either black or white, relying on whether they were lower or higher than the specified range.

One point that should be considered is the dark semi-circular features that are visible in STIM and SE images, corresponding to the periodic perforations in the gold film. In the SE image, these perforations appear as dark discs (e.g., the yellow arrow in Figure 4.1(b)), and according to the inverse SE contrast image, which appears as bright discs, the discs should appear as bright discs. In contrast, the perforations appear as dark discs in STIM due to the oversaturation in the DLD detector. The oversaturation occurs since the entire probe current passes through these holes. When the primary ion beam passes through the holes, even in a small area, they collide with the MCP detector locally. After the collision, insufficient time for MCP to be recharged results in an intense reduction of the pulse height distribution to a level below the noise threshold. However, as we explained in a few lines above, STIM images consist of detailed contrasts. Another example is the comparison of the grains which are brightest in STIM but darkest in SE mode (see the blue rectangle in Figure 4.1 (d, e, and f)).

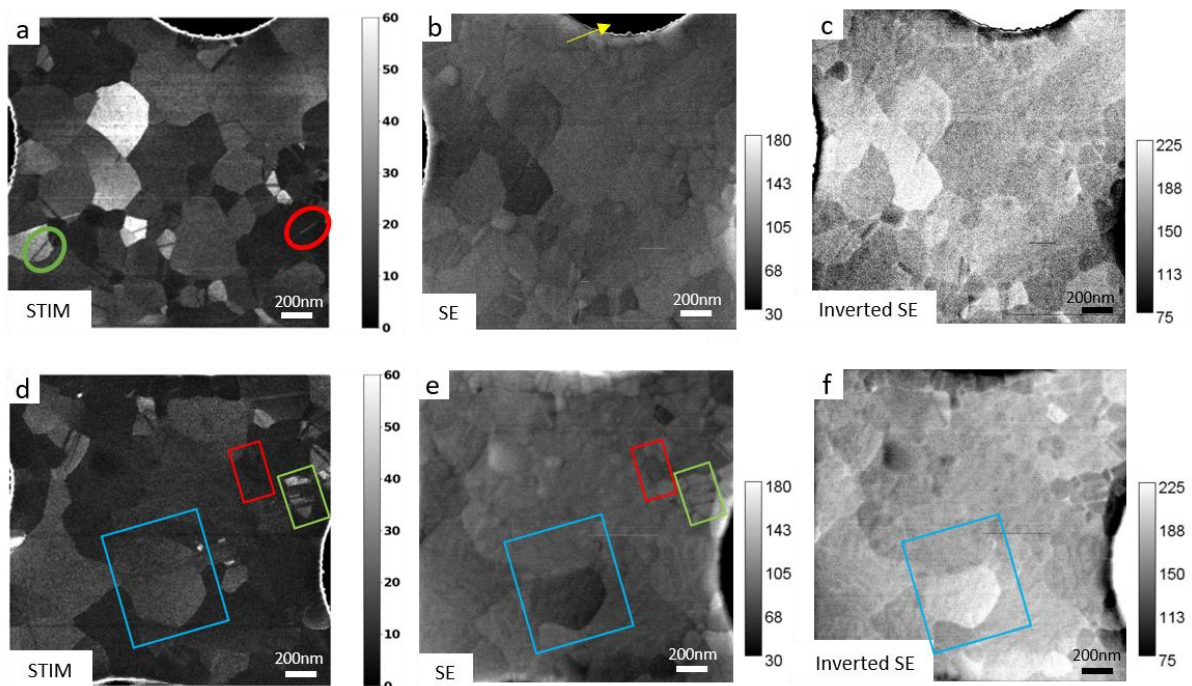


Figure 4.1: STIM (a, d), corresponding SE (b, e) and SE with inverted contrast (c, f) image pairs of thin freestanding polycrystalline Au sample (thickness ~ 50 nm). Twin bands are shown by the straight dark lines that is observed within some grains in the STIM images. Dark twin bands in a bright grain (green circle in figure (a)) and bright twin bands in a dark grain (red circle in figure (a)) are observed. Figures (c, f) demonstrate the inverse contrast between SE and STIM pictures by inverting the SE contrast of the same ROI. A blue rectangle in (d, e) indicates the same grain observed in STIM and SE. The SE mode can also be used to observe the rich features of the microstructure seen in the STIM mode. Some grains seem dark in both SE and STIM images, as seen by the red and green rectangles in (figures (d, e)), whereas some grains look bright in both SE and STIM images.

In addition to the black discs observed with the same dark contrast in SE and STIM, we observed grains that appear dark or bright in both SE and STIM. The dark grains (e.g., the red rectangle in Figure 4.2 (d, e)) could be explained by two stacked grains with two different orientations. Let us consider the top grain with a favourable orientation for channelling, which will produce a poor SE yield, and dark contrast will appear for the SE image. However, for this grain, more transmitted ions were expected. Conversely, suppose another grain is in an unfavourable orientation for channelling. In that case, it will also yield low transmission with a higher scatter of the He^+ ions. However, it is unexpected and requires more research to explain when a grain is bright in both the SE and STIM images (such as the green rectangle in Figure 4.1 (d, e)). This behaviour should be investigated within the specified scattering angles (measured from the bright central spot on the detector). As mentioned in Chapter 1, STIM images can be reproduced by choosing on-axis, off-axis, or an annular ring by selecting the particular polar or azimuthal scattering angles on the detector image. The angular selection aims to visualize the various features in the image, which may show different scattering intensities due to the different crystal orientations or chemical compositions. Therefore, images with specific scattering angles offer an additional contrast mechanism that can be used in STIM images for further investigations. Figure 4.2 shows one example of the mentioned concept. Figure 4.2(d) displays the detector image, and Figure 4.2 (a-c) show the images of a region produced simply utilizing intensities measured from the bright central spot on the detector till the specified scattering angle. The colour bar represents the integer number of counts from each pixel, and the yellow colour in the scale bar indicates the extent of counts in each pixel that are at or above the maximum scale bar. The grain's shape visibility and the overall distribution of pixel values are the parameters used to select the colour ranges.

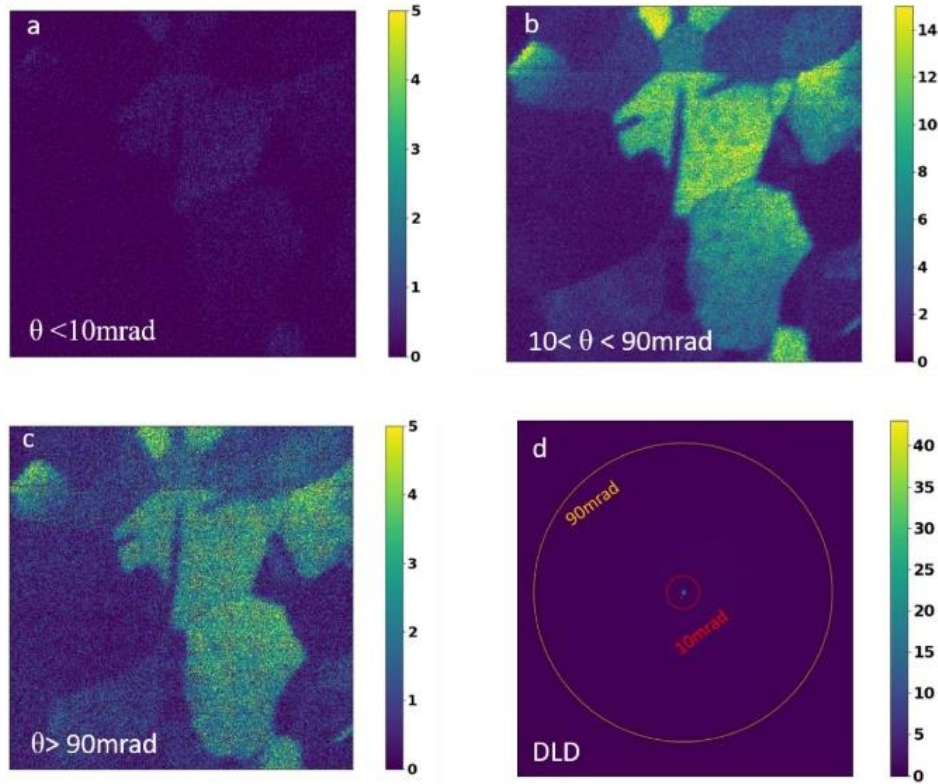


Figure 4.2: (a-c) STIM images obtained using integrated intensities within the specific scattering angles. (d) The circles in this DLD detector image represent the scattering radii utilized to create the STIM images. Image contrast exhibited by sample areas that scatter intensities at different angles. The field of view is $1.1\text{ }\mu\text{m}$ for a-c.

4.2.2 STIM, TKD and high-resolution BSE imaging mode comparison

Figure 4.3 displays three different imaging modes from the same areas: STIM, TKD, and BSE. We can better interpret the STIM images using TKD imaging, which offers more detailed crystallographic information. The method we employed in TKD imaging is the established and widely accepted method. TKD data illustration is a combination of Inverse pole figure (IPF) in the colour channel and image quality (IQ) as a grey value. Also, high-resolution BSE pictures were taken from the same ROIs for comparison. Comparing the three modes of images from the same ROI reveals distinct contrast variances from each other. In the first row Figure 4.3 (a-c), the contrast between the right and left sides of the red box is clearly different in STIM and TKD but not in BSE mode. The failure to detect the second grain (inside red box) in the BSE mode results from the incapacity to capture the change in crystal orientation, consequently preventing from manifesting as a contrast change. BSE imaging only shows output signals from the upper surface of the sample. Considering the BSE output signal is predicted to be approximately 21.5 nm deep from the top surface in our case because the electron beam energy utilized in the Au sample was 5 keV[187]. On the other

hand, the ions that reached the STIM detector have transmitted the entire thickness, which means the STIM displays the information from whole thickness of the sample. Also, the simulations showed that for 50nm gold sample, the TKD and BSE cannot provide any information for a central region on the sample. Hence STIM image fills this information gap as it probes the thickness throughout. Moreover, the reason for not observing the orientation change in BSE might be that the change in orientation is below the critical escape depth range of backscattered electrons. Another explanation, though, is that there could be two alternative grain orientations that, by accident, have similar backscatter yields. A high angular resolution imaging with multiple tilt angles, such as TEM can elucidate this.

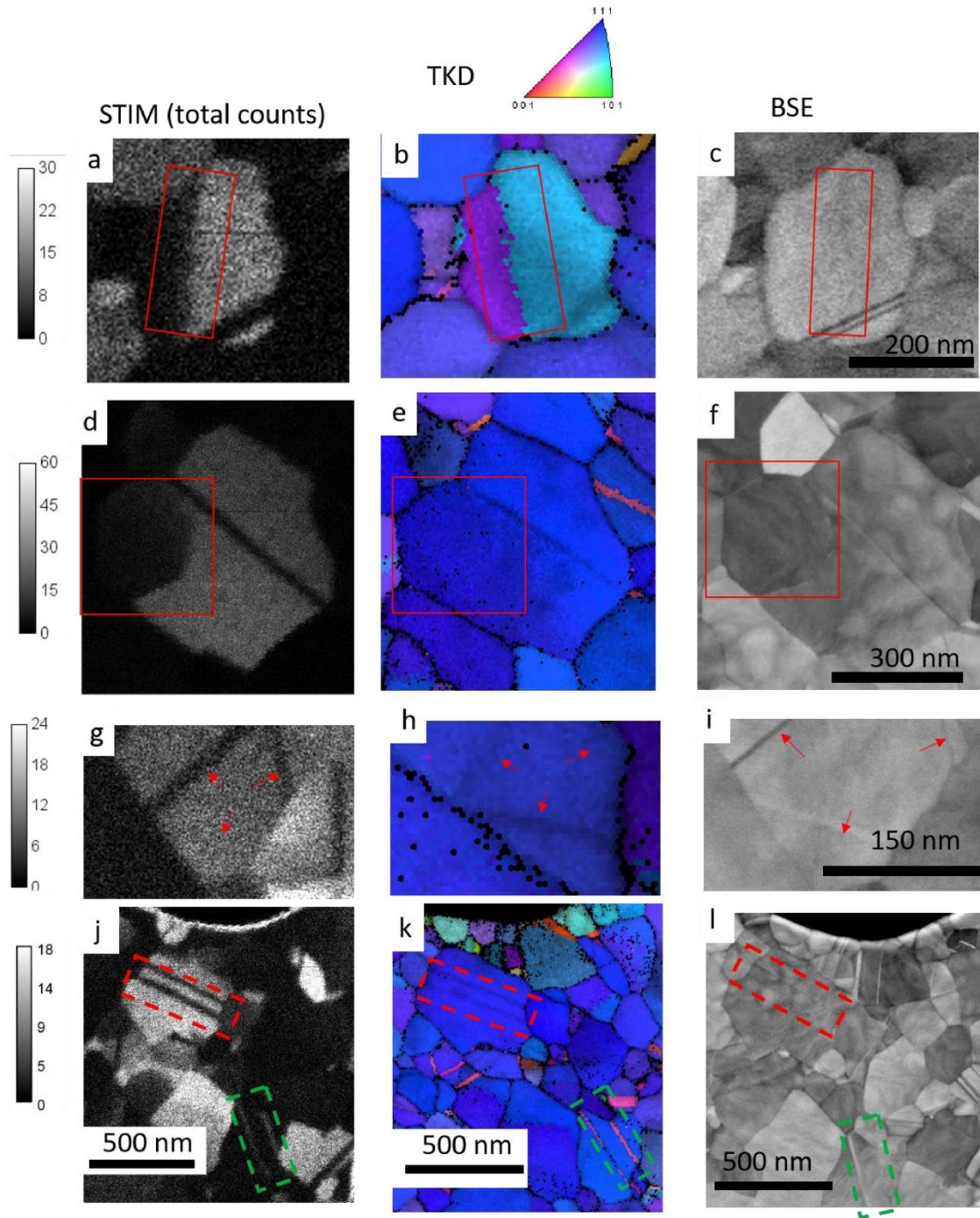


Figure 4.3: Comparison of STIM, TKD and BSE imaging modes. The same ROI is presented in each row. Coloured rectangles, arrows, and boxes denote features with variations in contrast or visibility depending on the imaging mode. The STIM image's intensity ranges are provided next to the relevant images. All the BSE images have a grey scale with values ranging from 0 (black) to 255 (white).

Furthermore, in Figure 4.3 (c) the two thin parallel lines inside the red rectangular are visible in the central grain in BSE identified as a twin band. The lines track the $[110]$ direction due to the film's overall $\{111\}$ fibre texture, which twin bands are commonly bound by. The twin bands in BSE are also visible but as a broad continuous line in STIM image. Comparing the

TKD image, the Kikuchi pattern overlap has reduced the image's quality, yet like with the STIM, the two lines are not discernible independently, and the bands have no discernible orientation contrast. Figure 4.3 (d) shows a polygonal feature visible in the STIM and BSE images. In the TKD image, the same feature is not evident (note the red box). Likewise, the same area in the TKD depicted in Figure 4.3(e) does not entirely match the shape of the brightest grain in Figure 4.3 (f). Also, the upper left edge of the TKD is a collection of unclear orientations as opposed to the BSE's distinct line. In this context, simulations[188] demonstrated that 80% of the final scattering events for 30 keV electrons in gold take place within an estimated 4 nm of the bottom surface. The 4 nm from the bottom surface can be considered as the information depth in the TKD images in Figure 4.3. This consideration is based on the TKD operation mechanisms that is mentioned above. According to this mechanism, the output signals of earlier scattering that emerged from the sample's top surface may be lost as a result of later processes of elastic and inelastic scattering. As a result, the top surface features could be invisible such as the polygonal grain in Figure 4.3(e). In contrast, the BSE output signal reveals the outcome from the upper surface, in which the polygon is visible. Also, the presence of the variable orientations in different depths are the cause of the change in the form of the brightest grain in the BSE image in Figure 4.3(f) and the corresponding TKD image.

A grain with three twin bands is visible in the third row of Figure 4.3 (g- i), forming a roughly 60-degree angle to one another (the red arrows indicate this grain). These are pointed in one of the three directions of the $[110]$ and sets of $\{111\}$ planes that bind the twin bands together. Interestingly, these twin band sets appear differently depending on the imaging technique or do not show up at all. Additionally, the STIM twin band, which will be further explored in Figure 4.4, is evident, whereas the twin band in TKD and BSE is the least apparent. In the last row Figure 4.3 (j-l), the inverse contrast of the twin bands in two different grains has been highlighted. In the grain marked by the dashed red rectangles, the twin bands appear as a dark line in a bright grain. However, the twin band in the dashed green line is the opposite. The two twin bands within the red rectangles are discernible in all three imaging modes, although the contrast for the twins is somewhat faint in the BSE picture. Alternatively, within the green rectangles, only one of the twin bands is noticeable in the BSE image, while it is visible in both TKD and STIM. The invisibility of the second twin

band could be due to the same backscatter yield of the parent grain and the twin band. Another reason could be the twin band's presence only in the sample's backside. From the second explanation for the twin's invisibility in BSE, we may infer that the ions can be redirected into a bottom crystal's channelling direction after initially passing through non-channelling orientations.

Furthermore, for all rows of the images, the low-voltage BSE has the highest resolution compared to the other two imaging modes. One illustration is the two detectable twin bands in Figure 4.3(c) compared to the equivalent STIM and TKD, in which the two lines are unrecognizable. Figure 4.4 (a–c) displays the set of images captured in STIM, TKD, and BSE modes from the same ROI to explore this further. For this aim line profiles done for the STIM (Figure 4.4 (a)) and the BSE images Figure 4.4 (c) to reveal the measured feature sizes using transmitted ion and backscattered electron intensities. The distribution of transmission channelling efficiencies throughout the ROI is depicted quantitatively in a histogram in Figure 4.4 (d).

4.2.3 STIM imaging resolution assessment

We performed SRIM and CASINO simulations to assess the reduced resolution caused by the beam broadening in STIM and TKD modes. Figure 4.4 (f) depicts the beam radius for ion and electron beams at the exit surface of the sample. The broadening of the ion or electron beam in STIM and TKD methods, respectively, could partially account for the fluctuations in image resolution. A beam at the nanometre scale will expand to tens of nanometres in both instances. The SRIM measurements demonstrate that while transmitting through 50 nm amorphous Au, a helium beam with an energy of 25 keV expands from a point to a full width at half maximum (FWHM) of 26 nm. Likewise, CASINO software shows that a 30 keV electron beam with a 2.6 nm FWHM (the software's "probe size" setting was 4.7 nm) spreads to an 8.3 nm FWHM when transmitted through 50 nm Au. These spreads impact the final resolution for both electron and ion beams. Notice that to determine the FWHM values, the radial histogram of the simulated trajectories of integrated count densities was used. In addition to the beam spread, the systematic nature of STIM's operation would cause the signal to noise ratio to drop, lowering image clarity. Furthermore, the twin bands' inherent characteristics should also be considered; looking at a twin band from above (normal to the plane), they would appear with a broader space than their actual width. The

broader space emerges even if an ideal probe was employed since they have an angle to the surface plane. In Figure 4.4(c), two twin bands with a gap distance of 15 nm and an order of 15 nm width are discernible in the BSE image. We may determine that these twin bands were visible but were too close together to be resolved separately by STIM method. To support this observation, we measured a distinct single feature in BSE and STIM in Figure 4.4 (e). The FWHM of 30 nm for the intensity dip in the STIM image and roughly 15 nm in BSE were achieved, which is consistent with the measurement from Figure 4.4 (c). The measurements from Figure 4.4(c) indicate that the two 15 nm features, positioned approximately 15 nm apart from each other, merged into a single blurred entity in the STIM image. In conclusion, the lowest resolvable twin band separation for the mentioned STIM experimental setup would be roughly 30 nm, which overestimates the best resolution caused by the twin bands' tilt concerning the parent plane. The method might resolve a thinner band if the twin band was oriented parallel to the beam direction. Also, to study the number of counts along the twin band to the parent grain, where the intensity decreases due to the change in orientation, an orange box has been added to Figure 4.4 (a). The decline in counts per pixel from 14 to 5 indicates that the ratio of transmission efficiency for ions in channelling and non-channelling states is 2.8 for the complete detector's collection angles and for this particular set of orientations.

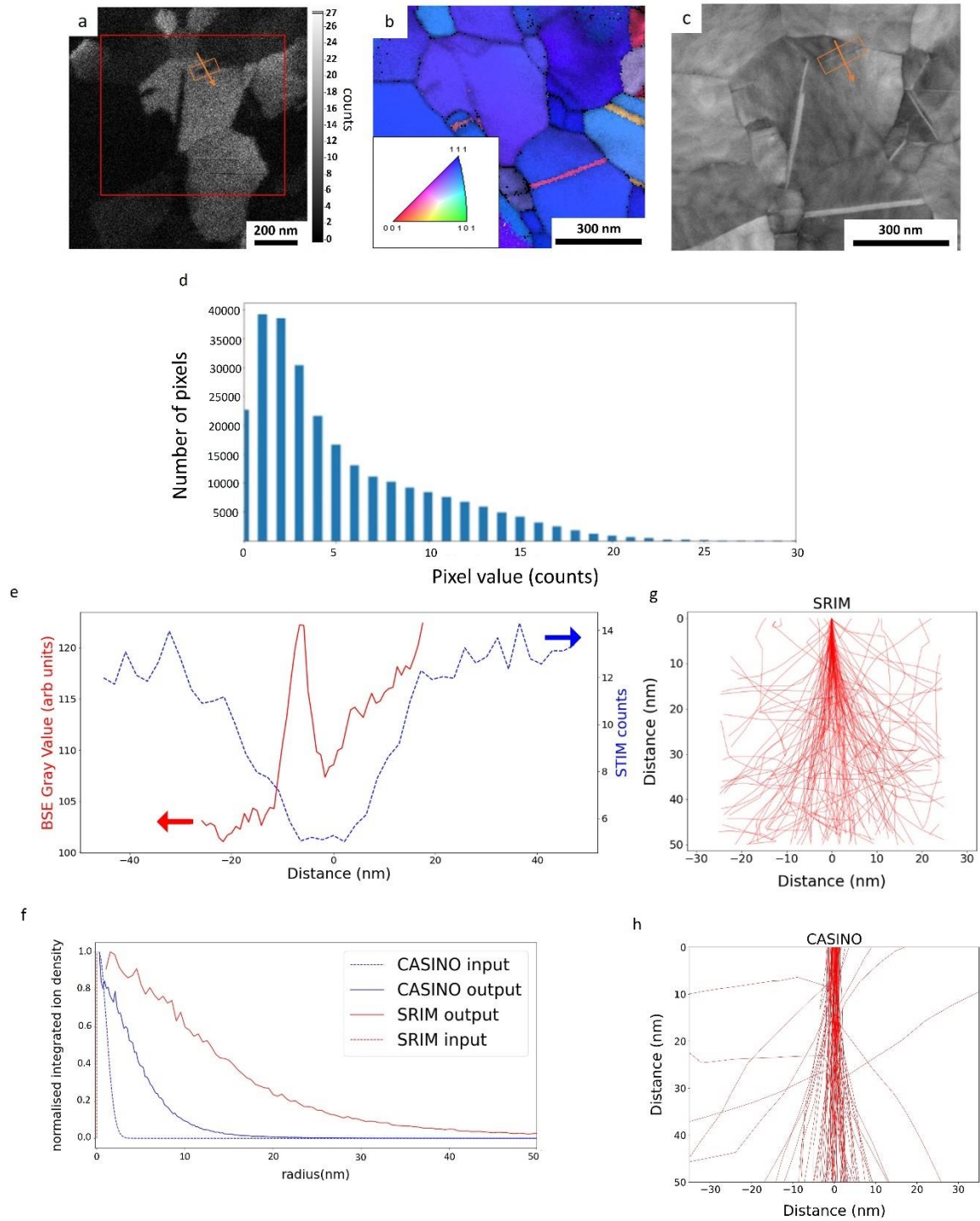


Figure 4.4: STIM (a), TKD (b), and in BSE (c) modes from the same ROI. The colour mapping for the various orientations is displayed in the inset in b. In (d), a histogram shows the (a) STIM image's intensity. Since in the STIM images, intensities are absolute counts, it is possible to quantitatively examine the channelling efficiency in various areas of the image. The image in (e) compares the measured feature size for the same twin band in BSE and STIM. The ion and electron beam sizes at the sample's exit surface are displayed in (f) alongside snapshots of ion and electron trajectories from SRIM and CASINO simulations, respectively. Also, note that the STIM image lacks the bright twin band that can be seen in the bottom right of the BSE and TKD images.

4.2.4 STIM imaging contrast variation with magnification

In this section we will talk about how STIM imaging's image contrast in our setup is affected by several variables. The effect of critical angle on channelling was discussed in chapter 1. An instance that can help us understand how the beam incidence angle can alter the transmitted intensity and, consequently, affect the contrast in transmission imaging can be located in the research conducted by Andreen et al. In this study the full width half maximum for the transmitted intensity of 18 keV He⁺ ions in single crystal Au foils has been measured in previous investigations[57] as 6.04°, 5.81°, and 4.63° for the channels of the crystallographic orientations [011], [001], and [112], respectively.

In the case of the sample examined in our study, the thickness is uniform, meaning that channelling effects are the primary cause of variations in transmission. Therefore, the crystallographic orientation of the grains and defects within the Au film will largely determine the intensity of the final STIM image. The channelling efficiencies of different orientations demonstrate that channelling is most effective along low index directions, although it still occurs to a lesser degree for other orientations. This finding is consistent with computational simulations [86], [189]. It also explains why some twins may not be visible in STIM images, as their orientation may coincide with a different channelling direction from that of the parent grain, leading to poor or no contrast. Complete blocking of transmission or channelling away from the detector area is infrequent, as evident from the histogram in Figure 4.4 (d), where only a small fraction of the total 2.6×10^5 pixels in the STIM, image has zero intensity on the detector.

The study found that channelling is not only influenced by the grain orientations in the sample, but also by the imaging settings used. The imaging setting effect demonstrated by the STIM images in Figure 4.5. Certain grains appeared brighter in the larger FOV (Figure 4.5 (a, b)) and some became brighter in the smaller FOV (Figure 4.5 (c)). Note that the sample was not moved intentionally. Although for the rest of the grains, the opposite effect was observed. The higher ion dose in the smaller FOV can explain the higher counts seen in Figure 4.5(c) than in Figure 4.5 (a, b) but it cannot account for the contrast reversion. Moreover, the local incidence angle in Figure 4.5 (b, c) would be the same because the sample was not shifted, and the detected contrast variations were unexpected. It is suspected that the sample experienced a slight drift or a small difference in the primary

beam incidence angle while changing the FOV settings. Both reasons can affect channelling contrast. Refer to Figure 4.6 for an illustration that explains why some twins appear dark in a bright grain while others appear bright in a dark grain in the STIM images. The mechanism illustrated in Figure 4.6 proposes that the visibility of twins in STIM images depends on twin boundaries alignment concerning the primary beam incidence angle. Twins with large areas of their boundaries exposed to the primary beam will be easily visible. In contrast, twins and their parent grains aligned in two different channelling axes will have very little or no channelling contrast, rendering them invisible in the parent grain in STIM image. Increasing the convergence angle of the beam enlarges the range of incidence angles between the ion and the channel, and it reduces contrast as well as peak brightness in the image. Therefore, the convergence angle of the beam is an influencing factor on channelling contrast.

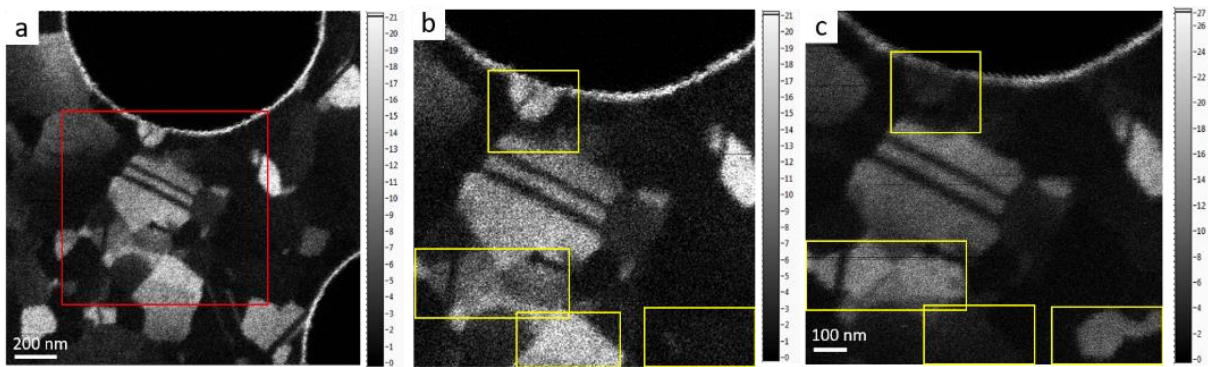


Figure 4.5: Changing the FOV settings caused certain grains' contrast to observe. (a) and (c) are as-acquired images at two different FOVs. (b) has been cropped and enlarged to facilitate comparison with (c) while the FOV remains the same as (a). Some specific grains (e.g., bottom right), which are invisible in a larger FOV (a, b), appear clearly when a smaller FOV (c) is chosen. Regarding some other grains, the reverse impact is seen (e.g., top centre). This shows that the channelling contrast is sensitive to even minute changes in the imaging conditions.

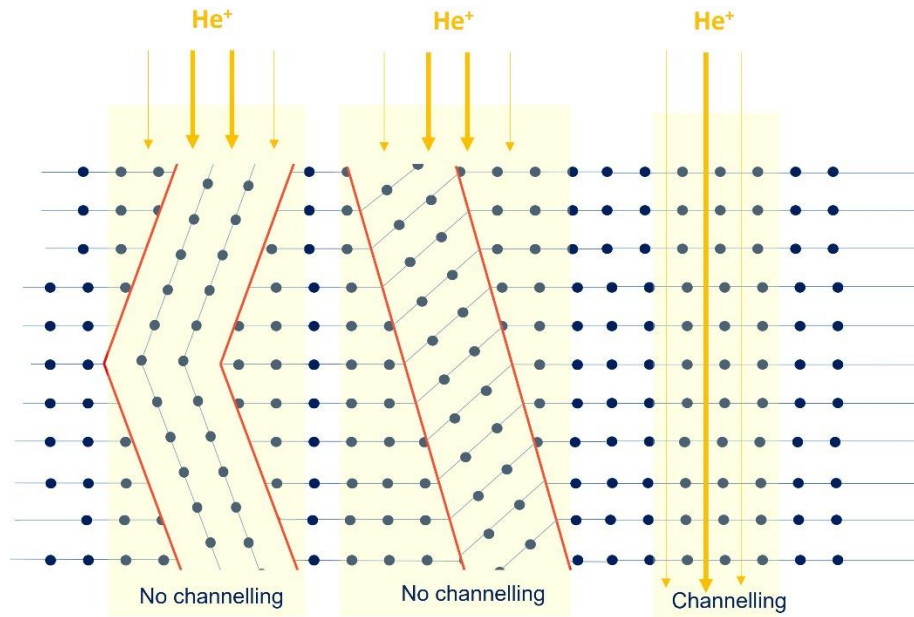


Figure 4.6: Schematic cross-sectional showing a few consistent twin variations in the sample. The red lines show the twin boundaries. When the primary beam's incidence angle is aligned with a low-index axis, channelling is encouraged, and the grain appears bright while the twins are dark in the STIM image (cf. Figure 4.1 (a)). A twin and its parent grain may be rendered invisible in the STIM image if, by chance, they coincide with two separate channelling axes. (cf. Figure 4.3 (g, i) and Figure 4.4 (a, c)).

4.3 Conclusions

STIM was used to qualitatively analyse the contrast across nanoscale twins in a thin gold membrane. STIM, TKD and BSE images were obtained from the same areas to understand the image contrast and correlated altogether. The STIM lateral resolution of better than 30 nm was determined under the experimental conditions compared with the BSE images with a beam normal to sample. The observed results were compared with Monte Carlo simulations to gain insights into beam broadening and its effect on STIM image resolution. Dark twins were visible in bright grains, while bright twins were visible in dark grains, but some twins remained undetectable in STIM. Under the experimental conditions mentioned before, the ion transmission efficiency decreased by a factor of 2.8 across a specific twin band. The contrast in some grains was reversed, indicating that even minor variations in illumination conditions can affect channelling contrast sensitivity. To comprehend the contrast mechanisms involved in twin imaging, a crystallographic analysis of the orientation of different twin variants was performed. Furthermore, we concluded that if a twin and a parent grain are aligned with two distinct but channelling axes, the twin may not be visible

in STIM. Compared to conventional ion-induced SE imaging in HIM, STIM imaging reveals more detailed contrast. Moreover, the use of very low primary current (50 fA) in STIM, as opposed to typical SE imaging in HIM (few pA), suggests that STIM imaging is a promising approach for nanoscale imaging that provides additional contrast mechanisms while potentially reducing beam-induced sample damage compared to standard SE imaging in HIM. This study demonstrates, for the first time, the potential to quantitatively investigate ion channelling within nanoscale structures such as isolated crystalline defects, opening the door for more advanced experiments, such as analysing ion energy loss characteristics with nanometre-scale lateral resolution.

To gain a better comprehension of the mechanisms of ion-solid interactions with nanometer-scale spatial resolution, it is essential to have a comprehensive understanding of all the factors that impact channelling contrast. This is particularly crucial for advanced experiments, where ion energy losses while traversing individual crystalline defects such as twins or stacking faults can be correlated.

5 Chapter 5: Energy loss contrast in STIM imaging mode

In this chapter we employed transmitted helium ion signals for microscopy in a similar field to what we investigated with STIM in chapter 4, but the beam, rastering modes, and setup differ. However, we used a focused beam and scanning transmission mode comparable to STIM[143], [148]–[150]. The chapter 5's primary objective is to demonstrate the STIM-IELS technique's ability to measure energy loss differences with 5D datasets.

Secondly, we will show the data from ToF STIM-IELS experiment using 20keV He⁺ ions, which starts to fill this gap in the current literature. The results of this experiment showcase the potential of KeV helium ions to be utilized effectively in energy loss imaging experiments, thus laying the foundation for the development of KeV scanning transmission ion microscopy energy loss techniques. The experiments involved using a stationary beam to obtain a single energy spectrum of the sample to measure the individual stopping power value. To achieve this, the incident or exit angle was adjusted to obtain angle-resolved measurements. It is important to note that sample imaging was not a focus in these experiments[49].

5.1 Sample preparation workflow

MEIS experiments were performed using Ga doped silicon samples. Galileo experiments done with Si partially coated with Au. Ga doped Si was prepared in Scios. The process involved implanting gallium ions at 30 keV using Ga-FIB, followed by vacuum annealing at 700 °C. The annealing step reformed silicon's crystalline structure and enabled gallium diffusion throughout the membrane.

To understand the projected range of Ga in Si, we performed simulations using SRIM. The simulation results showed that gallium implanted at 30 keV would have a projected range of 28 nm within silicon. However, these simulations did not consider the orientation of the silicon samples, which were single crystals with the (100) axis approximately aligned with the beam direction. This alignment with a channelling orientation is expected to increase the effective range of gallium diffusion. In order to enhance the probability of observing significant effects in the results related to channelling and energy loss, the goal was to introduce approximately 1% gallium into the silicon matrix. Nonetheless, considering the

implantation dimensions, achieving a 1% concentration of gallium across the entire 200 nm layer (referred to as the 'total' sample) would need a dose of around 8% at the average implantation depth. However, an alternate concentration was selected due to the limited solubility of gallium in silicon. In this case, the focus was on attaining a peak concentration of only 1% at the average implantation depth (referred to as the 'peak' sample). The total and peak samples were used in transmission analysis in ToF medium energy ion scattering (ToF-MEIS) instrument, which will be discussed later. The beam was expanded to an approximate spot size of 80 μm (measured using the standard 80-20 method at the Faraday cup edge) to prevent undesirable implantation. The beam spread would also help avoid potential membrane damage. Also, we determined the implantation dose using a faraday cup to measure the beam current. With the knowledge that the implantation area was assessed at the most minimal magnification achievable. Another approach for determining the implanted area is using the SE contrast alterations in the SE image. Following implantation, a vacuum annealing process was conducted at 700 °C for 1 minute. This annealing involved a linear ramp-up and down for 30 minutes to prevent membrane damage due to uneven thermal expansion.

Another sample used for the ToF measurements in Galileo was a sample comprising of two rectangular windows of 100 μm x 1500 μm and 15 nm thickness made of silicon membrane (NTUS100A15L from plano-em.de). Figure 5.1 illustrates the optical and secondary electron images of this sample. The first row displays images captured from the front side, while the second row presents images acquired from the reverse side after flipping the sample. In addition, the Leica EM ACE600 sputter coater was used to deposit Au on half of the windows, which appears as darker blue lower sections of the rectangular windows on the 'front' optical image and upper gold window sections on the 'back' optical image. As shown in Figure 5.1, the Si membranes broke partially during handling, resulting in three distinct but useful regions for our experiments on the sample: i) regions with a hole, ii) regions with only 15nm Si, and iii) regions with Au on top of 15nm Si (the 'Si/Au' region). The dissimilarities in the broken parts become evident upon comparing the images from the front and back sides. The deposited Au layer's thickness was determined using stylus profilometry, which provided a range of values between 24nm and 46nm, with an average of 32.5nm. The primary objective of analysing these samples is to assess differences in

energy loss within a 5D dataset rather than obtaining exact measurements of stopping powers. Therefore, the precise thickness of the film is not of utmost importance, as fluctuations in the average thickness will not impact the main findings we are aiming to achieve.

I acknowledge Dustin Andersen (from LIST) for Ga implanted Si sample preparations, and the Uppsala University team, namely Eleni Ntemou, Radek Holenak, and Daniel Primetzhofer for ToF-MEIS experiments. Also, I acknowledge Micheal Mousley for Galileo experiments and sample preparations. My primary involvement in these subjects centred around performing data analysis and investigations.

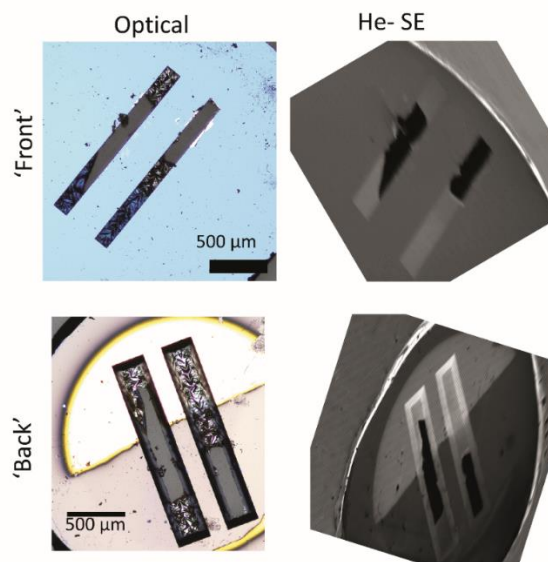


Figure 5.1: Optical images (left column) and helium generated secondary electron (SE) images (right column) of the sample. Since the SE detector of the prototype is positioned at an angle to the sample, the SE images exhibit a projection effect in comparison to the optical images. Notably, the front side of the silicon windows measures $100\text{ }\mu\text{m} \times 1500\text{ }\mu\text{m}$, with the scale bars being applicable only to the optical images.

5.2 Results and Discussion

In the chapter 4, we explored imaging contrasts within STIM images. We conducted a comparative analysis of transmission imaging in relation to alternative techniques. Now, our focus shifts towards investigating how energy variations correlate with angle changes. Our intention is to graph, analyse, and subsequently explain the experimental data using simulations, and highlight how this energy loss yields a distinct, novel imaging contrast.

Moreover, it's worth noting that energy loss can also contribute to contrast enhancement through careful data selection. Although ToF was employed in our study, we are excited about exploring additional avenues for achieving contrast. This implies that a deeper exploration beyond 2D spectra can uncover potential contrast-enhancing elements. In this context, we will begin by discussing the outcomes of ToF-MEIS on the Ga implanted Silicon. Subsequently, in the following section, we will delve into the results obtained using Galileo, this time on the gold-coated Si sample.

5.2.1 ToF-MEIS results on Ga implanted Si

Figure 5.2 (a) illustrates the dissimilarity in TOF spectra among three samples using 50 keV He⁺ ions: pristine, peak, and total samples. Evident differences are present among these three samples; nevertheless, discerning whether these distinctions arise from Ga within the channels or from incidental scatterings within the sample—possibly originating from Si lattice damage—remains uncertain. As our objective is to determine whether we can differentiate the positions of the Ga atoms within the lattice.

Concurrently, the TOF spectra are also influenced by the ion scattering angle. In Figure 5.2 (a), the plot is constructed considering a 2mm radius on the detector, revealing minimal discrepancies among the three samples. However, extending the plot to encompass all scattering angles Figure 5.2 (b) exhibits a longer flight time for the total sample, accompanied by a quantitatively distinct TOF spectrum.

In Figure 5.2 , Ga recoils and the transmitted projectile appears to overlap into a single peak. The reduction in mass separation, coupled with an increasing overlap between the Ga peak and the ascending projectile peak, complicates the discernment of an independent Ga peak. Note that particles identified within the channelling geometry typically exhibit shorter flight durations compared to those detected randomly[190]. Consequently, the initial part of the ToF peak represents the faster part, indicative of the channelled ions, while the latter half corresponds a mixture of slower ions and those that have undergone scattering. The second half is evidenced by a discernible shoulder in the Figure 5.2 (b).

Note that, the shoulder present in the total sample in Figure 5.2 (b) can be characterized through a comparison with the pristine sample to determine whether it arises from random channelling or implantation effects. Achieving this involves employing a beam alignment

procedure prior to experimentation to confirm precise beam alignment and exclude any influence of random channelling on the observed tail.

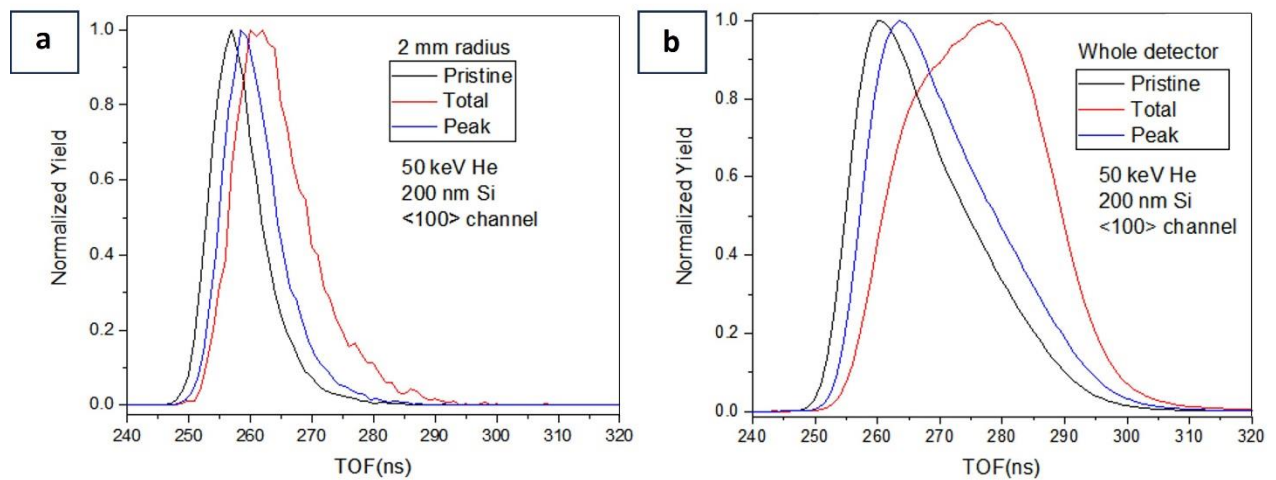


Figure 5.2: TOF spectra for the three Silson samples with normalized counts. Note the significant difference in the shape and timing of the TOF peak for the 'total' gallium implanted sample for the 'whole detector'.

Figure 5.3 depicts the channelling patterns derived from the Total sample. A star-like pattern is noticeable in the left image in Figure 5.3. Additionally, the dimensions of this star pattern within the channelling configuration allow us to assess, the scattering behaviour, energy loss, and peak broadening. Notably, a significant distinction in channelling pattern quality emerged based on whether the ion beam transmitted the Total Ga sample from its front or back side. Remarkably, the channelling effect's integrity diminished as ions entered the unimplanted membrane side and exited through the implanted side. This asymmetry in channelling suggests the presence of defects or contamination localized to one membrane side, or it hints at a lack of homogeneity in composition and crystal structure across the membrane's thickness. Changes in channelling pattern, respecting the high defect concentration side, confirms our previous discovery. Regarding to our findings in the previous chapter[143], ions were observed to channel through defects upon encountering them. However, upon reaching the defect on the exit side, the ions experienced scattering. Note that, the role of contamination appears unlikely, considering that the 'peak' sample underwent identical processing steps without manifesting this phenomenon.

Figure 5.4 show channelling patterns analysed on the Total sample, utilizing a Ne^+ beam at energies of 280 keV. Their distinctive energy loss characteristics initiated the idea of switching to Ne^+ ions, causing the contrasts between channelling and non-channelling

directions more visible than He^+ ions. As energy is higher than He, the distinct star shape becomes less visible and transitions toward resembling a donut shape, which is observable in the left image in Figure 5.4 attributed to diminished scattering. Notably, the time resolution remains relatively consistent across the different energies.

The difference between the front and back sides channelling patterns is maintained for both 50 keV He^+ and 280 keV Ne^+ ions (where the differences in mass and energy almost offset, resulting in a comparable particle velocity around $\sim 1.6 \times 10^6$ m/s). There exists a slight dissimilarity in the channelling behaviours of He^+ and Ne^+ . Specifically, the Ne^+ channelling patterns exhibit a clearer, less spread channelling pattern. This distinction could likely be attributed to the higher mass of the Ne^+ ion, which increases the probability of it readjusting its path through re-channelling when deviated.

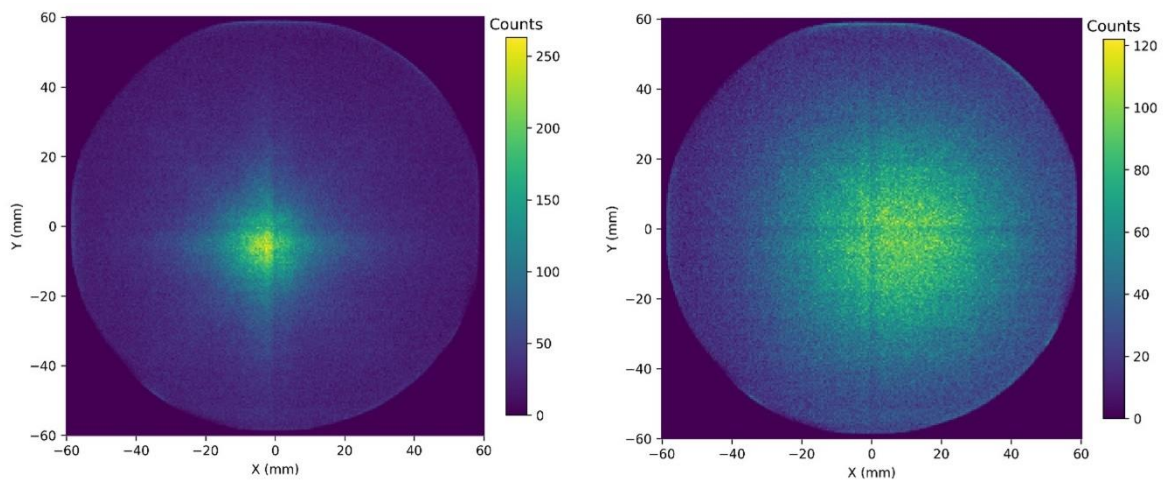


Figure 5.3: Images showing the $\langle 100 \rangle$ channelling pattern from the 'total' Ga implanted sample for incident He^+ ions at 50 keV from both the front (left) and back (right) of the sample. Image on the left shows star-like pattern.

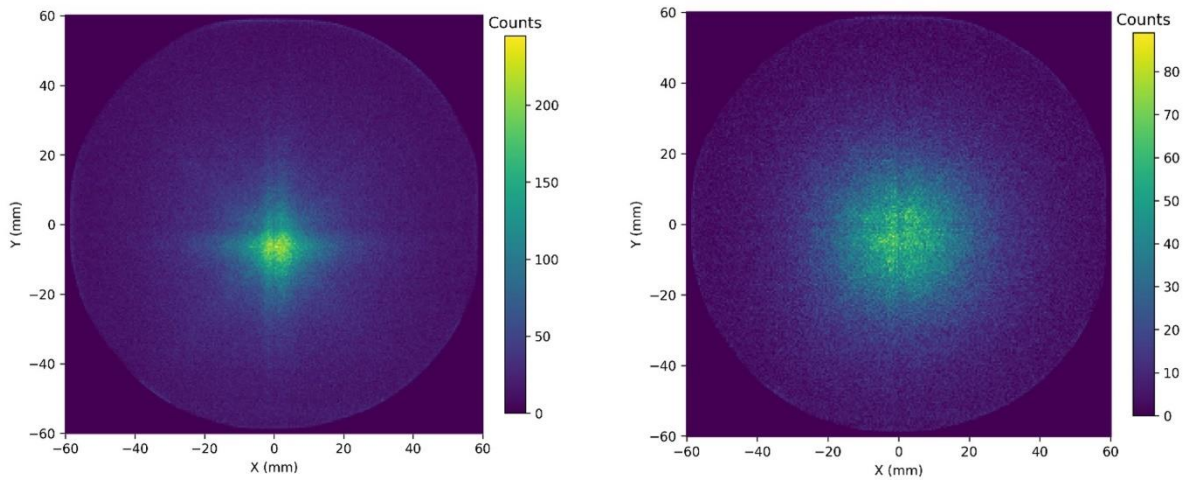


Figure 5.4: Images showing the $\langle 100 \rangle$ channelling pattern from the 'total' Ga implanted sample for incident Ne^+ ions at 280 keV from both the front (left) and back (right) of the sample.

To locate the position of Gallium within the structure, we pursued backscattering experiments. In these experiments, the energy of the He^+ ions that were backscattered could be correlated with the depth and mass of elements within the sample. Our initial effort, however, encountered difficulties due to the background counts originating from scattered projectiles and recoils within the chamber in the channelling configuration. Consequently, we placed the samples in front of a carbon wafer to minimize background counts. Additionally, we applied carbon tape to the surrounding area of the sample. This step served two purposes: facilitating sample identification and ensuring its proper alignment with the beam. This arrangement also diminished the backscattered signal from the surroundings, given that the beam spot size exceeded that of the sample.

Indeed, the presence of a peak preceding the Si (indicating a higher mass) was verified. However, we couldn't definitively confirm it as Gallium, as the peak was slightly ahead, possibly suggesting a heavier element. Since when the mass of the target atom struck by the projectile is higher, the energy lost by the projectile diminishes because less momentum is transferred to the target atom. Consequently, the backscattered particle attains a higher energy level, resulting in a shorter flight time for these backscattered projectiles as they reach the detector.

We need to employ an additional characterization method to identify the heavy element observed accurately. Two data sets were collected—one from the Total sample and another from the pristine sample—to establish the absence of the same peak in the latter. It would have been ideal to conduct a similar measurement on the 'peak' sample, which underwent

the same processing steps as the 'total' sample. Regrettably, there was not enough time for this step due to the extensive collection times (approximately a couple of hours) required.

Furthermore, due to the prolonged collection time for the orange line, some drift in the ToF spectrum occurred during collection, noticeable in the broadening of the photon peak. Consequently, there was increased uncertainty in determining the precise energy loss for the backscattered particles. The spectrum is illustrated in Figure 5.5. It is important to note that a more prominent photon peak indicates better conditions, as it signifies reduced background interference, enhanced resolution, and lower count variability.

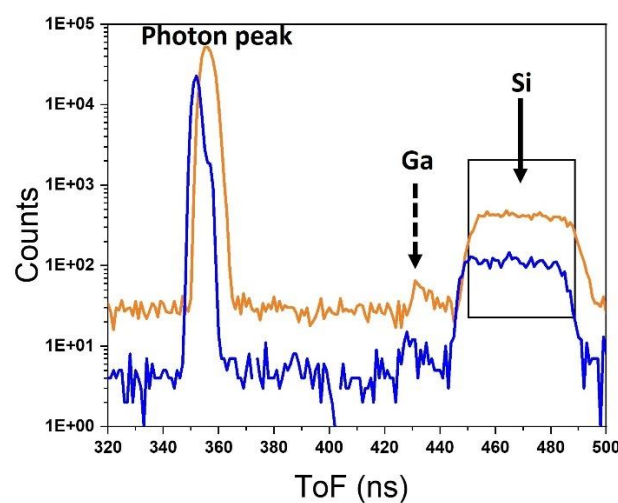


Figure 5.5: Backscattered TOF spectra for the 'total' Ga implanted Si sample taken during two different collections (orange data has prolonged collection time) applying 320 keV He⁺ beam. The peak ahead of the Si edge is believed to be the Ga, but it was not able to be confirmed within the scope of the experiments performed.

5.2.2 Galileo experiments

In the STIM measurements with Galileo, the Si membrane sample showed in Figure 5.1 was employed. The sample's orientation was arranged such that the ion beam initially penetrated the silicon layer, referred to as the 'front' (as indicated in Figure 5.1). Subsequently, experiments were repeated with the sample flipped over, causing the beam to first enter the Au layer. Interestingly, despite this change, identical TOF delay values were consistently observed, as depicted in Figure 5.6. For the STIM images in Figure 5.6 pixels with a value of 15 counts or higher were shown in white to highlight the sample's features. Furthermore, following the STIM measurements, an additional tear emerged on the membrane, accompanied by alterations in the sample's hole shapes during the handling

process for flipping the sample. The same TOF delay values were consistently maintained despite the sample modifications, as depicted in Figure 5.6.

To compare with the experimental findings, anticipated values were determined using the SRIM software tool[155] (Ziegler et al. 2010), which is accessible for free. The simulations were conducted with 20keV He⁺ ions, at 0° incident angle, and the 'Monolayer Collision Steps/Surface Sputtering' damage setting. Each simulation was performed with 1x10⁶ ions.

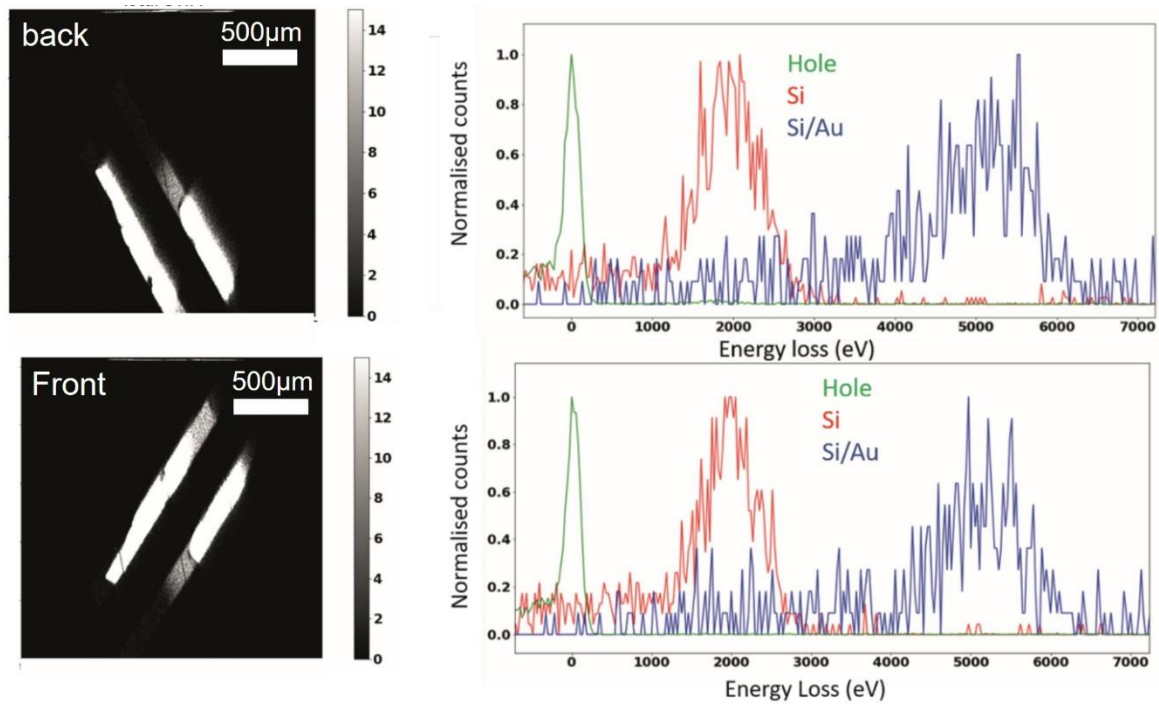


Figure 5.6: The TOF energy loss outcomes for the sample are presented in two orientations: one where it is flipped upside down (at the top row represented as back of the sample), and the other is when the sample is faced on the top surface (at the bottom row showed as front of the sample). In the STIM images, pixels that have a value of 15 or more are displayed in white, to enhance the visibility of the sample's characteristics.

The energy loss measurements and ToF peak analysis enable the plotting of energy loss maps. As depicted in Figure 5.6, each region of the sample exhibits a distinct position in the ToF spectrum, but these positions often overlap. To address this overlap, we can employ time window filtering to reconstruct STIM images, pinpointing the origins of counts within these specific ToF windows. Through this data filtering process, a 5D dataset, referred to as the STIM-IELS map[160], is generated, analogous to Scanning Transmission Electron Microscope-Electron Energy Loss Spectroscopy (STEM-EELS) maps [191].

Observing the impact of scattering angles on TOF spectra in the initial spectrum from MEIS (Figure 5.2), it is evident that ions scattered at larger angles generally experience greater

energy loss. Thus, when filtering the 5D dataset, accounting for the effect of scattering angles on energy loss is crucial. While correlations between scattering angles and energy loss have been explored in previous studies[192], [193], the comprehensive mapping of the complete (E, θ) space remains scarce in the literature. This deficiency leads us to discuss the upcoming paragraphs, where we compare our experimental data with simulation outcomes from SRIM.

In this section, we used SRIM simulations to samples with compositions of 5 nm C/15 nm Si/25 nm Au (referred to as C/Si/Au results) and 5 nm C/15 nm Si (referred to as C/Si results), subject to a dose of 1×10^6 ions. Figure 5.7 (b, d) illustrates the counts plotted in the (E, θ) plane, displayed in a logarithmic scale to emphasize key trends. The simulated results Figure 5.7 (b, d) exhibit a gradual shift in peak energies toward lower energies for high angle scattered ions. Thus, the energy peak shift is correlated with scattering angles with this phenomenon more pronounced in the C/Si plot Figure 5.7 (b). The histogram derived from the simulated results doesn't reveal any noticeable shift in the energy loss peak within the 0 to 3.4° range (using a histogram bin size of 50 eV). However, a noticeable shift becomes apparent at higher angles, indicating an energy loss increase of approximately 1.2 keV for a scattering angle of 40° compared to 0° . Unfortunately, there is a lack of angle-resolved energy loss studies about the thin silicon samples, although there are such data for gold in literature[194]. Consequently, we lack experimental data for comparison against these simulation outcomes.

The simulation results for C/Si/Au samples similarly displayed no particular shift between 0 and 3° , reflecting the behaviour observed in the C/Si simulations. However, a shift of approximately 500 eV became evident between 0 and 40° , corresponding to the observed increase in energy loss. These findings align well with outcomes from prior investigations, displaying comparable magnitudes of energy loss. For instance, a study reported an energy loss increase of up to 400 eV for 10 keV He^+ ions going through 13.1 nm Au and scattering to 40° [195]. In another study, Blume et al. determined a stopping power difference of 1.43 eV/angstrom between scattering angles of $0-25^\circ$ for 13 keV He^+ ions in polycrystalline gold[192]. This, in the context of our C/Si/Au segment investigations, corresponds to an additional energy loss of around 430 eV for a 25° scattering angle.

Further related literature[196] using 9 keV He⁺ ions, found an energy loss peak increase of 140 eV He⁺ ions scattered to 8° from monocrystalline 13.4 nm Au oriented in the $\langle 1\ 0\ 0 \rangle$ direction. Additionally, Famá et al.[197] reported an energy loss peak increase of 300 eV for 40° scattering of 9 keV He⁺ ions into 14.3 nm Au. In Figure 5.7 (c, d), it's essential to observe that when focusing on a small range of scattering angles, there is no observable shift in the energy loss peak in both experimental and simulated data. Furthermore, the angle range obtainable to the DLD is limited in this experiment, preventing the detection of the evident curvatures present in the polar plots of Figure 5.7 (b, d). However, when we compiled the data derived from ions scattered at low angles, specifically at or below 3.3°, a remarkable connection became apparent between the SRIM data and the experimental results (Figure 5.7(f)). Despite the broader beam of the experimental data, attributed to the shape of the 100 ns beam pulse, the peak centre shift remains identical.

Apart from the energy resolution limitation arising from restricted detector accessibility, another physical constraint in the present ToF measurements for energy loss is the time resolution of the detector. In our experimental setup, the detector employs a time bin of 6.9 ps, equivalent to a 0.5 eV energy loss for a 20 keV helium ion traveling a 0.53 m flight distance to the detector. In practice, the noise from the system and fluctuations in incident ion energy introduces uncertainties exceeding 6.9 ps in peak centre determination. This uncertainty can be decreased by enhancing the count rate or acquisition time to improve the signal-to-noise ratio. Also, ensuring a more stable power supply and ion source minimizes beam energy variations. Moreover, extending the flight path to the detector can enhance TOF resolution by increasing the time separation between arrival times for varying energies.

Figure 5.7 (e) illustrates the count variation (normalized to the value at 3°) relative to the scattering angle to investigate the spatial distribution of counts. The trend in experimental counts with respect to the scattering angle for C/Si/Au is qualitatively in line with the SRIM data, albeit slightly lower.

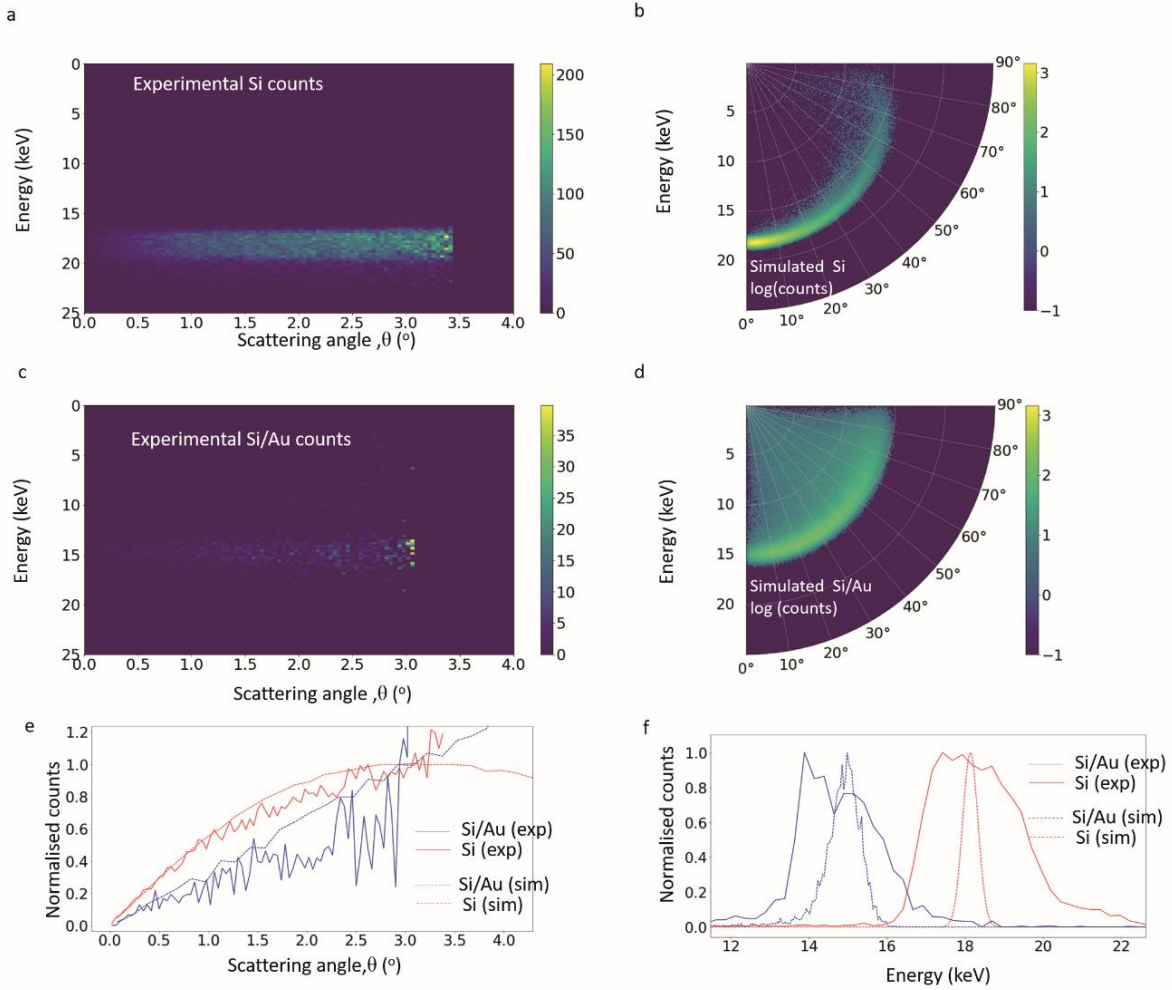


Figure 5.7: The energy-scattering angle maps are presented for both the experimental data (a, c) and the simulations (b, d). A comparison of intensity plots between the simulation and experiment is shown for the scattering angle (e) and energy (f).

The analysis of scattering angle results can reveal differences between two unlike regions of the sample comprising different elements. This differentiation remains noticeable even when the thickness of these regions results in identical peak energy losses. However, with increased thickness, both the peak energy loss and peak scattering angle are anticipated to rise. Consequently, if the thicknesses of the two regions were adjusted such that scattering angle peaks overlap, energy losses would differ. Therefore, the combination of both ToF and scattering angle measurements facilitates the differentiation of regions within a sample that might otherwise appear indistinguishable from just one of these measurements, which is illustrated in our published work[160].

5.3 Conclusions

By using ToF measurements involving 50 keV He^+ ions, we can observe the influence of varying scattering angles on ToF measurements. The effect is accomplished by comparing the complete detector image and a 2mm diameter section on the detector. Notably, altering the orientation of the sample on its implanted and unimplanted sides results in a modification of the channelling pattern. This shift is attributed to defects or contamination that arise on the implanted side. Identifying Ga^+ ions within the silicon crystal structure proved to be challenging. Additional experiments are proposed to provide conclusive evidence regarding the localization of Ga^+ ions within the crystal lattice. One viable approach is RBS, which can provide information about the position and composition of elements in the sample. Moreover, the strategy may contain a combined analysis involving XRD and EBSD or TKD. XRD can deliver an overall assessment of crystal quality. By applying EBSD/TKD to both sides of the membrane, one can pinpoint local crystal attributes within a thin layer near the surface. Additionally, we suggest conducting high-resolution SIMS and TEM analyses to fully comprehend Ga distribution and sample structure.

In the experiments involving 20keV He^+ ion transmission, we compute the behaviour of energy loss relative to scattering angle. Our simulations align with the experimentally observed outcomes. The spread of transmitted ion angles can be recorded, and the distribution of counts on the detector displays radial variations for Si samples with and without a gold layer. The dataset, which contains five dimensions (2D positions in the sample and detector planes, along with energy), can be examined by compiling energy spectra or images. The results indicates that the energy losses would no longer be the same and an energy loss contrast would arise if the thicknesses of the two sections were such that the scattering angle peaks overlapped. The capacity to discern between sections of a sample that would otherwise appear to be similar with only one of the two measurements is thus provided by the combination of TOF and scattering angle measurements as illustrated in this experiment.

Comparing Galileo results with MEIS obtained data for the top and bottom side image differences, one can conclude that, in the Si/Au samples the change in the contrast is due to the crystallinity differences as sample has been only coated. However, in the MEIS experiments, the variation in the results can also be due to the chemical differences.

6 Chapter 6: Correlative approaches using HIM

Within this chapter, we explored three distinct case studies for correlative microscopy approaches. Through these studies, we will unveil outcomes from combining HIM with complementary techniques using a correlative approach.

6.1 Case study 1: Correlative study of SE, SIMS for dopant profiling in ion implanted semiconductors

It was previously mentioned (state of the art 1) that variations in electronic properties at the surface could influence the contrast in SE imaging. In this case study, we compared the SE dopant contrast between SEM and HIM for electrically active dopants in silicon samples. This approach provides insights into comprehending the SE dopant contrast derived from SEM and HIM in boron-implanted samples and holds the potential for extension to other material systems.

6.1.1 Sample preparation workflow and imaging parameters

The dopant profiling contrast experiments involved boron-implanted Silicon. The implantation was carried out at the Surrey Ion Beam Centre in Guildford, UK. The substrate used for the experiment was a <100> crystal orientation n-type silicon wafer with phosphorous dopant atoms having a concentration of approximately 1×10^{15} at. cm⁻³. The implantation energy used was 190 keV, with a total dose of 10^{16} ions cm⁻². The high energy of implantation was chosen to ensure that the concentration maximum was located as deep as possible from the surface, specifically at a depth of 550 nm in this study, resulting in an extended concentration profile. The concentration at 550 nm depth from the surface was estimated using SRIM (version 2013)[198]. Therefore, the concentration profile at various depths revealed that the maximum concentration of boron (B) reached 5×10^{20} at. cm⁻³ (equivalent to 1 at. %) at a depth of 550 nm from the surface. To activate the boron dopants without causing significant diffusion, the implanted samples were annealed in a vacuum furnace at 700°C for 15 seconds, then gradually cooled until room temperature. The temperature and time parameters were carefully selected to minimize implantation damages and ensure efficient boron activation. Additional information on the implantation conditions can be found elsewhere[123].

SIMS depth profiling was performed using the CAMECA SC Ultra instrument. 1keV O_2^+ primary ion beam with 10 nA primary beam current was applied. The scanned region covered an area of $200 \times 200 \mu m^2$, and the area subjected to analysis had a diameter of 63 μm . We collected and analysed ions, specifically $^{30}Si^+$ and $^{11}B^+$. To determine the concentration, we followed a standard procedure that involved correlating the known implantation dose of 10^{16} ions cm^{-2} with the integrated B signal from SIMS measurements throughout the implantation depth. The time used for SIMS sputtering was converted into depth, assuming linear erosion. Also, we verified the crater depth after the experiment using a KLA-Tencor P17 profilometer.

Cross-sectional imaging was performed using a Hitachi SU-70 SEM. To minimize oxidation effects, the samples were cleaved prior to imaging. Standard imaging conditions were used, with an acceleration voltage of 2 kV and a probe current of 3.2 μA . The scan area covered 640×480 pixels.

For SE imaging in HIM, we used npSCOPE. The acceleration voltage was set to 25 kV, and the probe current ranged from 5.2 to 4.8 pA. The scan area consisted of 1024×1024 pixels, with a spot size of 3.9 nm and a dwell time of 80 μs .

The sample preparation and SIMS measurements was done by Shyam Kumar Chethala Neelakandhan. The EPFL group did the ECV analysis. My primary participation in this case study was the SE-HIM imaging.

6.1.2 Results and Discussion

As a result of implantation damage, boron atoms may become trapped within interstitial sites in the silicon lattice, hindering their ability to occupy electrically active substitutional sites. On the other hand, rapid annealing is known to induce transient enhanced diffusion, primarily due to the creation of vacancy clustering during implantation. These vacancies can facilitate the diffusion of implanted boron during thermal treatment, causing abnormal diffusion in certain boron atoms, while others become trapped as electrically inactive boron clusters[199]. Thus, the heat treatment can potentially rectify the implantation defects, allowing boron atoms to access the active substitutional sites.

To obtain the concentration peak and the overall dopant concentration, we conducted SIMS analysis, which is shown in the annex (Figure 8.2). The SIMS analysis revealed that the

implanted boron attains a peak concentration of 4.8×10^{20} atoms cm^{-3} . It's important to note that the SIMS profiles represent the total dopant concentration and do not differentiate between active and inactive boron atoms.

To estimate the electrically active dopant concentration, we performed ECV profiling. Figure 6.1 illustrates the results. Before the firing process, there is no evidence of any p-type doping in the sample, suggesting that the implanted boron remains inactive within the n-type silicon substrate. It's important to note that interpreting ECV profiles in amorphous materials is not well-established, and as a result, interpreting the ECV profile of the as-implanted sample is not straightforward. However, the previously amorphous regions crystallize after the heat treatment process, enabling a more meaningful interpretation of the ECV profiles. After annealing, ECV profile reveals an increasing p-type doping concentration at a depth of approximately 600 nm. The highest active dopant concentration measured was 1.59×10^{20} atoms cm^{-3} , reflecting a 33% activation efficiency and highlighting the effectiveness of annealing in activating the implanted boron. The red dots at the peak of the profile indicate some evidence of n-type doping. This variation in doping can be attributed to regional inhomogeneities arising from the clustering of boron during implantation and/or firing. Prior reports have demonstrated local boron precipitation when the implantation surpasses the solubility limit of boron[199]. Such local variations can result in regions with varying boron levels, leading to doping fluctuations within the material.

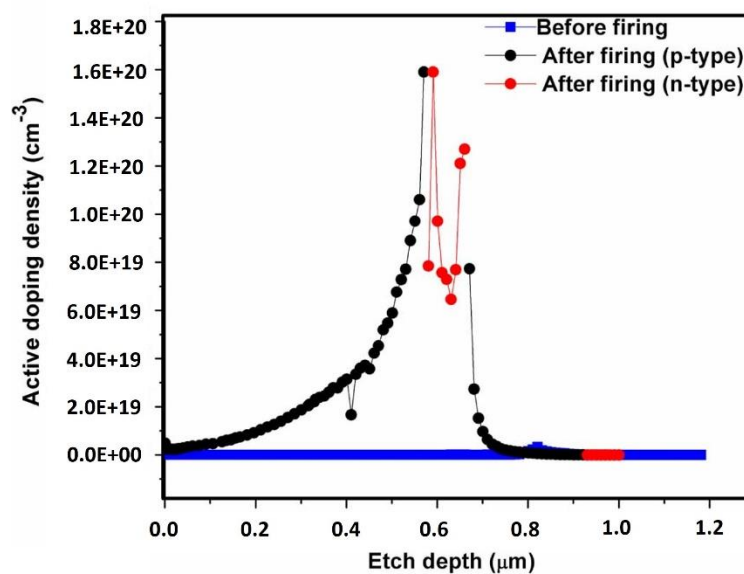


Figure 6.1: ECV profiles obtained from a silicon sample implanted with boron, both prior to and following heat treatment at 700°C.

Figure 6.2 presents a comparison of cross-sectional SE images obtained from both HIM and SEM for samples before and after annealing. Additionally, the contrast profile is displayed in the relevant section of the image. Since the contrast and brightness settings of the imaging acquisition is different in 2 different microscopes, we should ensure independence from the contrast and brightness settings. In this regard, we normalize the intensities for the contrast profile.

$$\text{Contrast percentage} = \frac{(I - I_b)}{(I + I_b)} \times 100$$

In the formula, “I” is the measured intensity and “I_b” is the average background intensity measured laterally over a range of 500 nm region (beginning 1 μm from the edge). Based on the SE images from SEM (Figure 6.2 (a, b)), it is evident that the boron intensity is not visible in the non-annealed samples. Instead, only a faint, diffuse contrast is observed in certain regions, potentially attributed to amorphization. Amorphization leads to varying work functions compared to crystalline silicon. The faint contrast could also be due to the presence of small active boron. Comparing Figure 6.2(a, b), we observe that the contrast of 15% is higher in Figure 6.2 (a) for the non-annealed sample. This discrepancy is due to a diffuse, broad, low-intensity peak and noisy signal. However, the sample after annealing displays a noticeable contrast, which is visually evident in Figure 6.2(b). Thus, the apparent contrast is attributed to the active boron. Also, the peak observed in the intensity profile in Figure 6.2 (b) aligns closely with the SIMS (Figure 8.2) and ECV (Figure 6.1) profiles, which provides clear evidence that the intensity is originating from the active boron. In addition, annealed sample shows improved contrast due to the crystallization of the matrix, effectively eliminating the contrast contributed by the amorphous region (Figure 6.2 (b, d)). Consequently, this may serve as a secondary explanation for attributing the contrast only to active boron. Note that, a similar trend is evident when examining the SE intensity derived from the HIM measurements. By calculating the contrast percentage, we can show that HIM exhibits a higher level of contrast when compared to SEM.

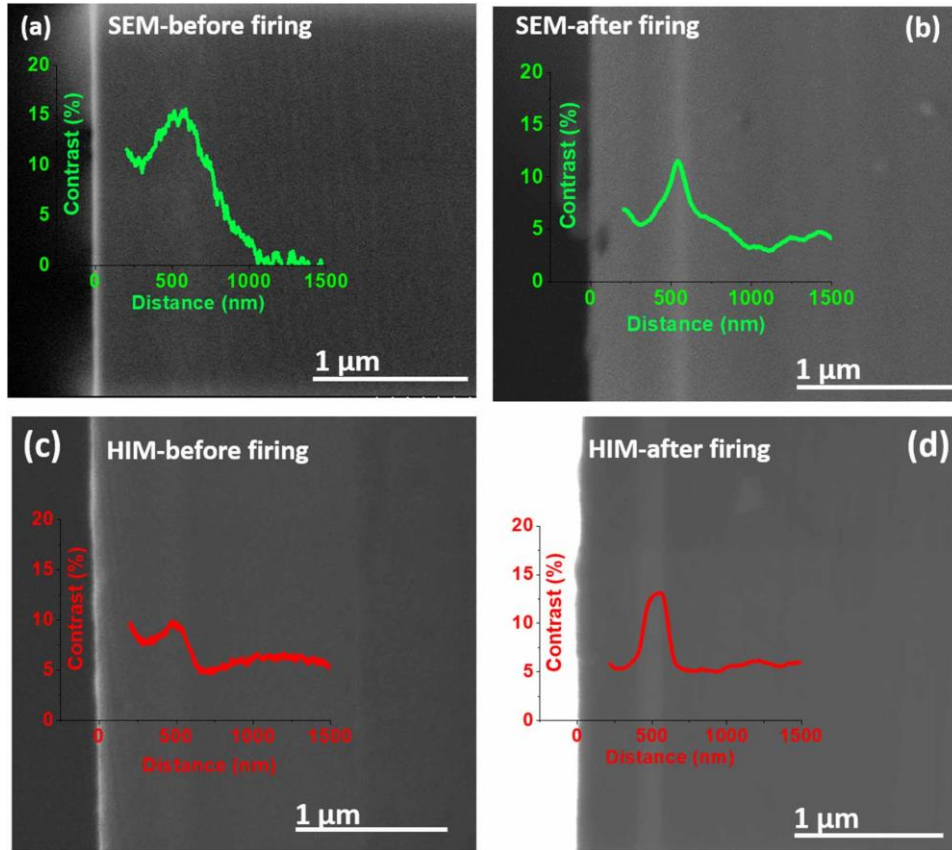


Figure 6.2: (a, b) SEM and (c, d) HIM images for contrast profile comparison from the cross-sectional implanted sample before and after firing, respectively. For SEM, the SE intensities were averaged across 480 pixels, while for HIM, the averaging encompassed 1024 pixels. The intensity profile within 200 nm from the edge is omitted in the image to prevent the influence of high intensities originating from the edge contrast.

We compared the normalized SE intensities from SEM and HIM for the annealed samples (Figure 6.3). The normalized intensity plots of SEM and HIM are aligned, compensating the misalignment caused by slight tilting of the sample during loading in the sample holder of SEM and HIM. The correction is minimal and does not particularly influence the FWHM of the profiles. Note that the dip observed before the SE intensity peak (around 300 nm), marked by a blue arrow in Figure 6.3, cannot be explained by varying dopant concentrations due to the lack of evidence in SIMS and ECV measurements.

The SEM intensity profile exhibits a narrow peak with a high background contribution. In contrast, the HIM intensity profile displays a clear peak with lower background. The peak belonging to HIM image profile is broader at the base since it suggests a lower (i.e., better) detection limit in HIM compared to SEM. Therefore, the broader peak does not show a poorer lateral resolution.

The ability of HIM to generate more localized SE even at higher accelerating voltages provides information about near-surface variations. Different primary energies can be

utilized for this purpose[200], [201]. On the other hand, in SEM, only by employing lower acceleration voltages the dopants can be visible due to the lower interaction volume and signal-to-noise ratio. Even in 2kV accelerating voltage, the contrast in SEM images would stem from a larger SE emission region when compared to the HIM at 25 kV[201]. Furthermore, as mentioned in Chapter 1, for SEM images, many SEs are generated from the backscattered electrons, which result in high background levels in SE-SEM compared to SE-HIM images, impacting the detection limit[202]. This aligns with previous studies on the samples grown by chemical vapor deposition, which also showed higher detection limits for HIM compared to SEM[37], [203].

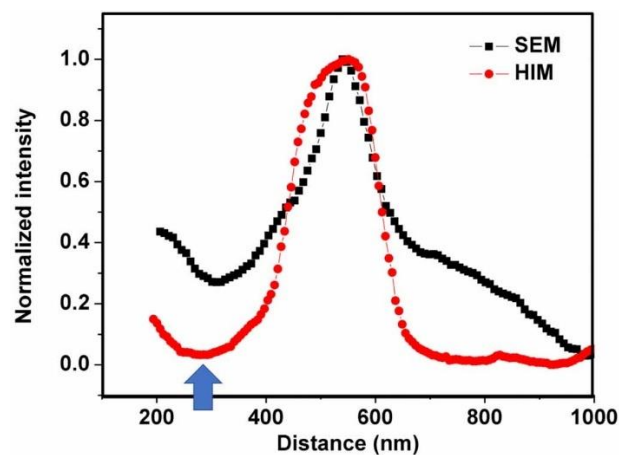


Figure 6.3: Normalized SE intensity profiles of SEM and HIM after firing.

Comparing the ECV profile (Figure 6.1) with the SE intensity profiles obtained from SEM and HIM (Figure 6.2), the ECV profile exhibits fluctuations in dopant concentration primarily within the higher concentration range. In contrast, both SE intensity profiles appear smoother and more consistent than the variations observed in the ECV profile.

The dip in the SE intensity profile just before the onset of the peak (indicated by the blue arrow in Figure 6.3) cannot be attributed to differences in dopant concentration as it is not present in ECV measurements.

The ECV measurement relies on establishing a semiconductor-electrolyte Schottky contact to form a depletion region at the sample's surface. Determining carrier concentration involves measuring the differential capacitance of the Schottky barrier formed at the semiconductor-electrolyte interface[204]. ECV measurements offer high sensitivity and a broad detection range due to their direct measurement of charge carrier concentration[205].

On the other hand, SE intensity profiling depends on local SE yield, which is associated with variations in the work function due to doping[36]. Surface states on a terminated crystal negatively affect the contrast between regions with different doping levels. For instance, bands bend downward at the surface for p-type doping and upward for n-type doping. Consequently, in cases of weak doping, SE contrast can be eliminated by pinning to a single Fermi-level, while it may still be detectable when doping levels are high enough to saturate the surface states [36].

Examining the dip in the intensity profile, previous research on photoemission thresholds in doped silicon[206] has revealed that the Fermi-level of a freshly cleaved sample remains fixed due to surface states, resulting in a nearly constant work-function irrespective of the doping type and concentration underneath. Thus, the dip in the SE intensity cannot be explained only by surface band bending. Instead, the dip may be related to the extent of the depletion region within the bulk and its interaction with the SE escape depth. While SEM and HIM images offer higher resolution, dopant profiling is constrained by the surface potential caused by surface band bending[36], [39]. As a result, small local variations in the dopant depth profile, detectable through ECV, may not be apparent in an SE intensity profile.

Additionally, SE intensity profiles are influenced by the volume from which SE emission occurs. Commercial SEM and HIM often scale SE intensity values between 0 and 255 (8-bit images), further smoothing out subtle local intensity variations and reducing the dynamic range.

6.1.3 Conclusions from Case Study 1

We investigated the electrically active dopants in boron-implanted silicon samples using correlative imaging and profiling approaches. SE images from SEM and HIM were used to investigate the SE contrast of electrically active dopants in boron implanted silicon samples and correlated them with SIMS and ECV profiles.

SE images captured by SEM and HIM showed distinct contrasts from the active boron distribution, with HIM exhibiting more evident contrast than SEM. The HIM images displayed a well-defined peak and reduced background contribution.

We demonstrated the efficiency of SE dopant profiling as a rapid method for generating 2D visualizations of electrically active dopants in ion-implanted samples. This rapid method

offers a notable advantage compared to the limited 1D data acquired through depth profiling using SIMS or ECV. Nevertheless, SE imaging proves insufficient in cases where local dopant concentrations surpass the solubility threshold, requiring complementary characterization techniques like SIMS and ECV to ensure a comprehensive study of the doping features.

6.2 Case study 2: A correlative SE and SIMS approach for perovskite crystallization kinetics and microstructure

In this section, we introduce research work done on a tandem solar cell device, drawing from previous research[207]. This device incorporates a perovskite layer that is uniformly coated on a silicon bottom cell featuring micrometric pyramids, which is the industry standard to improve its photocurrent generation. Through a correlative characterization approach, effects of the additive, 2,3,4,5,6-pentafluorobenzylphosphonic acid (FBPac) on the perovskite solar cell's performance were investigated.

6.2.1 Sample preparation workflow

For SIMS, SEM, QFLS and XPS investigations the utilization of flat glass/indium tin oxide (ITO) substrates as a foundation for the hole transport layer (HTL) coating was employed. The study encompassed the deployment of three distinct HTL: 2,2',7,7'-tetra (N, N-di-tolyl) amino-9,9-spiro-bifluorene (spiro-TTB), N4,N4,N4'',N4''-tetra([1,1'-biphenyl]-4-yl)-[1,1':4',1''-terphenyl]-4,400-diamine (TaTM), and [4-(3,6-dimethyl-9H-carbazol-9-yl)butyl]phosphonic acid (Me-4PACz). These three HTLs were chosen based on their compatibility with the textured surface. Following the HTL coating, a perovskite thin film was deposited onto the coated substrates using a hybrid two-step deposition technique[207]. Subsequently, a CsBr/PbI₂ template was co-evaporated onto the glass substrates or glass/ITO/HTL stacks before spin coating with an organo-halide solution of FAPb, FAI, and FBPac in some cases. Through a thermal annealing process conducted at 150°C in an ambient atmosphere, the films underwent a transformation into the perovskite phase. The deposition of the C₆₀ electron transport layer (ETL) was accomplished via thermal evaporation within a high vacuum environment, effectively completing certain layers within the perovskite stack.

The perovskite films for current-voltage (J-V) measurements were integrated into single junctions with glass/ITO/HTL/perovskite/C₆₀/bathocuproine (BCP) (or SnO_x)/Cu (or Ag) configurations, with an active area of approximately 0.49 cm².

Additionally, we fabricated 1-cm² tandem cells with adjusted perovskite deposition conditions on silicon heterojunction bottom cells featuring pyramids measuring 2 to 3 mm on both sides of the wafer (Figure 8.3)[208].

The sample preparation and synthesis were carried out by our collaborators in the PV lab at EPFL University, while my primary involvement centred around the application of SIMS to analyse the composition and establish correlations with the properties of the perovskite film, specifically in relation to its interactions with FBPAc. For further details regarding the sample preparation the reader is referred to the cited source[119]. SIMS within the Nanofab HIM-SIMS were utilized for the analysis of the composition, property correlation, and interactions of the perovskite film with FBPAc. Note that a range of characterization methodologies were employed in PV lab, including SEM, QFLS, XPS, J-V curve measurements. A Gemini 2 SEM (manufactured by Zeiss) was employed to capture top-view images of the perovskite thin films deposited on ITO/glass substrates.

6.2.2 Results and Discussion

6.2.2.1 Recognizing and mitigation of voltage losses in perovskite top cells by adding FBPAc

In the absence of FBPAc additive, introducing the C₆₀ (ETL) onto the perovskite (as represented by the filled diamond in Figure 8.4) leads to significant losses in QFLS, ranging from -100 to -50 meV. These losses occur in addition to the losses induced by the HTL and are primarily due to the formation of trap states within the initial monolayer of C₆₀ [209]. Conversely, when FBPAc is incorporated into the perovskite film synthesis, it mitigates some of the losses induced by the ETL. As a result, there is an increase in QFLS of approximately +100 meV compared to FBPAc-free films. Also, FBPAc has the ability to stop surface defects related to Pb²⁺/Pb⁰, (as illustrated in Figure 8.4 through XPS data). FBPAc's phosphonic group corresponds to Pb-related defects, a phenomenon previously demonstrated elsewhere[209]. This correspondence effectively reduces the number of nonradiative recombination states at the top surface[210]. Moreover, the positive influence of FBPAc is

particularly noticeable when C_{60} is present. FBPAc likely splits the perovskite from the C_{60} layer, thereby diminishing the number of deep trap states within C_{60} that may arise when it directly contacts the perovskite[211].

6.2.2.2 Resulting microstructure and SIMS analysis of perovskite

FBPAc decelerates the transformation of the $CsBr/PbI_2$ template into the perovskite phase due to a competitive interaction between FBPAc and other perovskite precursors, namely FAI and FAPbBr₃, for binding with Pb^{2+} ions[210]. This difference in formation kinetics proves advantageous, resulting in films that exhibit larger and more distinct perovskite domains. The presence of FBPAc may hinder the initiation of new perovskite grains or domains, as evidenced by top-view SEM images (see Figure 6.4(a)). These images reveal submicrometric dark regions in perovskite films that incorporate FBPAc. Figure 6.4 displays the images of both the samples, one with additives and the other without.

In this case, we employed SIMS to investigate the distribution pattern of FBPAc clusters on the surface of the perovskite film. Figure 6.4(b) shows the SIMS images, which was unveiled that FBPAc formed clusters on the perovskite film's surface. These clusters were distinguished as regions abundant in both fluorine (F) and carbon (C), elements found within FBPAc (Figure 6.4(b)). Conversely, films without FBPAc exhibit an absence of clustering and manifest a diminished presence of fluorine (F) and carbon (C) on their surface (Figure 6.4(b-c)).

The significant reduction in QFLS losses strongly recommends that FBPAc is not only present within the surface clusters but also distributed between them. This assumption is based on the logarithmic relationship between QFLS and surface recombination current, implying that FBPAc is effectively reducing the surface recombination current by several orders of magnitude. If FBPAc were exclusively located within the clusters detected by SIMS, meaning that approximately 90% of the film surface would be devoid of FBPAc, the difference in QFLS would be limited to around 3 meV [$\Delta QFLS = 25.7 \text{ meV} \times \ln(1/0.9) \cong 3 \text{ meV}$]. However, we observe a significant QFLS gain of over 50 meV when C_{60} is present (as shown in Figure 8.4), indicating that FBPAc is also distributed in regions between the clusters. In summary, FBPAc functions to passivate Pb-related defects and mitigates the formation of trap states within

the C_{60} layer by segregating on the top surface of the perovskite. Additionally, any excess FBPac forms clusters on the surface.

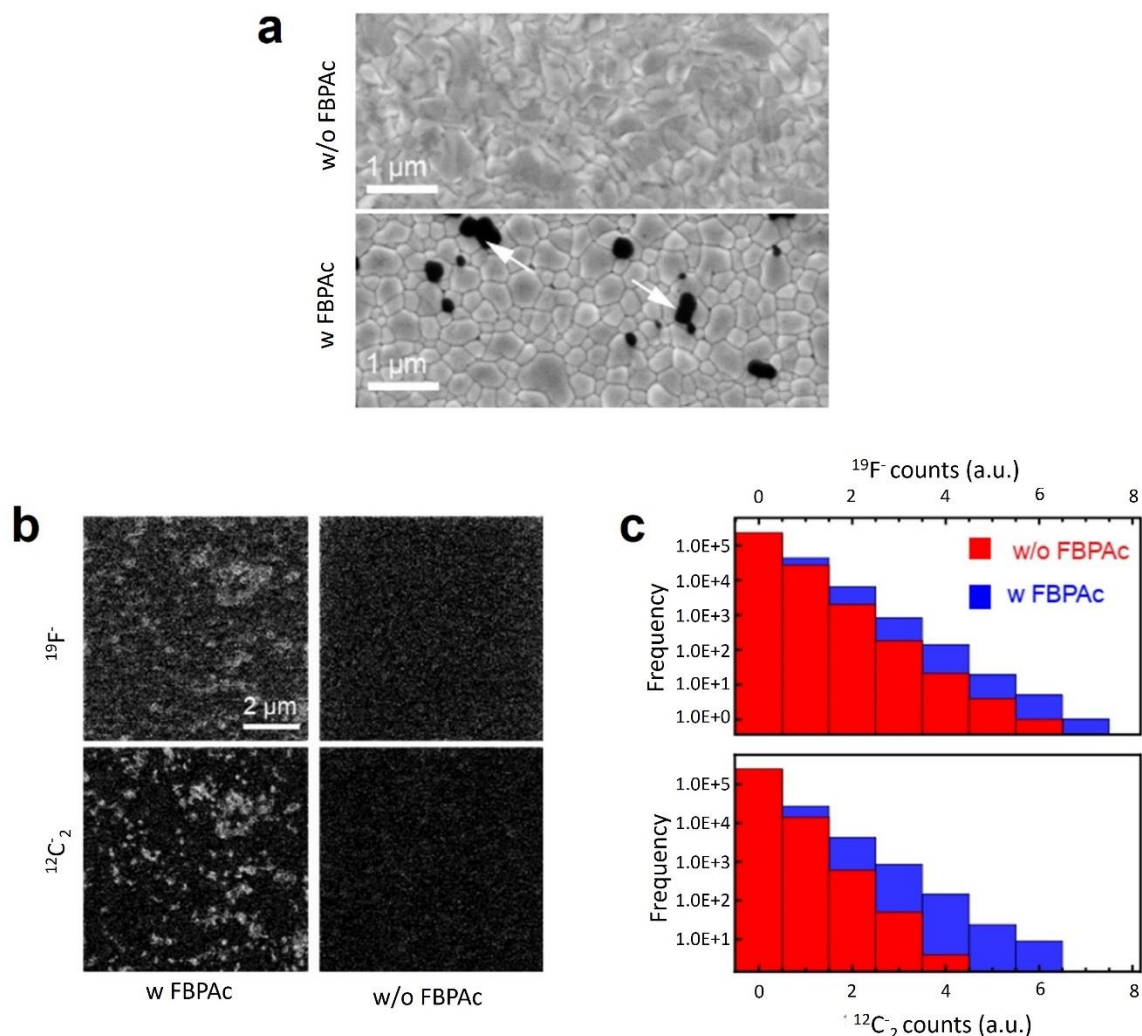


Figure 6.4: Microstructural investigations of perovskite with and without FBPac. (a) SEM images showing the different surface morphologies, arrows pointing to the FBPac clusters. (b) SIMS images of the $^{19}F^-$ and $^{12}C_2^-$ signals and the bright areas correspond to higher signal counts, while the dark regions indicate lower signal counts. (c) The histograms shown here correspond to the $^{19}F^-$ and $^{12}C_2^-$ SIMS signals displayed in (b).

6.2.2.3 Perovskite single junctions and perovskite/c-Si tandem solar cells performance analysis

When Me-4PACz and FBPac are combined, it leads to a PCE of up to 19.5%. Notably, adjusting the concentration of FBPac within the FABr:FAI solution, ranging from 2.5 to 7.5 mM, does not significantly impact the performance (as shown in Figure 8.5). This observation suggests that the excess of FBPac (as seen in Figure 6.4(b)) does not impede charge transport across the perovskite/ C_{60} interface.

A tandem cell incorporating Me-4PACz and FBPAC was transmitted to the National Renewable Energy Laboratory (NREL) for certification. The results of achieving a remarkable 31.25% efficiency in perovskite/c-Si tandem solar cells is attributed to the synergistic effects of Me-4PACz and FBPAC, coupled with a pyramidal texture on the front side of the tandem showed in Figure 6.5. The certified relative external quantum efficiency (EQE), as presented in Figure 6.5(a), indicates that the tandem cell was slightly limited by the top cell, and both sub cells exhibited a photocurrent density (J_{sc}) greater than 20 mA/cm².

The device's stabilized J-V characteristics were assessed using the asymptotic maximum power (P_{max}) scan method under standard test conditions (STC) which include a temperature of 25°C, an illumination intensity of 1000 W/m², and the AM1.5G spectrum (as depicted in Figure 6.5 (b, and c)[212]. The cell achieved a V_{oc} of 1.91 V, a J_{sc} of 20.47 mA/cm², and a fill factor (FF) of 79.8%. This resulted in a certified PCE of 31.25%, based on an aperture area of 1.1677 cm².

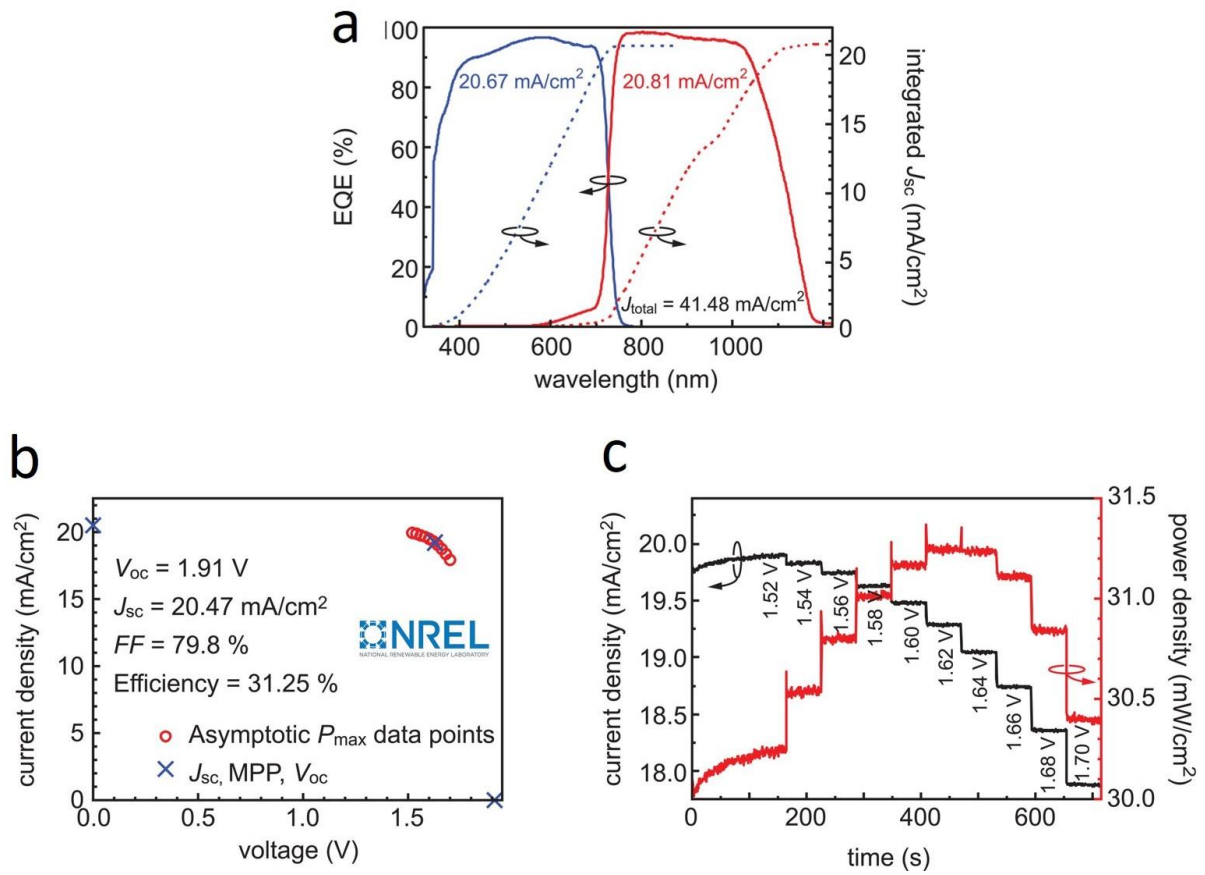


Figure 6.5: Independent certification reveals the EQE of perovskite/c-Si tandem solar cells (a), the asymptotic maximum power (P_{max}) scan (b), and the tracking of current density and power density around P_{max} (c).

6.2.3 Conclusions from Case Study 2

By introducing an additive into the processing sequence, we have been able to control the crystallization of the perovskite layer and reduce recombination losses that typically occur at the interface between the perovskite layer and the electron-selective contact (in this case, buckminsterfullerene or C_{60}). And together with a micrometric texture which is standard in the c-Si PV industry, we have successfully developed a device with an active area measuring 1.17 square centimetres, achieving a certified power conversion efficiency of 31.25%.

In these investigations, the SIMS analysis provided a clear picture of how FBPAc was distributed on the perovskite film's surface, forming clusters rich in fluorine and carbon. Based on SIMS data, FBPAc is visible on the perovskite top surface, which interacts with Pb-related defects in perovskite through its phosphonic acid group. Furthermore, the FBPAc's presence in the clusters also contributed to improved efficiency and performance of the

solar cell. Therefore, we were able to optimize the perovskite solar cell design and enhance its overall energy conversion efficiency.

6.3 Case study 3: Correlative approach for cesium-formamidinium metal-halide perovskites

The pursuit of achieving metal-halide perovskite solar cells (PSCs) with exceptional PCEs has primarily centred around formulations rich in formamidinium lead iodide (FAPbI₃, where FA⁺ represents the formamidinium ion). This focus is attributed to the favourable characteristics of FAPbI₃, such as its nearly ideal bandgap of approximately 1.5 eV, which closely aligns with the maximum of the Shockley-Queisser limit (1.33 eV). Additionally, FAPbI₃ exhibits remarkable thermal stability in comparison to perovskite compositions based on methylammonium (MA⁺) [213]·[214]·[215]·[216]·[217]. The measured V_{oc} of MAPbI₃ cells under dark conditions (with devices stored in a dry box and measured daily in ambient conditions with $\geq 70\%$ relative humidity) exhibits the stability profile characteristic of unencapsulated MAPbI₃ perovskite solar cells. Notably, MAPbI₃ cells experience a rapid decline and complete degradation in approximately 10 days, whereas FAPbI₃ cells demonstrate a longer stability, lasting around 30 days[218]. In our case study, we analysed the effect of cationic alloying in Cs_xFA_{1-x}PbI₃ perovskite absorbers specially on the local defects. Also, we investigated the final optoelectronic effects and device operation.

6.3.1 Sample preparation workflow

Solution-based process used to fabricate mixed-cation Cs_xFA_{1-x}PbI₃ perovskite absorbers (with x values ranging from 0 to 0.3; please note that these concentrations are nominal and are derived from the compositions in the precursor inks). The perovskite films were directly spin-coated on ultra-thin carbon-coated copper (Cu) TEM grids that were stuck to ITO glass using a Kapton tape. To deposit electron-transparent films, with a thickness of less than 200 nm, we utilized diluted ink concentrations while maintaining identical solvents and processing conditions employed in the fabrication of solar cells. This approach was chosen to obtain thin film samples suitable for STIM and TEM imaging. To minimize any environmental potential-induced degradations such as moisture exposure, the samples were placed in a nitrogen (N₂)-filled cylinder immediately after deposition inside the

glovebox and then transferred into the STIM and TEM chambers in less than 5 mins of air exposure.

BF images and SAED patterns were captured using a Talos F200S TEM running at 200 kV, situated within the Centre interdisciplinaire de Microscopie électronique (Cime) at EPFL's Lausanne campus. To minimize potential electron beam-induced artifacts, we adopted low-dose TEM imaging conditions, maintaining an electron dose rate of approximately 1 electron per square angstrom per second ($\text{e}\text{\AA}^{-2} \text{s}^{-1}$). All TEM BF micrographs and diffraction patterns were sourced from areas of the sample that had not been previously exposed to electron beams. Importantly, the specimen orientation was preserved without any tilting, ensuring that SAED patterns were acquired in the same orientation as the domains were initially found. To facilitate the capture of localized diffraction patterns, a small objective aperture was utilized. My main contribution to these investigations was SIMS and STIM analyses which was performed in Nanofab HIM-SIMS and npSCOPE in LIST.

For the long-term operational stability for different Cs content x in $\text{Cs}_x\text{FA}_{1-x}\text{PbI}_3$ perovskite devices, the devices were constructed using an inverted (p-i-n) configuration, utilizing indium-tin oxide (ITO) glass as the substrate, followed by layers of (2-(3,6-Dimethoxy-9H-carbazol-9-yl)ethyl)phosphonic acid (MeO-2PACz), perovskite, Buckminsterfullerene (C_{60}), Tin (IV) Oxide (SnO_2), and Silver (Ag) (illustrated in annex, Figure 8.8(a)).

We conducted aging experiments on encapsulated devices by subjecting them to continuous full-spectrum simulated 1 sun illumination at 35 °C, all while maintaining open-circuit conditions within a nitrogen (N_2) environment. The encapsulation process involved using a glass/glass technique sealed within a N_2 environment and employing UV-epoxy resin. It's worth noting that aging photovoltaic solar cells under open-circuit conditions is known to expedite degradation compared to employing maximum power point tracking (MPPT)[219].

The sample preparation, TEM, C-AFM, photocurrent analysis and performance tests, were done by another Ph.D. student, Mostafa Othman and his colleagues, from PV lab at EPFL University.

6.3.2 Results and discussion

The technique of alloying FA^+ with Cs^+ is often used to promote structural stabilization of the desirable $\alpha\text{-FAPbI}_3$ cubic phase in halide perovskite devices. However, maintaining such high performance in practical operating conditions has proven to be challenging due to the structural instability of FAPbI_3 . This instability causes the preferred photoactive $\alpha\text{-FAPbI}_3$ cubic phase to transform into a non-perovskite wide-bandgap photo-inactive $\delta\text{-FAPbI}_3$ phase at room temperature[220]. To address this issue, various approaches have been explored to suppress the formation of the $\delta\text{-FAPbI}_3$ phase. One notable strategy involves the incorporation of cesium (Cs^+) alloying with FA^+ on the A-site of the perovskite crystal structure[221]. This cesium-formamidinium (CsFA) cation mixing has been shown to enhance the stability of the cubic perovskite structure. Therefore, we aim to uncover the underlying local structural changes, specifically structural defects in the $\text{Cs}_x\text{FA}_{1-x}\text{PbI}_3$ perovskite system through TEM. Stacking faults refer to structural defects in this context that occur within the crystalline lattice of CsFA perovskite absorbers. These defects are essentially disruptions or deviations from the regular arrangement of atoms in the crystal lattice, leading to altered stacking sequences of atomic layers. Various factors can cause stacking faults during the crystal growth process or due to the integration of different ions, such as Cs^+ and FA^+ , into the crystal structure.

6.3.2.1 TEM results

We investigated stacking faults (SFs) using the mixed-cation $\text{Cs}_x\text{FA}_{1-x}\text{PbI}_3$ perovskite absorbers by low-dose BF-TEM imaging and SAED patterns from individual regions (Figure 6.6). The presence of SFs was found with striped contrasts, ranging from 5 to 7 nm in width, across numerous regions on the film's surface (Figure 6.6(a)) in the FAPbI_3 (i.e., $\text{Cs}_x=0$) sample. A SAED pattern obtained from the region highlighted by the yellow circle in Figure 6.6(a) shows $\{111\}_\text{C}$ twin domains oriented near the $[011]_\text{C}$ zone axis of the cubic crystal structure of the perovskite, with a lattice parameter of 6.3 Å (Figure 6.6(d)). These SFs indicate the presence of nanoscale-hexagonal clusters within the cubic structure of the perovskite, which cannot be resolved using traditional low-resolution Bragg Brentano XRD measurements [222].[223]. From the TEM images we found that by increasing the Cs content in the $\text{Cs}_x\text{FA}_{1-x}\text{PbI}_3$ perovskite films, the prevalence of stacking faults decreased (at $\text{Cs}_{0.05}$ & $\text{Cs}_{0.1}$). At $\text{Cs}_{0.15}\text{FA}_{0.85}\text{PbI}_3$, no stacking faults were observed, which suggests the

introduction of Cs ions can influence the defect density and the local structure of the material. Continued elevation in Cs content ($x = 0.2 - 0.3$) leads to undesired secondary phases rich in Cs, termed δ -CsPbI₃, as illustrated in Figure 6.6(c, f).

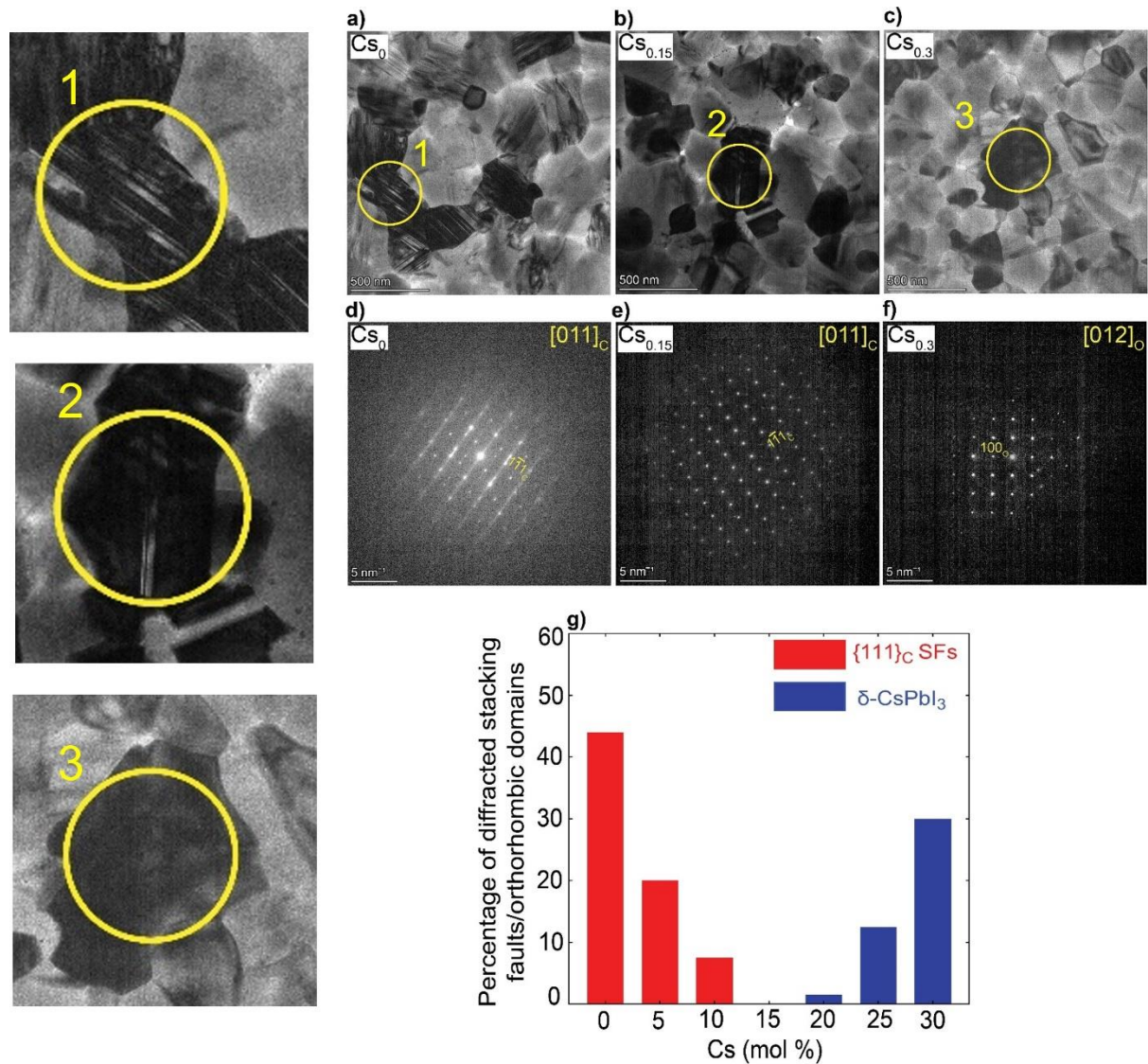


Figure 6.6: Nano-structural analysis of the Cs_xFA_{1-x}PbI₃ perovskite films: a-c) BF micrographs, d-f) The associated SAED patterns (The Cs content and zone axis are written on the top left and right side of the images, respectively), The yellow circles indicate the position of the selected-area for SAED pattern acquisition which are zoomed as 1, 2, 3 from a, b, c images respectively; and g) Histograms illustrating the impact of the Cs content on the defect density. The estimated percentages are based on the number of diffracted domains (from all the obtained micrographs) featuring {111}_c SFs or δ -CsPbI₃ phases with respect to all the other different phases present in the samples.

6.3.2.2 SIMS results

The formation of SFs is probably linked to heterogeneous distribution of cations (specifically, Cs⁺ and FA⁺). This uneven distribution enables microscopically unstable regions to form inside the cubic perovskite domains such as the hexagonal photo-inactive δ -FAPbI₃ phase. To substantiate this hypothesis, we conducted SIMS imaging to examine the elemental distribution within CsFA perovskite films. The elemental mapping of Cs, Pb, C, N, and I

(Figure 6.7 (a-o)) reveals a relatively homogenous distribution within the $\text{Cs}_{0.15}\text{FA}_{0.85}\text{PbI}_3$ perovskite absorber, except for regions rich in Pb and I, which are likely PbI_2 clusters. This distribution pattern contrasts with what is observed in the FAPbI_3 and $\text{Cs}_{0.3}\text{FA}_{0.7}\text{PbI}_3$ perovskite films, aligning with our initial hypothesis. Figure 6.7(k-o)) clearly reveals the distinct emergence of segregated CsPbI_3 -rich clusters. Please note that the slightly elevated signal observed on the left half of the Cs map in Figure 6.7(h) is an artifact. This artifact may be attributed to minor variations in the extraction efficiencies of secondary ions during the experimental process.

Based on TEM and SIMS results, introducing Cs alters the intrinsic defect density of FAPbI_3 perovskite. Lower Cs concentrations diminish the occurrence of SFs, reaching a minimum at $\text{Cs}_{0.15}$, while elevated Cs contents in compositions provoke the formation of δ - CsPbI_3 Orthorhombic phases (Figure 6.6(g)).

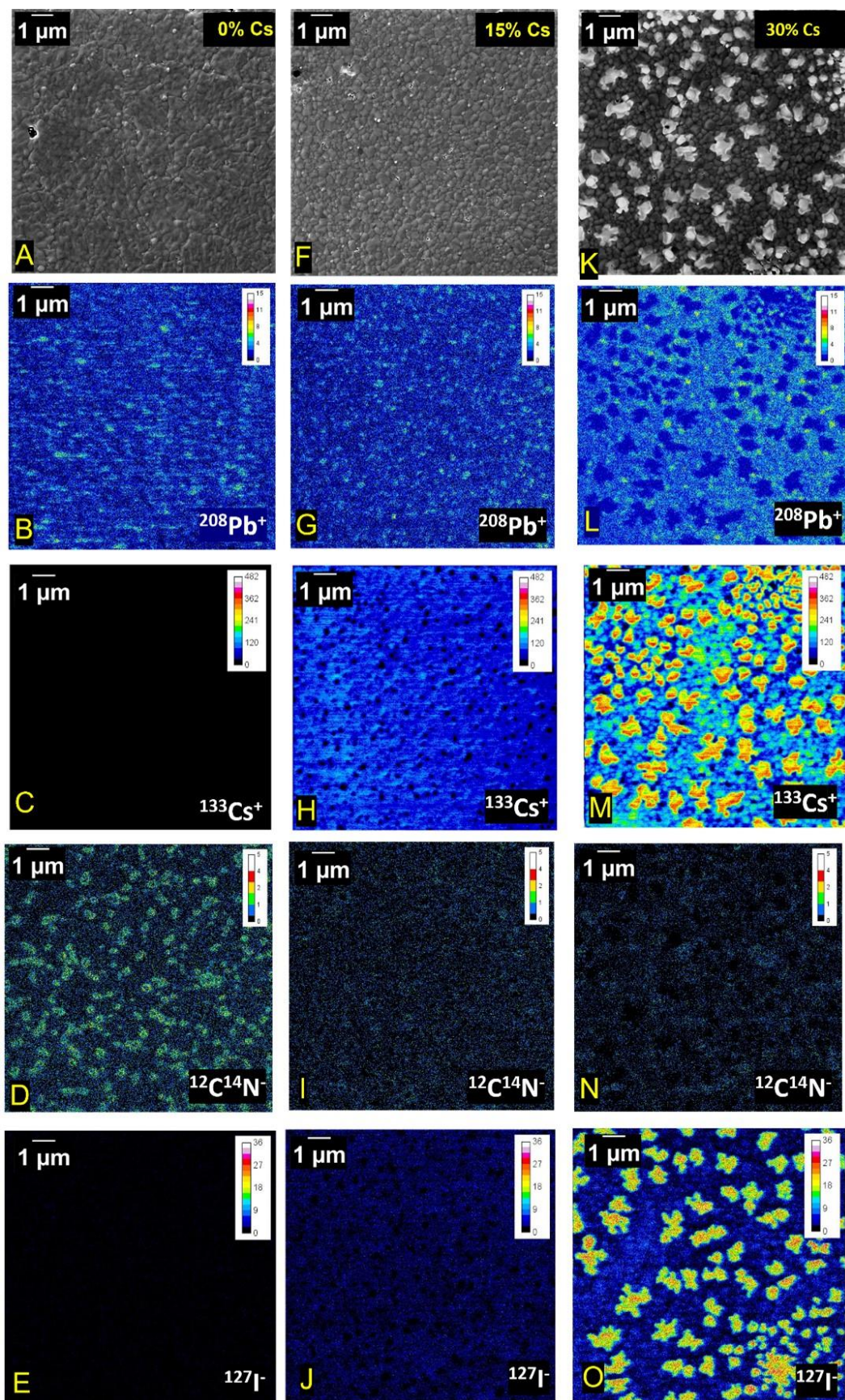


Figure 6.7: Elemental analysis for the a-e) FAPbI_3 , f-j) $\text{Cs}_{0.15}\text{FA}_{0.85}\text{PbI}_3$ and k-o) $\text{Cs}_{0.3}\text{FA}_{0.7}\text{PbI}_3$ perovskite films.

6.3.2.3 Optoelectronic and performance tests

We conducted additional characterization methods to evaluate the impact of SFs on the optical properties and performance of the halide perovskites. Given that these characterization methods are not our primary area of expertise, I will briefly summarize the conclusions drawn from these results together with the EPFL team. However, the reader can refer to the corresponding plots in the annex for more detailed information.

To assess the nanoscale local photocurrent, we employed conductive-atomic force microscopy (C-AFM) with illumination provided by a white LED, simulating approximately 1 sun excitation. As depicted in the annex (Figure 8.6(d & f)) concerning the Cs_0 and $\text{Cs}_{0.3}$ stacks, the photoconductivity is significantly reduced in areas specifically associated with the presence of SFs on terraced-edge surfaces (refer to annex Figure 8.7) and extensive insulating regions resembling the CsPbI_3 -rich clusters (Figure 6.7). In contrast, the spatial distribution of photo-current conductivity and its uniformity reach their peak in the $\text{Cs}_{0.15}\text{FA}_{0.85}\text{PbI}_3$ perovskite system, indicating efficient carrier transport and collection properties (Figure 8.6(e)). These findings strongly suggest that these nanoscale defect impurities are likely causing impediments in charge transport, resulting in fill-factor (FF) losses in devices.

As a final assessment, we conducted long-term operational stability tests on perovskite devices containing varying Cs content (x) in the $\text{Cs}_x\text{FA}_{1-x}\text{PbI}_3$ composition, all while maintaining the same hole/electron transport layers and device configuration. Remarkably, the $\text{Cs}_{0.15}\text{FA}_{0.85}\text{PbI}_3$ perovskite device with optimal Cs content displayed outstanding stability, retaining 85% of its initial PCE over a duration of 1400 hours (Figure 8.8(b)). In contrast, all other devices exhibited degradation and ultimately failed at different and shorter time intervals, evident by their yellowish appearance (Figure 8.8 (c-i)), particularly in the active device area. This discoloration is indicative of the formation of PbI_2 as a by-product of absorber layer decomposition[224]. This remarkable stability achievement can be attributed to the inherent robustness of the perovskite film crystallinity and the defect-free metrically cubic photo-active absorber layer.

We evaluated the device performance metrics for these different processed perovskite absorbers in complete devices (Figure 8.8 (j-m)). The $\text{Cs}_{0.15}\text{FA}_{0.85}\text{PbI}_3$ perovskite film exhibited outstanding device parameters, with the top-performing device achieving a

maximum PCE of 19.3%, a J_{SC} of 22.8 mA cm⁻², an open-circuit voltage (V_{OC}) of 1.02 V, and a fill-factor of 82.8%.

6.3.2.4 STIM images approach for investigating potential characterization benefits

We observed a correlation between SIMS and TEM images; however, it would have been significantly more practical if these imaging techniques were executed within the same apparatus, eliminating the need to remove the sample from the chamber. This practical consideration has spurred our motivation to attempt visualizing SFs using STIM and subsequently performing SIMS on the same ROI. To achieve this objective, we acquired STIM images to capture the SFs, and these images were then compared to TEM images in Figure 6.8. As evident, the SFs are not discernible in the STIM images. However, the effectiveness of STIM becomes apparent when observing that grain boundaries appear brighter in STIM images, indicating reduced thickness because of their brightness. However, the crucial takeaway here is that TEM images lack this contrast, potentially leading to a misinterpretation that the region is uniformly flat or has a very little thickness variation. This highlights the greater sensitivity of STIM in detecting variations in thickness. To have a complementary data, we conducted SIMS on the identical ROI, we encountered difficulty in establishing a correlation between the SIMS results and the SFs, primarily due to the invisibility of SFs in the STIM images.

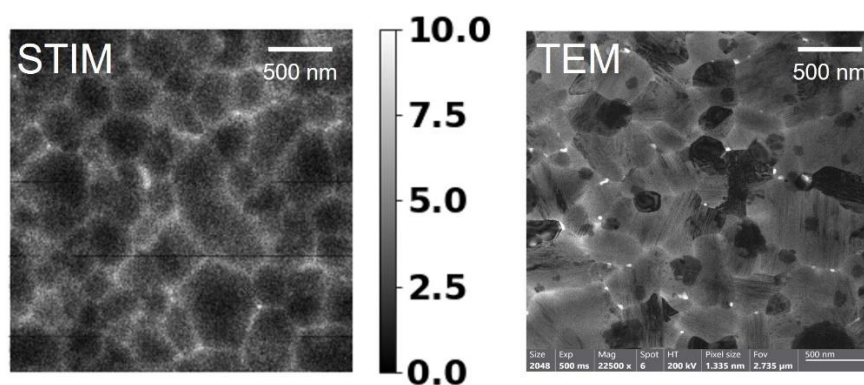


Figure 6.8: Comparison of TEM with STIM images.

6.3.3 Conclusions

In summary, this study emphasizes the intricate interplay between defects in crystallography, material properties, and device performance within mixed-cation $\text{Cs}_x\text{FA}_{1-x}\text{PbI}_3$ perovskite absorbers.

The formation of the $\{111\}_C$ SFs is likely attributed to heterogeneous cation (Cs^+ to FA^+) distributions, which would allow microscopically unstable regions to form inside the cubic perovskite domains such as the hexagonal photo-inactive $\delta\text{-FAPbI}_3$ phase. SIMs verified this explanation by indicating the relatively uniform distribution in the $\text{Cs}_{0.15}\text{FA}_{0.85}\text{PbI}_3$ perovskite absorber (with the exception of Pb-I rich clusters, likely PbI_2). Thus, Cs alloying changes the intrinsic FAPbI_3 perovskite defect density in which low Cs concentrations ($\text{Cs} < 15 \text{ mol\%}$) reduce the $\{111\}_C$ SFs with a minimum reached at $\text{Cs}_{0.15}$.

Utilizing SAED patterns alongside other methods, the study indicates that precise Cs^+ adjustments (as in $\text{Cs}_{0.15}\text{FA}_{0.85}\text{PbI}_3$) lead to the minimization of SFs and an enhancement in the perovskite films' electronic conductivity. Attempts were also made to correlate TEM images with STIM to identify SFs. The combination of STIM with SIMS aimed to observe SFs' connection with chemical variations, yet SFs were not discernible through STIM. However, STIM showed a better thickness variation contrast compared to TEM.

7 Chapter 7: Future work

The effects of ion beam incidence angle on transmission efficiency were discussed in state of the art section 1. Thus, the variation in transmitted ion channelling efficiencies by changing the incident beam angle within a grain is a subject that can be further investigated. In this regard we performed experiments at room and Cryo temperature (roughly 130°K) to investigate the variation in transmission ion channelling efficiency. The experimental results are then compared to ion channelling maps predicted by BCA simulations.

7.1 Preliminary results

The sample is the 50 nm thick freestanding Au membrane used in Chapter 4. The sample stage tilt in npSCOPE is available based on the movement of the cradle, which is located in the chamber. The cradle provides the tilt motion on one axis which is driven by the tilt drive assembly with a range of travel of -5° to +54 ° position. Therefore, we could tilt the stage by two experiments, from +5° to -4° with approximately 1° step and from 0 to +36° with about 2.5° steps. The primary beam energy was 30 keV, and the beam current fluctuated between 0.235 -0.125 pA. The He gas pressure was adjusted to 1.00×10^{-6} torr. The remaining parameters were the same as for the STIM imaging conditions mentioned before.

The Binary Collision Approximation (BCA) data has calculated the transmission yields on a rectilinear (tensor product) 46x46 grid within an x and y coordinates. Also, the normal surface vector and the x direction, both given in the ordinate system connected with the crystal axes ([100], [010], [001]), are calculated for the individual points. The BCA simulations were performed through a research collaboration with Prof. Gerhard Hobler of TU Wien.

STIM imaging acquired on each tilt position to examine the channelling contrast change with varying incident beam angles. Therefore, we obtained some primarily results on contrast variations caused by changes in the beam incidence angle at room temperature (300°K), depicted in Figure 7.1. For this purpose, the sample was tilted from -0.7° (reference) to 45°.

Several intriguing observations were observed within the grains as the contrast changed with varying beam angle incidence. For instance, in Figure 7.1(a, b), the twin band exhibited alternating dark and bright contrast within a ~5-degree shift in incident beam angle,

highlighted in a yellow rectangle. In Figure 7.1 (a, and c), the orange circle illustrates how changes in contrast can obscure the twin band that was initially observable. Furthermore, one twin band became visible at only a specific incident beam angle, as indicated by the red oval in Figure 7.1 (a). Red square within the Figure 7.1 (c) showed adjustments in the incident beam angle revealed that the grain actually comprised several smaller grains. Another noteworthy observation is the presence of a twin band in Figure 7.1 (d) within the red square, positioned halfway within the grain. The twin bands located within the red square in Figure 7.1 (c) exhibits better resolution when compared to Figure 7.1(a). The line profile shown in Figure 7.2. The better resolution may be because of the twin band's orientation, which aligns with the beam in a way that perfectly fits its inherent characteristic of appearing wider than they actually are; thus, this angle appears to be the ideal angle for this particular surface plane.

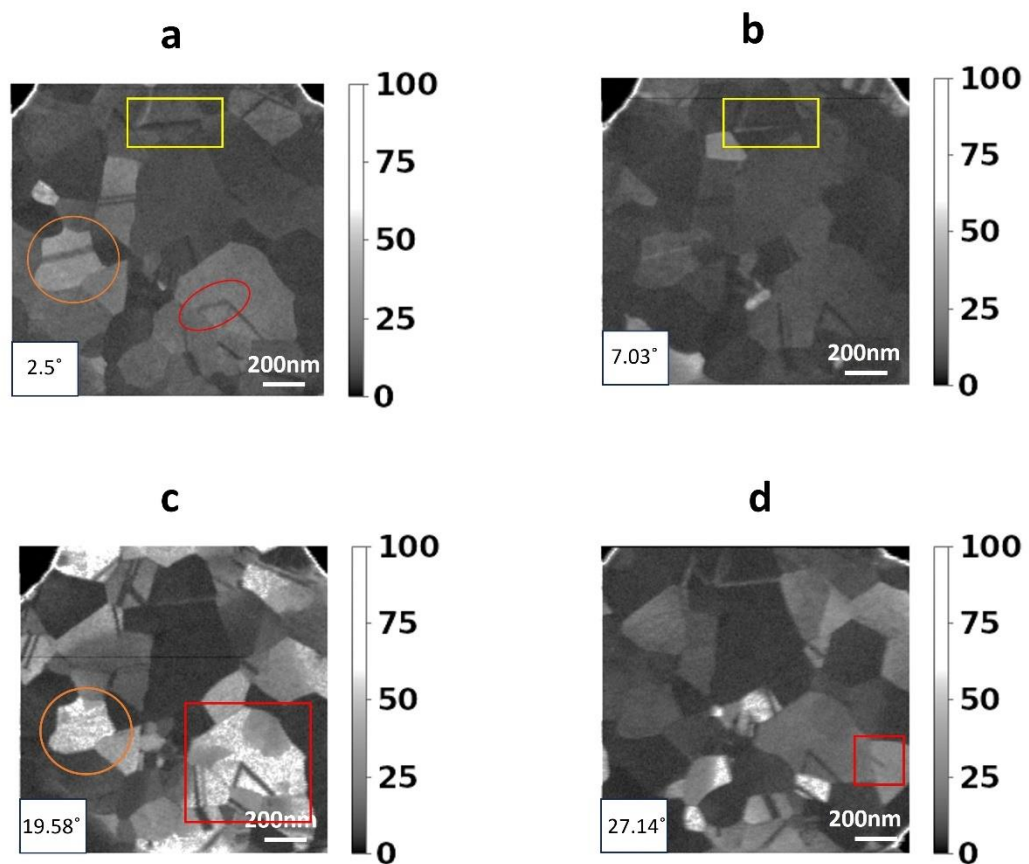


Figure 7.1: STIM images from 50 nm thick freestanding Au membrane, sample was tilted relative to reference angle of -0.7° to four different tilts: (a) 2.5° , (b) 7.03° , (c) 19.58° , (d) 27.14° tilt.

We must always consider that displayed tilt angles may not be entirely accurate. Since during the tilting process, the sample stage experiences a slight backward drift. Moreover, as the tilt angles exceed 27 degrees, the images obtained during acquisition display a lower resolution due to the drift that occurs as well as the stage's position's erratic movement.

Figure 7.2 presents the line profile analysis performed on the twin bands within the same ROI on the sample, albeit with a 30-degree tilt. This illustrates how the resolution of STIM imaging can vary with the incident beam angle, offering valuable insights for potential enhancements in STIM image resolution in the future.

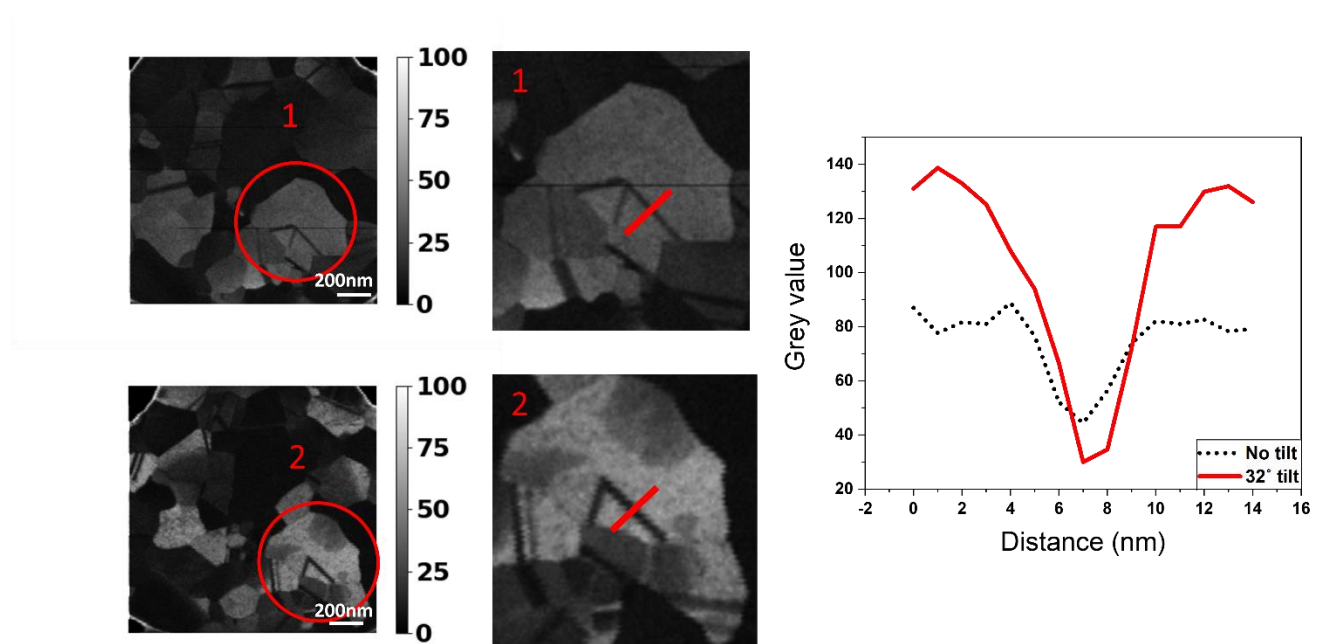


Figure 7.2: Line profile compares the measured featured size for the sample (1) with no tilt, and (2) 32° tilt. The STIM images on the left side display an area where the twin bands are present. Subsequently, we have cropped these images to emphasize the specific twin band chosen for the line profile, presenting it in a larger size.

To investigate the transmission intensity variation with temperature alteration, first we chose two distinct grains to test the intensity change in room temperature. The transmission intensity shows three peaks in Figure 7.3 (a) and two peaks in Figure 7.3 (b). The error bars in Figure 7.3 were derived from the 10% standard deviation of the stage's tilt magnitude for each dataset. Channelling theory excels at forecasting which channels will be active at a given energy and at sub-keV energies, this is still valid if the penetration depth is not too shallow[86]. Therefore, it's possible that this analysis could be utilized for a preliminary estimation of crystal orientations.

To accurately compute ion channelling across all crystal orientations and provide channelling maps that clearly illustrate the expected direction of channelling, we present a BCA simulation in parallel with these experiments, with the parameters similar to the experimental setup. The simulations provide the ion transmission yield as a function of crystal orientation, and the results are presented using stereographic projections. The channelling maps showed in Figure 7.3 are plots with stereographic projections. Using colour coding, these maps enable a qualitative understanding of the strength and width of channelling directions. In an experiment, a small subset of polar and azimuthal angles can be scanned to acquire a part of the channelling map[57], [189]. This information can correlate, channelling probability with the beam incident angle and the crystal orientation. Furthermore, this correlation could be helpful to estimate the crystal orientation of the grains in the STIM images using the beam incidence angle and the transmission intensity. Stereographic projections make it simple to choose effective 'non-channelling' ways for experiments or, alternatively, to locate broad channels for beneficial channelling applications.

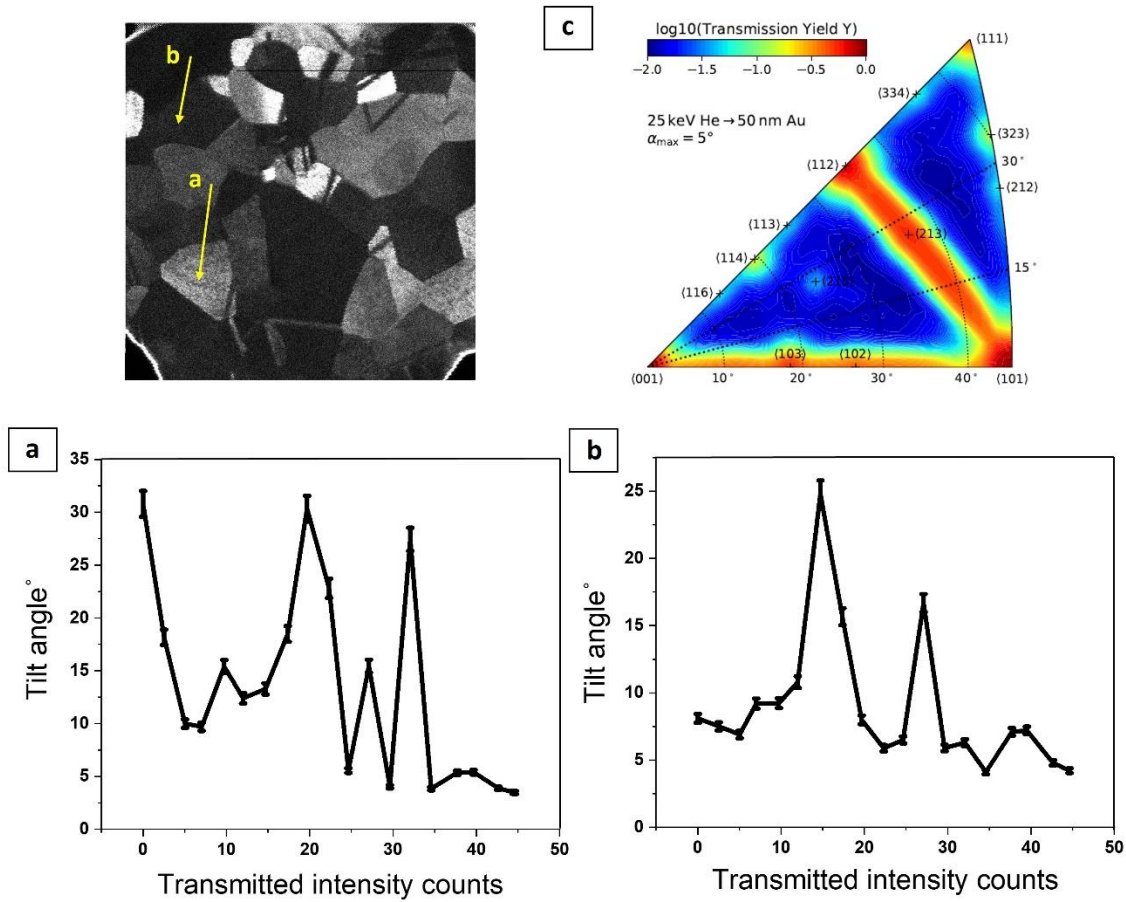


Figure 7.3: (a, b) Transmission intensity variations investigation in relation to the variation in beam incident angle in two separate grains indicated by arrows a, b in the STIM image. (c) stereographic projection of BCA simulation results for a sample temperature of 300 K.

Up to this point, all tilt experiments were performed at room temperature. However, it is crucial to consider the influence of the ion irradiation on sample, as it can cause significant heating of clusters when directed at a target. Ghader Zadeh et.al.[86] have investigated 5-15 nm gold nanoparticles using 30 keV He⁺ ion irradiation and found that collisions between the ions and target material can lead to significant heating of clusters due to energy deposition to electrons. However, under normal imaging conditions, clusters have time to cool between impacts, which means that channelling is unaffected. To delve deeper into this matter, we conducted the same set of experiments using the npSCOPE's cryo setup, which allowed us to lower the temperature of the sample (Figure 7.4). Here we present the transmission intensity for the 130 K samples for both experimental results and BCA simulations. We examined the transmission intensity of three distinct grains at progressively lower temperatures to achieve this goal. The error bars in Figure 7.4 were determined by

analysing the temperature fluctuations recorded during the measurements. We selected the pointed grains because of their high intensity. Grain 1 showed an intense increase in transmission ion intensity as the temperature decreased. Grain 2 and Grain 3 also increased in transmission intensity, but the slope was lower. The simulation findings are consistent with the experimental graph. The stereographic projection shows that at lower temperatures, larger regions are highlighted in red, indicating increased channelling and higher intensity.

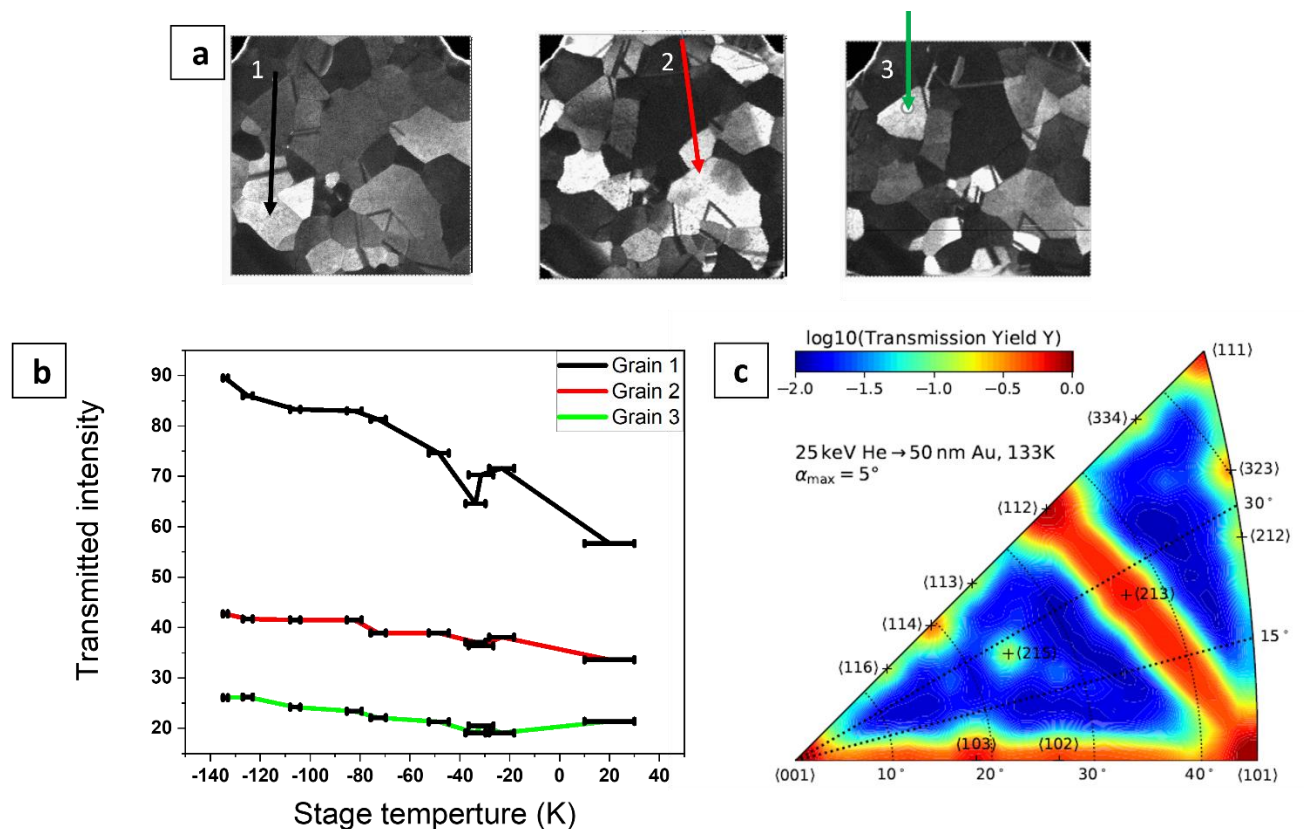


Figure 7.4: : (a) STIM images, (b) Transmission intensity variations investigation in relation to the variation in temperature in three separate grains in (a) 1, 2, 3. (c) stereographic projections of BCA simulation in 130 K.

7.2 Conclusions

We have seen the incident angle of the beam with the grains in the sample is a factor that can impact channelling contrast. The imaging of the tilted sample was also carried out at a temperature of 130 K, revealing that the behaviour of the grains is not uniform as their transmission intensity increases differently with decreasing temperature. With all the preliminary findings from STIM imaging regarding the impact of incident beam angle on transmission efficiency, there are still some further data needed. For example,

advancements in instrumentation (such as a double-tilt stage) and software development (including automated matching of intensity-angle correlations) are required to advance this research direction. Based on the BCA simulation results, we can aim to determine grain indexing by correlating STIM images with simulation outcomes.

8 Annex

8.1 Galileo prototype

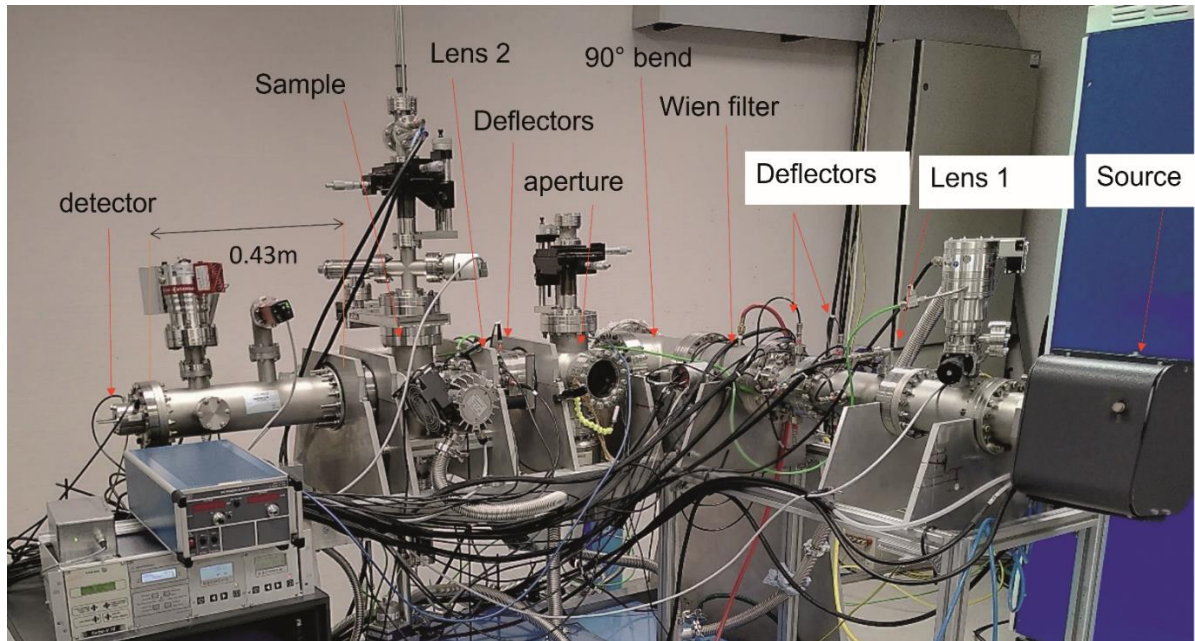


Figure 8.1: A photograph of the Galileo prototype scanning transmission helium ion microscope

8.2 SIMS analysis

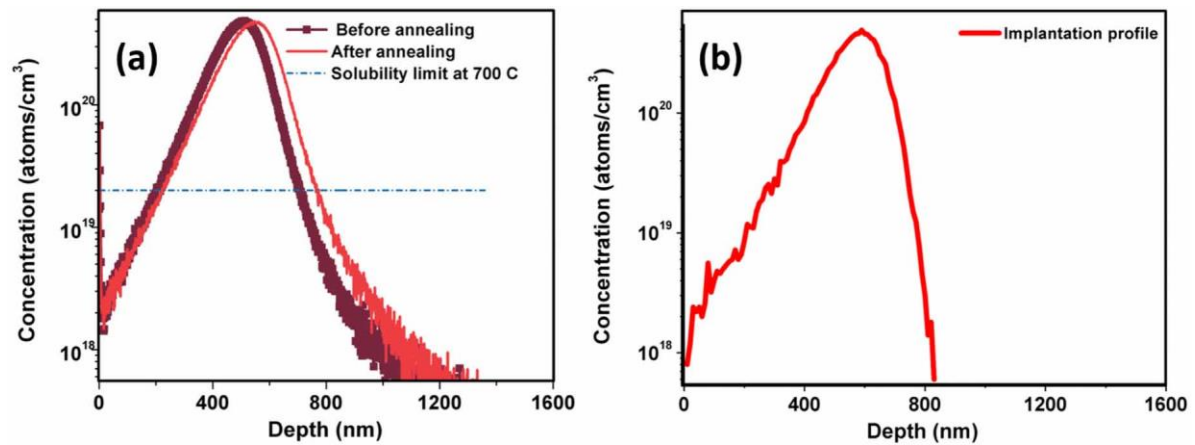


Figure 8.2: (a) SIMS depth profile of the silicon sample implanted with boron before and after heating to 700°C. (b) Implantation profile plotted from SRIM calculations. In (a), the dotted blue line indicates the boron solubility limit in silicon at 700°C, which is 2×10^{19} atoms cm^{-3} .

8.3 Schematic view of perovskite/crystalline-Si

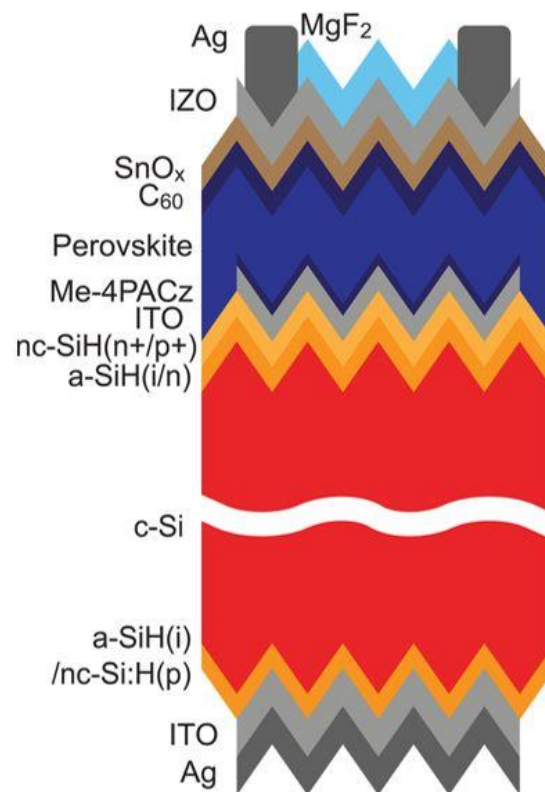


Figure 8.3: An illustrative representation of the tandem stack involving perovskite and crystalline silicon (c-Si).

8.4 QFLS and XPS

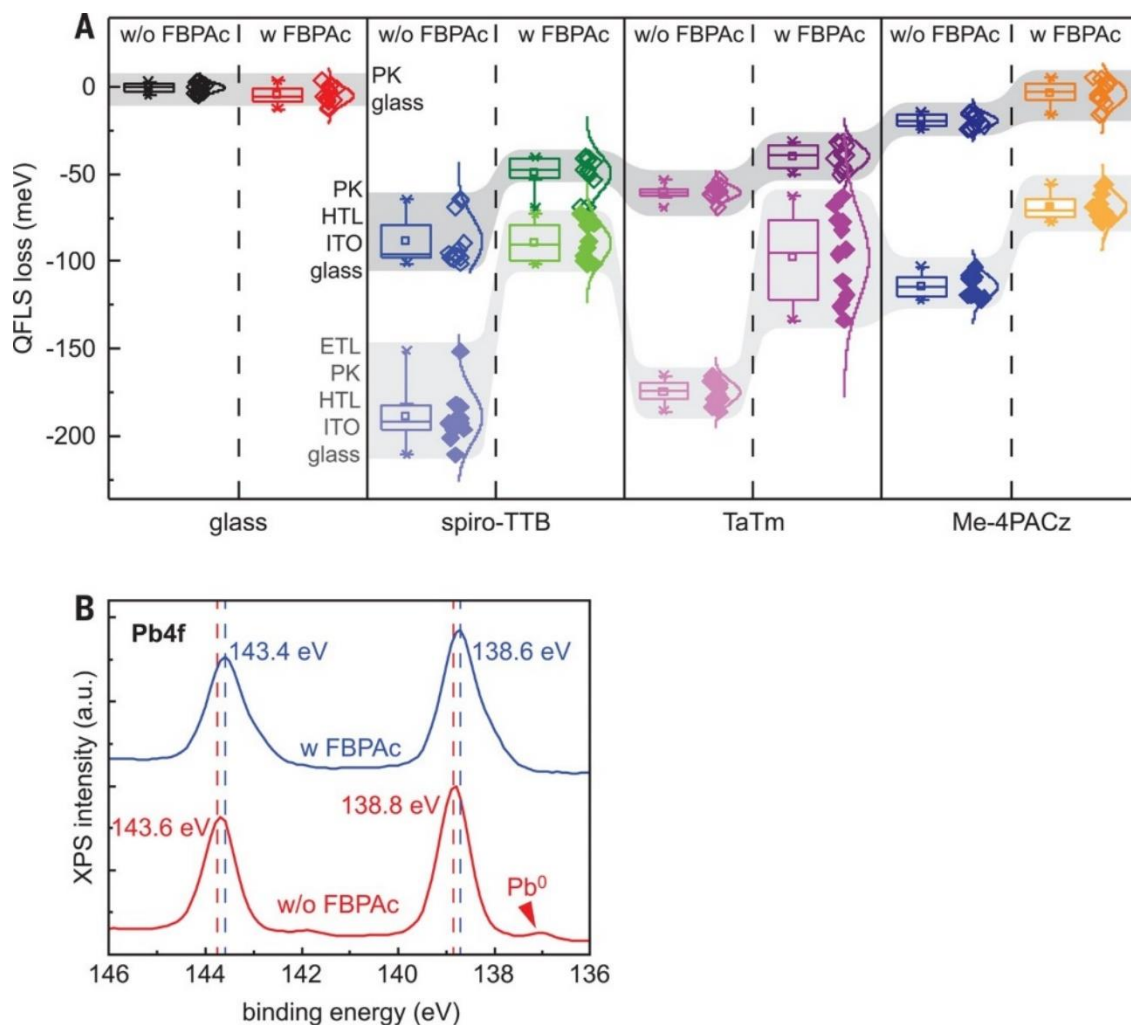


Figure 8.4: The comprehension of FBPAc results in a reduction of nonradiative recombination losses and an improvement in crystallographic properties. (A) The chart displays the QFLS of perovskite films, both with and without FBPAc, as deduced from photoluminescence quantum yield data. This comparison is relative to the glass/perovskite reference. The data points represented by hollow diamonds correspond to QFLS measurements of perovskite films deposited on various hole transport layers (HTLs), namely spiro-TTB, TaTm, and Me-4PACz. In contrast, the filled diamonds are associated with films positioned between one of these HTLs and a C₆₀ ETL. (B) Presented here are high-resolution XPS spectra of the Pb 4f orbital.

8.5 Current -voltage (J-V)

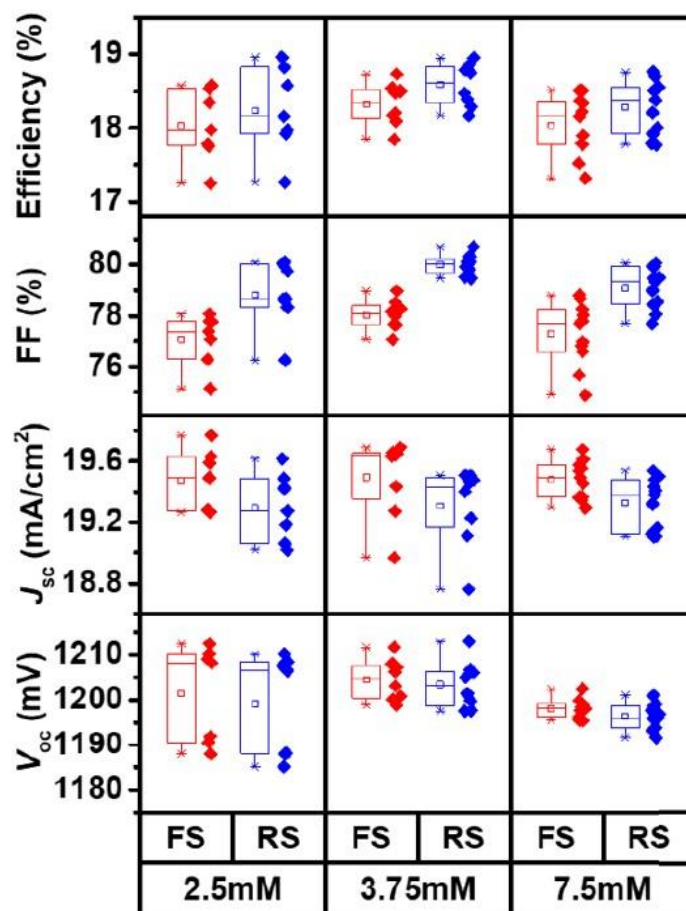


Figure 8.5: The impact of FBPAc concentration on the current-voltage (J-V) characteristics of perovskite single-junction cells was examined. The x-axis represents the molar concentration of FBPAc used during the spin-coating process of the organo-halide solution (specifically, 0.46M of FA⁺). Notably, the current-voltage parameters, including efficiency, fill factor (FF), photocurrent density (J_{sc}), and open-circuit voltage (V_{oc}), exhibited no significant statistical differences across the single-junction perovskite solar cells, regardless of the FBPAc concentration. This similarity can be predominantly attributed to the natural tendency of any unreacted excess FBPAc to self-aggregate, leading to the formation of clusters on the top surface of the perovskite thin films (as depicted in Figure 6.4(a)). It's important to note that the aperture area used for the J-V measurements was 0.25 cm².

8.6 Photocurrent map

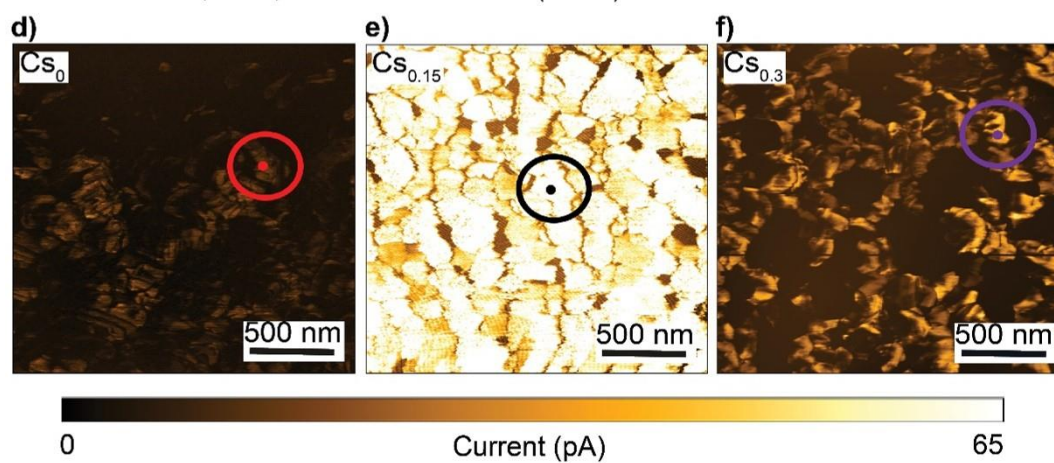


Figure 8.6: d-f) Photo-current maps performed at 1 sun under JSC conditions for the CsFA perovskite systems

8.7 C-AFM map

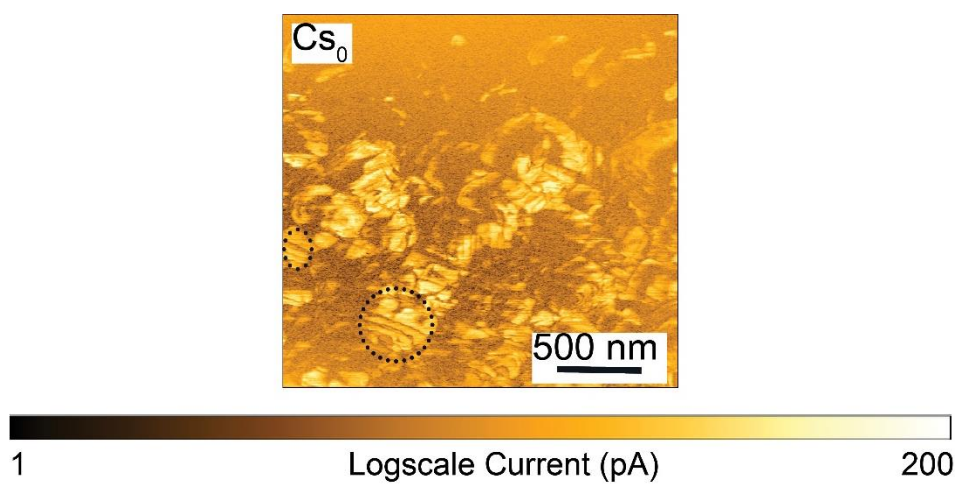


Figure 8.7: a log-scale representation of the C-AFM map for the FAPbI₃ film shown in Figure 8.6(d) to emphasize the terraced-edge surfaces, as indicated by the black circles.

8.8 Stability and performance

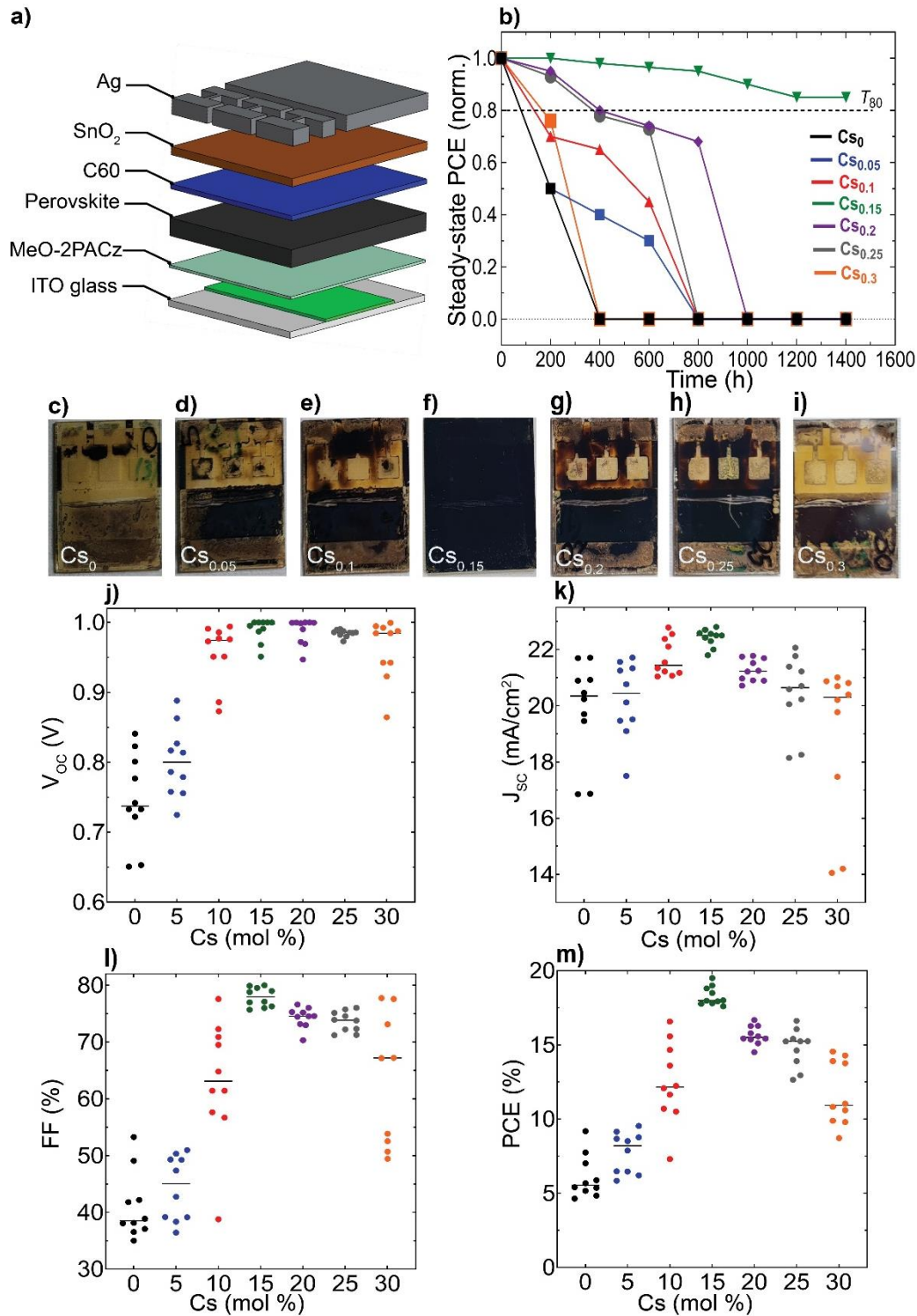


Figure 8.8: Stability and performance assessment of the perovskite devices: a) Depiction of the pin device stack structure. b) Progression of normalized steady-state PCE (averaged from 6 sub cells) for encapsulated PSCs, subjected to continuous simulated sunlight exposure at 35°C in an N_2 atmosphere. T_{80} represents the time it takes for a solar cell device to decrease to 80% of its initial efficiency. c-i) Images of the aged CsFA encapsulated perovskite devices, captured from the glass side after enduring 1400 hours of uninterrupted simulated sunlight exposure. Statistical distribution depicting the performance metrics of CsFA PSCs: j) Open-circuit voltage (V_{oc}), k) Short-circuit current density (J_{sc}), l) Fill factor (FF), and m) PCE. All current-voltage (J - V) data were collected under standard conditions, utilizing a simulated air mass (AM) 1.5G and 100 mW cm^{-2} of sunlight.

9 References

- [1] L.A. Giannuzzi and F.A. Stevens. "Introduction to focused ion beams: instrumentation, theory, techniques and practice." *Springer Science & Business Media*, 2004.
- [2] H. D. Wanzenboeck *et al.*, "FIB-TEM characterization of locally restricted implantation damage," *Mater. Res. Soc. Symp. - Proc.*, vol. 738, pp. 57–62, 2003, doi: 10.1557/proc-738-g7.14.
- [3] S. Rubanov and P. R. Munroe, "FIB-induced damage in silicon," *J. Microsc.*, vol. 214, no. 3, pp. 213–221, 2004, doi: 10.1111/j.0022-2720.2004.01327.x.
- [4] K. A. Unocic, M. J. Mills, and G. S. Daehn, "Challenges in preparing aluminum alloys for grain boundary characterization," *Microsc. Microanal.*, vol. 14, no. SUPPL. 2, pp. 556–557, 2008, doi: 10.1017/S1431927608082305.
- [5] R. P. Babu, S. Irukuvarghula, A. Harte, and M. Preuss, "Nature of gallium focused ion beam induced phase transformation in 316L austenitic stainless steel," *Acta Mater.*, vol. 120, pp. 391–402, 2016, doi: 10.1016/j.actamat.2016.08.008.
- [6] J. R. Michael, "Focused ion beam induced microstructural alterations: Texture development, grain growth, and intermetallic formation," *Microsc. Microanal.*, vol. 17, no. 3, pp. 386–397, 2011, doi: 10.1017/S1431927611000171.
- [7] K. A. Unocic, M. J. Mills, and G. S. Daehn, "Effect of gallium focused ion beam milling on preparation of aluminium thin foils," *J. Microsc.*, vol. 240, no. 3, pp. 227–238, 2010, doi: 10.1111/j.1365-2818.2010.03401.x.
- [8] A. Stanishevsky *et al.*, "Testing new chemistries for mask repair with focused ion beam gas assisted etching," *J. Vac. Sci. Technol. B Microelectron. Nanom. Struct.*, vol. 21, no. 6, p. 3067, 2003, doi: 10.1116/1.1624253.
- [9] D. H. Anjum, I. A. Qattan, S. Patole, E. M. Diallo, N. Wei, and H. Heidebreder, "Nano-characterization of silicon-based multilayers using the technique of STEM-EELS spectrum-imaging," *Mater. Today Commun.*, vol. 25, no. May, p. 101209, 2020, doi: 10.1016/j.mtcomm.2020.101209.
- [10] N. Kumar, R. Kumar, S. Kumar, and S. K. Chakarvarti, "Tailoring the properties of copper nanowires by ion beam irradiation," *Radiat. Phys. Chem.*, vol. 119, pp. 44–50, 2016, doi: 10.1016/j.radphyschem.2015.09.010.
- [11] C.S. Kim, *et al.*, "Focused-helium-ion-beam blow forming of nanostructures: radiation damage and nanofabrication," *Nanotechnology*, 31(4), p.045302, *Mater*, 2019.
- [12] M. Moon, S. H. Lee, J. Sun, K. H. Oh, A. Vaziri, and J. W. Hutchinson, "Wrinkled hard skins on polymers created by focused ion beam," *PNAS.*, vol. 104, no. 4, 2007, [Online]. Available: www.pnas.org/cgi/doi/10.1073/pnas.0610654104.
- [13] R. Lontas *et al.*, "Effects of helium implantation on the tensile properties and microstructure of Ni73P27 metallic glass nanostructures," *Nano Lett.*, vol. 14, no. 9, pp. 5176–5183, 2014, doi: 10.1021/nl502074d.
- [14] L. Y. Shang, D. Zhang, and B. Y. Liu, "Influence of Cu ion implantation on the microstructure and cathodoluminescence of ZnS nanostructures," *Phys. E Low-Dimensional Syst. Nanostructures*, vol. 81, pp. 315–319, 2016, doi: 10.1016/j.physe.2016.03.042.
- [15] C. Ronning *et al.*, "Tailoring the properties of semiconductor nanowires using ion beams," *Phys. Status Solidi Basic Res.*, vol. 247, no. 10, pp. 2329–2337, 2010, doi: 10.1002/pssb.201046192.
- [16] S. Hoffmann and J. Michler, "Axial p-n junctions realized in Silicon nanowires by ion implantation," *EMPA Act.*, no. 2009-2010 EMPA ACTIVITIES, p. 15, 2009.
- [17] W. Möller, A. Johannes, and C. Ronning, "Shaping and compositional modification of zinc oxide nanowires under energetic manganese ion irradiation," *Nanotechnology*, vol. 27, no. 17, p. 0, 2016,

doi: 10.1088/0957-4484/27/17/175301.

- [18] P. Willke *et al.*, "Doping of Graphene by Low-Energy Ion Beam Implantation: Structural, Electronic, and Transport Properties," *Nano Lett.*, vol. 15, no. 8, pp. 5110–5115, 2015, doi: 10.1021/acs.nanolett.5b01280.
- [19] R. Flatabo *et al.*, "Exploring proximity effects and large depth of field in helium ion beam lithography: large-area dense patterns and tilted surface exposure." *Nanotechnology* 29.27 (2018): 275301.
- [20] A. Johannes, S. Noack, W. Wesch, M. Glaser, A. Lugstein, and C. Ronning, "Anomalous Plastic Deformation and Sputtering of Ion Irradiated Silicon Nanowires," *Nano Lett.*, vol. 15, no. 6, pp. 3800–3807, 2015, doi: 10.1021/acs.nanolett.5b00431.
- [21] M. S. Ding *et al.*, "Radiation-Induced Helium Nanobubbles Enhance Ductility in Submicron-Sized Single-Crystalline Copper," *Nano Lett.*, vol. 16, no. 7, pp. 4118–4124, 2016, doi: 10.1021/acs.nanolett.6b00864.
- [22] A. Janse Van Vuuren, V. A. Skuratov, V. V. Uglov, J. H. Neethling, and S. V. Zlotski, "Radiation tolerance of nanostructured ZrN coatings against swift heavy ion irradiation," *J. Nucl. Mater.*, vol. 442, no. 1–3, pp. 507–511, 2013, doi: 10.1016/j.jnucmat.2013.02.047.
- [23] Y. J. Jung, Y. Homma, R. Vajtai, Y. Kobayashi, T. Ogino, and P. M. Ajayan, "Straightening suspended single walled carbon nanotubes by ion irradiation," *Nano Lett.*, vol. 4, no. 6, pp. 1109–1113, 2004, doi: 10.1021/nl049550b.
- [24] A. P. Robinson, G. Burnell, S. L. Sahonta, and J. MacManus-Driscoll, "Perfectly ordered, free-standing nanowire arrays with controllable geometry," *Adv. Eng. Mater.*, vol. 11, no. 11, pp. 907–911, 2009, doi: 10.1002/adem.200900150.
- [25] C. S. Kim *et al.*, "Focused-helium-ion-beam blow forming of nanostructures: Radiation damage and nanofabrication," *Nanotechnology*, vol. 31, no. 4, 2020, doi: 10.1088/1361-6528/ab4a65.
- [26] A. Kashinath and M. J. Demkowicz, "A predictive interatomic potential for He in Cu and Nb," *Model. Simul. Mater. Sci. Eng.*, vol. 19, no. 3, 2011, doi: 10.1088/0965-0393/19/3/035007.
- [27] M. G. Stanford *et al.*, "In Situ Mitigation of Subsurface and Peripheral Focused Ion Beam Damage via Simultaneous Pulsed Laser Heating," *Small*, vol. 12, no. 13, pp. 1779–1787, 2016, doi: 10.1002/sml.201503680.
- [28] V. Raineri, P. G. Fallica, G. Percolla, A. Battaglia, M. Barbagallo, and S. U. Campisano, "Gettering of metals by voids in silicon," *J. Appl. Phys.*, vol. 78, no. 6, pp. 3727–3735, 1995, doi: 10.1063/1.359953.
- [29] R. Livengood, S. Tan, Y. Greenzweig, J. Notte, and S. McVey, "Subsurface damage from helium ions as a function of dose, beam energy, and dose rate," *J. Vac. Sci. Technol. B Microelectron. Nanom. Struct.*, vol. 27, no. 6, p. 3244, 2009, doi: 10.1116/1.3237101.
- [30] D. Fox, Y. Chen, C. C. Faulkner, and H. Zhang, "Nano-structuring, surface and bulk modification with a focused helium ion beam," *Beilstein J. Nanotechnol.*, vol. 3, no. 1, pp. 579–585, 2012, doi: 10.3762/bjnano.3.67.
- [31] R. Li *et al.*, "Study of damage generation induced by focused helium ion beam in silicon," *J. Vac. Sci. Technol. B*, vol. 37, no. 3, p. 031804, 2019, doi: 10.1116/1.5096908.
- [32] C. M. Gonzalez *et al.*, "Focused helium and neon ion beam induced etching for advanced extreme ultraviolet lithography mask repair," *J. Vac. Sci. Technol. B, Nanotechnol. Microelectron. Mater. Process. Meas. Phenom.*, vol. 32, no. 2, p. 021602, 2014, doi: 10.1116/1.4868027.
- [33] S. Hang, Z. Moktadir, and H. Mizuta, "Raman study of damage extent in graphene nanostructures carved by high energy helium ion beam," *Carbon N. Y.*, vol. 72, pp. 233–241, 2014, doi: 10.1016/j.carbon.2014.01.071.
- [34] D. C. Joy, "SPRINGER BRIEFS IN MATERIALS Helium Ion Microscopy Principles and Applications." *Springer New York Heidelberg Dordrecht London.*, ISBN 978-1-4614-8660-2, 2013, DOI 10.1007/978-1-

- [35] B. W. Ward, J. A. Notte, and N. P. Economou, "Helium ion microscope: A new tool for nanoscale microscopy and metrology," *J. Vac. Sci. Technol. B Microelectron. Nanom. Struct.*, vol. 24, no. 6, p. 2871, 2006, doi: 10.1116/1.2357967.
- [36] C. P. Sealy, M. R. Castell, and P. R. Wilshaw, "Mechanism for secondary electron dopant contrast in the SEM," *J. Electron Microsc. (Tokyo)*, vol. 49, no. 2, pp. 311–321, 2000, doi: 10.1093/oxfordjournals.jmicro.a023811.
- [37] A. K. W. Chee, "Principles of High-Resolution Dopant Profiling in the Scanning Helium Ion Microscope, Image Widths, and Surface Band Bending," *IEEE Trans. Electron Devices*, vol. 66, no. 11, pp. 4883–4887, 2019, doi: 10.1109/TED.2019.2940562.
- [38] M. Buzzo, M. Ciappa, M. Stangoni, and W. Fichtner, "Two-dimensional dopant profiling and imaging of 4H silicon carbide devices by secondary electron potential contrast," *Microelectron. Reliab.*, vol. 45, no. 9–11, pp. 1499–1504, 2005, doi: 10.1016/j.microrel.2005.07.069.
- [39] M. El-Gomati, "Why is it possible to detect doped regions of semiconductors in low voltage SEM: a review and update," *Surf. Interface Anal.* 2005; 37: 901–911, doi: 10.1002/sia.2108.
- [40] R. Turan, D. D. Perovic, and D. C. Houghton, "Mapping electrically active dopant profiles by field-emission scanning electron microscopy," *Appl. Phys. Lett.*, vol. 69, no. 11, pp. 1593–1595, 1996, doi: 10.1063/1.117041.
- [41] L. Frank, M. Hovorka, M. M. El-Gomati, I. Müllerová, F. Mika, and E. Mikmeková, "Acquisition of the dopant contrast in semiconductors with slow electrons," *J. Electron Spectros. Relat. Phenomena*, vol. 241, no. July 2018, pp. 0–1, 2020, doi: 10.1016/j.elspec.2019.03.004.
- [42] A. E. Michel, W. Rausch, and P. A. Ronsheim, "Implantation damage and the anomalous transient diffusion of ion-implanted boron," *Appl. Phys. Lett.*, vol. 51, no. 7, pp. 487–489, 1987, doi: 10.1063/1.98375.
- [43] L. A. Giannuzzi and J. R. Michael, "Ion Channeling vs. Electron Channeling Image Contrast," *Microsc. Microanal.*, vol. 18, no. Suppl 2, pp. 694–695, 2012, doi: 10.1017/S1431927612005326.
- [44] P. J. C. King, M. B. H. Breese, P. J. M. Smulders, P. R. Wilshaw, and G. W. Grime, "Defect imaging and channeling studies using channeling scanning transmission ion microscopy," *Nucl. Instruments Methods Phys. Res. Sect. B Beam Interact. with Mater. Atoms*, vol. 118, no. 1–4, pp. 426–430, 1996, doi: 10.1016/0168-583X(95)01091-2.
- [45] W. H. Escovitz, T. R. Fox, and R. Levi Setti, "Scanning transmission ion microscope with a field ion source," *Proc. Natl. Acad. Sci. U. S. A.*, vol. 72, no. 5, pp. 1826–1828, 1975, doi: 10.1073/pnas.72.5.1826.
- [46] E. Serralta *et al.*, "Scanning transmission imaging in the helium ion microscope using a microchannel plate with a delay line detector," *Beilstein J. Nanotechnol.*, vol. 11, pp. 1854–1864, 2020, doi: 10.3762/BJNANO.11.167.
- [47] Linhard, "Motion As Influenced of Swift Charged By Strings," *Phys. Lett.*, vol. 12, no. 2, pp. 126–128, 1964.
- [48] G. Hlawacek and A. Götzhäuser, *Helium Ion Microscopy*. Basel, Switzerland: Springer Nature, 2016.
- [49] R. Holeňák, S. Lohmann, and D. Primetzhofer, "Contrast modes in a 3D ion transmission approach at keV energies," *Ultramicroscopy*, vol. 217, no. June, pp. 0–5, 2020, doi: 10.1016/j.ultramic.2020.113051.
- [50] S. Lohmann and D. Primetzhofer, "Disparate Energy Scaling of Trajectory-Dependent Electronic Excitations for Slow Protons and He Ions," *Phys. Rev. Lett.*, vol. 124, no. 9, p. 96601, 2020, doi: 10.1103/PhysRevLett.124.096601.
- [51] G. A. Dissanaikie, "CX. A study of charge exchange by helium ions in metals," *London, Edinburgh, Dublin Philos. Mag. J. Sci.*, vol. 44, no. 357, pp. 1051–1063, 1953, doi: 10.1080/14786441008520363.

- [52] P. Sigmund, "Six decades of atomic collisions in solids," *Nucl. Instruments Methods Phys. Res. Sect. B Beam Interact. with Mater. Atoms*, vol. 406, pp. 391–412, 2017, doi: 10.1016/j.nimb.2016.12.004.
- [53] J. Lindhard, "Influence of Crystal Lattice on Motion of Energetic Charged Particles," *Mat. Fys. Medd.*, vol. 34, pp. 1–64, 1965.
- [54] M. T. Robinson and O. S. Oen, "Computer studies of the slowing down of energetic atoms in crystals," *Phys. Rev.*, vol. 132, no. 6, pp. 2385–2398, 1963, doi: 10.1103/PhysRev.132.2385.
- [55] J. U. Andersen, "Notes on Channeling," University of Aarhus (1986).
- [56] J. A. Davies, "The Channeling Phenomenon- and Some of Its Applications," *Phys. Scr.*, vol. 28, no. 3, pp. 294–302, 1983, doi: 10.1088/0031-8949/28/3/006.
- [57] C. J. Andreen and R. L. Hines, "Critical angles for channeling of H⁺, D⁺ and He⁺ ions in single crystal gold films in the energy interval 1-17 keV," *Phys. Lett. A*, vol. 24, no. 2, pp. 118–119, 1967, doi: 10.1016/0375-9601(67)90512-9.
- [58] R. S. Nelson and M. W. Thompson, "The penetration of energetic ions through the open channels in a crystal lattice," *Philos. Mag.*, vol. 8, no. 94, pp. 1677–1690, 1963, doi: 10.1080/14786436308207330.
- [59] P. Sigmund, "LSS and the Integral Equations of Transport Theory," *Phys. Scr.*, vol. 28, no. 3, pp. 257–267, 1983, doi: 10.1088/0031-8949/28/3/001.
- [60] C. Lehmann and G. Leibfried, "Long-range channeling effects in irradiated crystals," *J. Appl. Phys.*, vol. 34, no. 9, pp. 2821–2836, 1963, doi: 10.1063/1.1729817.
- [61] G. Hobler, "Critical angles and low-energy limits to ion channeling in silicon," *Radiat. Eff. Defects Solids*, vol. 139, no. 1, pp. 21–85, 1996, doi: 10.1080/10420159608212927.
- [62] V. G. K. Reddi and J. D. Sansbury, "Channeling and dechanneling of ion-implanted phosphorus in silicon," *J. Appl. Phys.*, vol. 44, no. 7, pp. 2951–2963, 1973, doi: 10.1063/1.1662689.
- [63] H. Nishi, T. Inada, T. Sakurai, T. Kaneda, T. Hisatsugu, and T. Furuya, "Uniform doping of channeled-ion implantation," *J. Appl. Phys.*, vol. 49, no. 2, pp. 608–613, 1978, doi: 10.1063/1.324687.
- [64] J. F. Gibbons, "Ion Implantation in Semiconductors—Part I Range Distribution Theory and Experiments," *Proc. IEEE*, vol. 56, no. 3, pp. 295–319, 1968, doi: 10.1109/PROC.1968.6273.
- [65] S.T. Picraux et al., "Channeling studies in diamond-type lattices," *Physical Review*, 180(3), p.873, 1969.
- [66] B. Domeij, "Crystal lattice effects in the emission of charged particles from monocrystalline sources," *Nucl. Instruments Methods*, vol. 38, no. C, pp. 207–209, 1965, doi: 10.1016/0029-554X(65)90139-4.
- [67] E. Bøgh, J. A. Davies, and K. O. Nielsen, "Experimental evidence for the extinction of (p, γ) yields in single crystals," *Phys. Lett.*, vol. 12, no. 2, pp. 129–130, 1964, doi: 10.1016/0031-9163(64)91134-5.
- [68] E. Bøgh and E. Uggerhøj, "Experimental investigation of orientation dependence of rutherford scattering yield in single crystals," *Nuclear Instruments and methods.*, vol. 38, pp. 216–220, 1965.
- [69] L. T. Chadderton and F. H. Eisen, "On the transmission of energetic protons through very thin crystals," *Philosophical Magazine.*, vol. 8086, no. June, 2016, doi: 10.1080/14786436908228546.
- [70] J. F. Ziegler and R. F. Lever, "Channeling of ions near the silicon 001 axis," *Appl. Phys. Lett.*, vol. 358, pp. 4–7, 1985, doi: 10.1063/1.95630.
- [71] J. Sillanpää, K. Nordlund, and J. Keinonen, "Electronic stopping of Si from a three-dimensional charge distribution," *PHYSICAL REVIEW B.*, vol. 62, no. 5, pp. 3109–3116, 2000.
- [72] K. Nordlund, "Molecular dynamics simulation of ion ranges in the 1-100 keV energy range," *COMPUTATIONAL MATERIALS SCIENCE.*, vol. 0256, no. 94, 1995.
- [73] R. Smith, B. King, and K. Beardmore, "Incorporating Plasma Science and Plasma Technology Molecular dynamics simulation of 0.1 – 2 keV ion bombardment of Ni { 100 }," *Radiation Effects and Defects in*

- Solids.*, vol. 141, pp. 425–451, 1997, doi: 10.1080/10420159708211586.
- [74] K. M. Beardmore, “Direct simulation of ion-beam-induced stressing and amorphization of silicon,” *PHYSICAL REVIEW.*, vol. 60, no. 18, pp. 610–616, 1999.
 - [75] G. Hobler and G. Betz, “On the useful range of application of molecular dynamics simulations in the recoil interaction approximation,” *Nuclear Instruments and Methods in Physics.*, vol. 180, pp. 203–208, 2001.
 - [76] A. R. Hall, “In situ thickness assessment during ion milling of a free-standing membrane using transmission helium ion microscopy,” *Microsc. Microanal.*, vol. 19, no. 3, pp. 740–744, 2013, doi: 10.1017/S1431927613000500.
 - [77] V. P. Adiga, B. Ilic, R. A. Barton, I. Wilson-Rae, H. G. Craighead, and J. M. Parpia, “Approaching intrinsic performance in ultra-thin silicon nitride drum resonators,” *J. Appl. Phys.*, vol. 112, no. 6, pp. 0–6, 2012, doi: 10.1063/1.4754576.
 - [78] M. Wanunu, T. Dadoosh, V. Ray, J. Jin, L. McReynolds, and M. Drndić, “Rapid electronic detection of probe-specific microRNAs using thin nanopore sensors,” *Nat. Nanotechnol.*, vol. 5, no. 11, pp. 807–814, 2010, doi: 10.1038/nnano.2010.202.
 - [79] N. Yu, K. B. Ma, and W. K. Chu, “Channeling simulation on YBa₂Cu₃O₇,” *Nucl. Inst. Methods Phys. Res. B*, vol. 59–60, no. PART 2, pp. 1409–1414, 1991, doi: 10.1016/0168-583X(91)95842-2.
 - [80] J. H. Barrett, “Methods of channeling simulation,” *Nucl. Inst. Methods Phys. Res. B*, vol. 44, no. 3, pp. 367–372, 1990, doi: 10.1016/0168-583X(90)90652-B.
 - [81] R. E. Franklin, E. C. G. Kirk, J. R. A. Cleaver, and H. Ahmed, “Channelling ion image contrast and sputtering in gold specimens observed in a high-resolution scanning ion microscope,” *J. Mater. Sci. Lett.*, vol. 7, no. 1, pp. 39–41, 1988, doi: 10.1007/BF01729909.
 - [82] V. Veligura, G. Hlawacek, R. Van Gastel, H. J. W. Zandvliet, and B. Poelsema, “Channeling in helium ion microscopy: Mapping of crystal orientation,” *Beilstein J. Nanotechnol.*, vol. 3, no. 1, pp. 501–506, 2012, doi: 10.3762/bjnano.3.57.
 - [83] G. Hlawacek *et al.*, “Imaging ultra thin layers with helium ion microscopy: Utilizing the channeling contrast mechanism,” *Beilstein J. Nanotechnol.*, vol. 3, no. 1, pp. 507–512, 2012, doi: 10.3762/bjnano.3.58.
 - [84] C. Langlois *et al.*, “Crystal orientation mapping via ion channeling: An alternative to EBSD,” *Ultramicroscopy*, vol. 157, pp. 65–72, 2015, doi: 10.1016/j.ultramic.2015.05.023.
 - [85] G. Hlawacek, M. Jankowski, H. Wormeester, R. Van Gastel, H. J. W. Zandvliet, and B. Poelsema, “Ultramicroscopy Visualization of steps and surface reconstructions in Helium Ion Microscopy with atomic precision,” *Ultramicroscopy*, vol. 162, pp. 17–24, 2016, doi: 10.1016/j.ultramic.2015.11.009.
 - [86] S. Ghaderzadeh, M. Ghorbani-asl, and S. Kretschmer, “Channeling effects in gold nanoclusters under He ion irradiation : insights from molecular dynamics simulations,” *Nanotechnology* 31, no. 3 (2019), pp. 17–31. 2020. doi: 10.1088/1361-6528/ab4847.
 - [87] L. P. Zheng, Z. Y. Zhu, Y. Li, D. Z. Zhu, and H. H. Xia, “Ion mass dependence for low energy channeling in single-wall nanotubes,” *Nucl. Instruments Methods Phys. Res. Sect. B Beam Interact. with Mater. Atoms*, vol. 266, no. 5, pp. 849–852, 2008, doi: 10.1016/j.nimb.2008.01.001.
 - [88] W. Takeuchi, “Evaluation of theoretical critical angle including mass effects for channeling by computer simulation,” *Nucl. Instruments Methods Phys. Res. Sect. B Beam Interact. with Mater. Atoms*, vol. 269, no. 12, pp. 1355–1360, 2011, doi: 10.1016/j.nimb.2011.03.013.
 - [89] E. Serralta *et al.*, “Scanning transmission imaging in the helium ion microscope using a microchannel plate with a delay line detector,” *Beilstein.*, pp. 1854–1864, 1854, doi: 10.3762/bjnano.11.167.
 - [90] C. L. Fontana *et al.*, “Stopping power measurements with the Time-of-Flight (ToF) technique,” *Nucl. Instruments Methods Phys. Res. Sect. B Beam Interact. with Mater. Atoms*, vol. 366, pp. 104–116, 2016,

doi: 10.1016/j.nimb.2015.10.048.

- [91] Y. Zhang and W. J. Weber, "Response of materials to single ion events," *Nucl. Instruments Methods Phys. Res. Sect. B Beam Interact. with Mater. Atoms*, vol. 267, no. 8–9, pp. 1705–1712, 2009, doi: 10.1016/j.nimb.2009.01.104.
- [92] W. J. Weber, D. M. Duffy, L. Thomé, and Y. Zhang, "The role of electronic energy loss in ion beam modification of materials," *Curr. Opin. Solid State Mater. Sci.*, vol. 19, no. 1, pp. 1–11, 2015, doi: 10.1016/j.cossms.2014.09.003.
- [93] C. H. Chen *et al.*, "Irradiation-induced microstructural change in helium-implanted single crystal and nano-engineered SiC," *J. Nucl. Mater.*, vol. 453, no. 1–3, pp. 280–286, 2014, doi: 10.1016/j.jnucmat.2014.07.020.
- [94] Y. Zhang, A. Debelle, A. Boulle, P. Kluth, and F. Tuomisto, "Advanced techniques for characterization of ion beam modified materials," *Curr. Opin. Solid State Mater. Sci.*, vol. 19, no. 1, pp. 19–28, 2015, doi: 10.1016/j.cossms.2014.09.007.
- [95] Y. Zhang and W. J. Weber, "Validity of Bragg's rule for heavy-ion stopping in silicon carbide," *Phys. Rev. B - Condens. Matter Mater. Phys.*, vol. 68, no. 23, pp. 2353171–2353177, 2003, doi: 10.1103/PhysRevB.68.235317.
- [96] Y. Zhang, W. J. Weber, and C. M. Wang, "Electronic stopping powers in silicon carbide," *Phys. Rev. B - Condens. Matter Mater. Phys.*, vol. 69, no. 20, pp. 1–9, 2004, doi: 10.1103/PhysRevB.69.205201.
- [97] C. Angulo, T. Delbar, J.-S. Graulich, and P. Leleux, "Stopping power measurements: Implications in nuclear astrophysics," *American Institute of Physics.*, vol. 381, pp. 381–384, 2008, doi: 10.1063/1.1301826.
- [98] N. V. Kuznetsov, R. A. Nymmik, and N. M. Sobolevsky, "Estimates of radiation effect for a spacecraft on the Earth-Mars-Earth route," *Adv. Sp. Res.*, vol. 30, no. 4, pp. 985–988, 2002, doi: 10.1016/S0273-1177(02)00163-1.
- [99] B. Schaffner and E. Pedroni, "The precision of proton range calculations in proton radiotherapy treatment planning: Experimental verification of the relation between CT-HU and proton stopping power," *Phys. Med. Biol.*, vol. 43, no. 6, pp. 1579–1592, 1998, doi: 10.1088/0031-9155/43/6/016.
- [100] B. Bruckner, P. M. Wolf, P. Bauer, and D. Primetzhofer, "Impact of the experimental approach on the observed electronic energy loss for light keV ions in thin self-supporting films," *Nucl. Instruments Methods Phys. Res. Sect. B Beam Interact. with Mater. Atoms*, vol. 489, no. January, pp. 82–87, 2021, doi: 10.1016/j.nimb.2020.08.005.
- [101] R. Ishiwari, N. Shiomi, and N. Sakamoto, "Geometrical effect on the measurement of stopping power: Angle-dependent energy loss of 7-MeV protons in metallic and organic thin foils," *Phys. Rev. A*, vol. 25, no. 5, pp. 2524–2528, 1982, doi: 10.1103/PhysRevA.25.2524.
- [102] P. Sigmund and K. B. Winterbon, "Small-Angle Multiple Scattering of Ions in the Screened Coloumb Region," *Nucl. Instruments Methods*, vol. 119, pp. 541–557, 1974.
- [103] P. Sigmund and A. Schinner, "Note on measuring electronic stopping of slow ions," *Nucl. Instruments Methods Phys. Res. Sect. B Beam Interact. with Mater. Atoms*, vol. 410, pp. 78–87, 2017, doi: 10.1016/j.nimb.2017.08.011.
- [104] C. C. Montanari and P. Dimitriou, "The IAEA stopping power database, following the trends in stopping power of ions in matter," *Nucl. Instruments Methods Phys. Res. Sect. B Beam Interact. with Mater. Atoms*, vol. 408, pp. 50–55, 2017, doi: 10.1016/j.nimb.2017.03.138.
- [105] P. Mertens, "The influence of the polycrystalline structure of thin copper foils on the energy loss of transmitted 300 keV ions," *Thin Solid Films*, vol. 60, no. 3, pp. 313–320, 1979, doi: 10.1016/0040-6090(79)90077-4.
- [106] "H. H. Andersen, J. Bøttiger and H. Knudsen (Eds.), "Ion Beam Analysis" *Proceedings of the Fourth*

- International Conference on Ion Beam Analysis*, ISBN 978-1-4832-2889-1, 1979, Doi <https://doi.org/10.1016/C2013-0-12136-8>.
- [107] R. G. Smeenk et al., "Angle resolved detection of charged particles with a novel type toroidal electrostatic analyser". *Nuclear Instruments and Methods in Physics Research*, 195(3), pp.581-586, 1982.
 - [108] S. Lohmann, R. Holeňák, and D. Primetzhofer, "Trajectory-dependent electronic excitations by light and heavy ions around and below the Bohr velocity," *Phys. Rev. A*, vol. 102, no. 6, 2020, doi: 10.1103/PhysRevA.102.062803.
 - [109] F. Abel et al., "Backscattering study and theoretical investigation of planar channeling processes. I. Experimental results," *Physical Review B*, 12(11), p.4617. 1975.
 - [110] H. F. Krause et al., "Angular distribution of ions axially channeled in a very thin crystal: Experimental and theoretical results," *Phys. Rev. A*, vol. 49, no. 1, pp. 283–299, 1994, doi: 10.1103/PhysRevA.49.283.
 - [111] S. Petrović, L. Miletić, and N. Nešković, "Theory of rainbows in thin crystals: The explanation of ion channeling applied to ions transmitted through a $\langle 100 \rangle$ Si thin crystal," *Phys. Rev. B - Condens. Matter Mater. Phys.*, vol. 61, no. 1, pp. 184–189, 2000, doi: 10.1103/PhysRevB.61.184.
 - [112] M. Mousley, W. Möller, P. Philipp, G. Hlawacek, T. Wirtz, and S. Eswara, "Structural and chemical evolution of Au-silica core-shell nanoparticles during 20 keV helium ion irradiation: a comparison between experiment and simulation," *Sci. Rep.*, vol. 10, no. 1, pp. 1–13, 2020, doi: 10.1038/s41598-020-68955-7.
 - [113] J. C. Overley, R. C. Connolly, G. E. Sieger, J. D. Macdonald, and H. W. Lefevre, "Energy-loss radiography with a scanning MeV-ion microprobe," *Nucl. Instruments Methods Phys. Res.*, vol. 218, no. 1–3, pp. 43–46, 1983, doi: 10.1016/0167-5087(83)90952-3.
 - [114] X. Chen et al., "High-resolution 3D imaging and quantification of gold nanoparticles in a whole cell using scanning transmission ion microscopy," *Biophys. J.*, vol. 104, no. 7, pp. 1419–1425, 2013, doi: 10.1016/j.bpj.2013.02.015.
 - [115] T. Gehrke et al., "Proof of principle of helium-beam radiography using silicon pixel detectors for energy deposition measurement, identification, and tracking of single ions," *Medical physics*, 45(2), pp.817-829, 2018.
 - [116] F. Allegrini et al., "Charge state of ~ 1 to 50 keV ions after passing through graphene and ultrathin carbon foils," *Opt. Eng.*, vol. 53, no. 2, p. 024101, 2014, doi: 10.1117/1.oe.53.2.024101.
 - [117] ZEISS, "Correlative Microscopy in Materials Science," *Essent. Knowl. Briefings*, 2017.
 - [118] B. West, M. I. Bertoni, D. Verebelyi, Z. Holman, and V. Rose, "Correlative X-ray Microscopy Studies of CuIn_{1-x}Ga_xSe₂ Solar Cells," *Arizona State University library.*, 2018, [Online]. Available: https://repository.asu.edu/attachments/201234/content/West_asu_0010E_17907.pdf.
 - [119] X. Y. Chin et al., "Interface passivation for 31.25%-efficient perovskite/silicon tandem solar cells," *Science (80)*, vol. 381, pp. 59–63, 2023, doi: 10.1126/science.adg0091.
 - [120] C. N. S. Kumar et al., "Evaluation of secondary electron intensities for dopant profiling in ion implanted semiconductors: A correlative study combining SE, SIMS and ECV methods," *Semicond. Sci. Technol.*, vol. 36, no. 8, 2021, doi: 10.1088/1361-6641/ac0854.
 - [121] T. Wirtz, O. De Castro, J. N. Audinot, and P. Philipp, "Imaging and Analytics on the Helium Ion Microscope," *Annu. Rev. Anal. Chem.*, vol. 12, pp. 523–543, 2019, doi: <https://doi.org/10.1146/annurev-anchem-061318-115457>.
 - [122] T. Wirtz, P. Philipp, J. N. Audinot, D. Dowsett, and S. Eswara, "High-resolution high-sensitivity elemental imaging by secondary ion mass spectrometry: From traditional 2D and 3D imaging to correlative microscopy," *Nanotechnology*, vol. 26, no. 43, p. 434001, 2015, doi: 10.1088/0957-4484/26/43/434001.

- [123] S. Eswara *et al.*, "A method for quantitative nanoscale imaging of dopant distributions using secondary ion mass spectrometry: An application example in silicon photovoltaics," *MRS Commun.*, vol. 9, no. 3, pp. 916–923, 2019, doi: 10.1557/mrc.2019.89.
- [124] L. Yedra *et al.*, "A correlative method to quantitatively image trace concentrations of elements by combined SIMS-EDX analysis," *J. Anal. At. Spectrom.*, vol. 36, no. 1, pp. 56–63, 2021, doi: 10.1039/d0ja00289e.
- [125] F. Babbe *et al.*, "Vacuum-Healing of Grain Boundaries in Sodium-Doped CuInSe₂ Solar Cell Absorbers," *Adv. Energy Mater.*, vol. 13, no. 17, 2023, doi: 10.1002/aenm.202204183.
- [126] S. De Wolf *et al.*, "Organometallic Halide Perovskites: Sharp Optical Absorption Edge and Its Relation to Photovoltaic Performance," *J. Phys. Chem. Lett.*, vol. 5, no. 6, pp. 1035–1039, Mar. 2014, doi: 10.1021/jz500279b.
- [127] X. Y. Chin, D. Cortecchia, J. Yin, A. Bruno, and C. Soci, "Lead iodide perovskite light-emitting field-effect transistor," *Nat. Commun.*, vol. 6, no. May, pp. 1–9, 2015, doi: 10.1038/ncomms8383.
- [128] S. D. Stranks *et al.*, "Electron-hole diffusion lengths exceeding 1 micrometer in an organometal trihalide perovskite absorber," *Science (80)*, vol. 342, no. 6156, pp. 341–344, 2013, doi: 10.1126/science.1243982.
- [129] T. Jesper Jacobsson *et al.*, "Exploration of the compositional space for mixed lead halogen perovskites for high efficiency solar cells," *Energy Environ. Sci.*, vol. 9, no. 5, pp. 1706–1724, 2016, doi: 10.1039/c6ee00030d.
- [130] O. De Castro *et al.*, "npSCOPE: A New Multimodal Instrument for in Situ Correlative Analysis of Nanoparticles," *Anal. Chem.*, vol. 93, no. 43, pp. 14417–14424, 2021, doi: 10.1021/acs.analchem.1c02337.
- [132] P. Schöppe *et al.*, "Rubidium segregation at random grain boundaries in Cu(In,Ga)Se₂ absorbers," *Nano Energy*, vol. 42, pp. 307–313, 2017, doi: 10.1016/j.nanoen.2017.10.063.
- [133] T. Kuroda, "Development of high current negative ion source," *Fusion Eng. Des.*, vol. 36, no. 1, pp. 143–156, 1997, doi: 10.1016/S0920-3796(97)00019-7.
- [134] R. Hill, P. Blenkinsopp, A. Barber, and C. Everest, "The development of a range of C 60 ion beam systems," *Appl. Surf. Sci.*, vol. 252, no. 19, pp. 7304–7307, 2006, doi: 10.1016/j.apsusc.2006.02.211.
- [135] S. Ogawa, "Helium ion microscopy for low-damage characterization and sub-10 nm nanofabrication," *AAPPS Bull.*, vol. 32, no. 1, 2022, doi: 10.1007/s43673-022-00050-7.
- [136] P. V. D Heide, "Secondary ion mass spectrometry: an introduction to principles and practices," *John Wiley & Sons*, vol. 6, 2014.
- [137] J. N. Audinot, P. Philipp, O. De Castro, A. Biesemeier, Q. H. Hoang, and T. Wirtz, "Highest resolution chemical imaging based on secondary ion mass spectrometry performed on the helium ion microscope," *Reports on Progress in Physics*, vol. 84, no. 10, p. 105901, Aug-2021, doi: 10.1088/1361-6633/ac1e32.
- [138] A. D. Ost, "Investigation of Surface Sputtering and Ionization Processes Under Non-Reactive Light Ion Irradiation: Towards 4D Sims Imaging," *University of Luxembourg.*, 2022, [Online]. Available: <https://orbilu.uni.lu/handle/10993/53899>.
- [139] D. Dowsett and T. Wirtz, "Co-Registered in Situ Secondary Electron and Mass Spectral Imaging on the Helium Ion Microscope Demonstrated Using Lithium Titanate and Magnesium Oxide Nanoparticles," *Anal. Chem.*, vol. 89, no. 17, pp. 8957–8965, 2017, doi: 10.1021/acs.analchem.7b01481.
- [140] L. Scipioni, C. A. Sanford, J. Notte, B. Thompson, and S. McVey, "Understanding imaging modes in the helium ion microscope," *J. Vac. Sci. Technol. B Microelectron. Nanom. Struct.*, vol. 27, no. 6, p. 3250, 2009, doi: 10.1116/1.3258634.
- [141] C. B. Carter and D. B. Williams, "Transmission electron microscopy: Diffraction, imaging, and

- spectrometry"., *Springer Cham.*, ISBN 978-3-319-26651-0 2016, Doi <https://doi.org/10.1007/978-3-319-26651-0>.
- [142] J. Notte IV, R. Hill, S. M. McVey, R. Ramachandra, B. Griffin, and D. Joy, "Diffraction imaging in a He⁺ ion beam scanning transmission microscope," *Microsc. Microanal.*, vol. 16, no. 5, pp. 599–603, 2010, doi: 10.1017/S1431927610093682.
 - [143] S. Tabean *et al.*, "Quantitative nanoscale imaging using transmission He ion channelling contrast: Proof-of-concept and application to study isolated crystalline defects," *Ultramicroscopy*, vol. 233, no. June 2021, p. 113439, 2022, doi: 10.1016/j.ultramic.2021.113439.
 - [144] L. P. Zweifel, I. Shorubalko, and R. Y. H. Lim, "Helium Scanning Transmission Ion Microscopy and Electrical Characterization of Glass Nanocapillaries with Reproducible Tip Geometries," *ACS Nano*, vol. 10, no. 2, pp. 1918–1925, 2016, doi: 10.1021/acs.nano.5b05754.
 - [145] D. Emmrich, A. Wolff, N. Meyerbröcker, J. K. N. Lindner, A. Beyer, and A. Götzhäuser, "Scanning transmission helium ion microscopy on carbon nanomembranes," *Beilstein J. Nanotechnol.*, vol. 12, pp. 222–231, 2021, doi: 10.3762/bjnano.12.18.
 - [146] L. Scipioni, D. C. Ferranti, V. S. Smentkowski, and R. A. Potyrailo, "Fabrication and initial characterization of ultrahigh aspect ratio vias in gold using the helium ion microscope," *J. Vac. Sci. Technol. B, Nanotechnol. Microelectron. Mater. Process. Meas. Phenom.*, vol. 28, no. 6, p. C6P18-C6P23, 2010, doi: 10.1116/1.3517514.
 - [147] D. Emmrich *et al.*, "Nanopore fabrication and characterization by helium ion microscopy," *Appl. Phys. Lett.*, vol. 108, no. 16, 2016, doi: 10.1063/1.4947277.
 - [148] T. J. Woehl, R. M. White, and R. R. Keller, "Dark-Field Scanning Transmission Ion Microscopy via Detection of Forward-Scattered Helium Ions with a Microchannel Plate," *Microsc. Microanal.*, vol. 22, no. 3, pp. 544–550, 2016, doi: 10.1017/S1431927616000775.
 - [149] K. L. Kavanagh, C. Herrmann, and J. A. Notte, "Camera for transmission He⁺ ion microscopy," *J. Vac. Sci. Technol. B, Nanotechnol. Microelectron. Mater. Process. Meas. Phenom.*, vol. 35, no. 6, p. 06G902, 2017, doi: 10.1116/1.4991898.
 - [150] J. Wang, S. H. Y. Huang, C. Herrmann, S. A. Scott, F. Schiettekatte, and K. L. Kavanagh, "Focussed helium ion channeling through Si nanomembranes," *J. Vac. Sci. Technol. B, Nanotechnol. Microelectron. Mater. Process. Meas. Phenom.*, vol. 36, no. 2, p. 021203, 2018, doi: 10.1116/1.5020667.
 - [151] K. L. Kavanagh, A. Bunevich, and M. R. Motapothula, "Transmission Helium Ion Microscopy of Graphene," *arXiv preprint.*, pp. 1–5, 2020, [Online]. Available: <http://arxiv.org/abs/2004.01682>.
 - [152] M. Mousley *et al.*, "Stationary beam full-field transmission helium ion microscopy using sub-50 keV He⁺: Projected images and intensity patterns," *Beilstein J. Nanotechnol.*, vol. 10, pp. 1648–1657, 2019, doi: 10.3762/bjnano.10.160.
 - [153] P. Gratia *et al.*, "The Many Faces of Mixed Ion Perovskites: Unraveling and Understanding the Crystallization Process," *ACS Energy Lett.*, vol. 2, no. 12, pp. 2686–2693, 2017, doi: 10.1021/acsenenergylett.7b00981.
 - [154] W. Gaderbauer *et al.*, "Effects of alloying elements on surface oxides of hot-dip galvanized press hardened steel," *Surf. Coatings Technol.*, vol. 404, no. October, p. 126466, 2020, doi: 10.1016/j.surfcoat.2020.126466.
 - [155] J. F. Ziegler, M. D. Ziegler, and J. P. Biersack, "Nuclear Instruments and Methods in Physics Research B SRIM – The stopping and range of ions in matter (2010)," *Nucl. Inst. Methods Phys. Res. B*, vol. 268, no. 11–12, pp. 1818–1823, 2010, doi: 10.1016/j.nimb.2010.02.091.
 - [156] L. Scipioni, C. A. Sanford, J. Notte, B. Thompson, and S. McVey, "Understanding imaging modes in the helium ion microscope," *J. Vac. Sci. Technol. B Microelectron. Nanom. Struct.*, vol. 27, no. 6, p. 3250, Dec. 2009, doi: 10.1116/1.3258634.

- [157] M. Mousley *et al.*, "Stationary beam full-field transmission helium ion microscopy using sub-50 keV He⁺: Projected images and intensity patterns," *Beilstein J. Nanotechnol.*, vol. 10, no. 1, pp. 1648–1657, Aug. 2019, doi: 10.3762/bjnano.10.160.
- [158] L. Wahlin, "The colutron, a zero deflection isotope separator," *Nuclear instruments and methods.*, vol. 27, no. 1, pp. 55-60, 1964.
- [159] H. Kreckel *et al.*, "A simple double-focusing electrostatic ion beam deflector," *Rev. Sci. Instrum.*, vol. 81, no. 6, 2010, doi: 10.1063/1.3433485.
- [160] M. Mousley, S. Tabean, O. Bouton, Q. H. Hoang, T. Wirtz, and S. Eswara, "Scanning Transmission Ion Microscopy Time-of-Flight Spectroscopy Using 20 keV Helium Ions," *Microsc. Microanal.*, vol. 29, no. 2, pp. 563–573, 2023, doi: 10.1093/micmic/ozac049.
- [161] T. Wirtz, O. De Castro, J.-N. Audinot, and P. Philipp, "Imaging and Analytics on the Helium Ion Microscope," *Annu. Rev. Anal. Chem.*, vol. 12, no. 1, pp. 523–543, Jun. 2019, doi: 10.1146/annurev-anchem-061318-115457.
- [162] FEI company, "User Operation Manual Scios," Edition 9, 2016.
- [163] H. Hofsäss, K. Zhang, and A. Mutzke, "Simulation of ion beam sputtering with SDTrimSP, TRIDYN and SRIM," *Appl. Surf. Sci.*, vol. 310, pp. 134–141, 2014, doi: 10.1016/j.apsusc.2014.03.152.
- [164] A. Mutzke *et al.*, "IPP Report SDTrimSP Version 6.00," *Max-Planck-Institut für Plasmaphys.*, 2019.
- [165] N. Brodusch, H. Demers, and R. Gauvin, "Nanometres-resolution Kikuchi patterns from materials science specimens with transmission electron forward scatter diffraction," vol. 250, no.1, pp. 1–14, 2013, doi: 10.1111/jmi.12007.
- [166] P. W. Trimby *et al.*, "ScienceDirect Characterizing deformed ultrafine-grained and nanocrystalline materials using transmission Kikuchi diffraction in a scanning electron microscope," *Acta Mater.*, vol. 62, pp. 69–80, 2014, doi: 10.1016/j.actamat.2013.09.026.
- [167] P. W. Trimby, "Ultramicroscopy Orientation mapping of nanostructured materials using transmission Kikuchi diffraction in the scanning electron microscope," *Ultramicroscopy*, vol. 120, pp. 16–24, 2012, doi: 10.1016/j.ultramic.2012.06.004.
- [168] M. A. Sortica, M. K. Linnarsson, D. Wessman, S. Lohmann, and D. Primetzhofer, "A versatile time-of-flight medium-energy ion scattering setup using multiple delay-line detectors," *Nucl. Instruments Methods Phys. Res. Sect. B Beam Interact. with Mater. Atoms*, vol. 463, no. June 2019, pp. 16–20, 2020, doi: 10.1016/j.nimb.2019.11.019.
- [169] M. K. Linnarsson, A. Hallén, J. Åström, D. Primetzhofer, S. Legendre, and G. Possnert, "New beam line for time-of-flight medium energy ion scattering with large area position sensitive detector," *Rev. Sci. Instrum.*, vol. 83, no. 9, 2012, doi: 10.1063/1.4750195.
- [170] R. G. Smeenk, R. M. Tromp, H. H. Kersten, A. J. H. Boerboom, and F. W. Saris, "Angle resolved detection of charged particles with a novel type toroidal electrostatic analyser," *Nucl. Instruments Methods*, vol. 195, no. 3, pp. 581–586, 1982, doi: 10.1016/0029-554X(82)90022-2.
- [171] W. Dabrowski, "Radiation damage in Si detectors and front-end electronics," *Nucl. Phys.*, vol. 44, pp. 150–175, 1902.
- [172] Q. Su *et al.*, "Helium Irradiation and Implantation Effects on the Structure of Amorphous Silicon Oxycarbide," *Sci. Rep.*, vol. 7, no. 1, pp. 1–8, 2017, doi: 10.1038/s41598-017-04247-x.
- [173] S. Gavarini *et al.*, "Effects of helium irradiation on fine grained β -SiC synthesized by spark plasma sintering," *J. Eur. Ceram. Soc.*, vol. 40, no. 1, pp. 1–11, 2020, doi: 10.1016/j.jeurceramsoc.2019.09.018.
- [174] K. Nordlund, M. Ghaly, and R. S. Averback, "Mechanisms of ion beam mixing in metals and semiconductors," *J. Appl. Phys.*, vol. 83, no. 3, pp. 1238–1246, 1998, doi: 10.1063/1.366821.
- [175] K. Nordlund, M. Ghaly, and R. Averback, "Defect production in collision cascades in elemental

- semiconductors and fcc metals," *Phys. Rev. B - Condens. Matter Mater. Phys.*, vol. 57, no. 13, pp. 7556–7570, 1998, doi: 10.1103/PhysRevB.57.7556.
- [176] L. J. García, Y. Kawamura, M. Uematsu, J. M. Hernández-Mangas, and K. M. Itoh, "Monte Carlo simulation of silicon atomic displacement and amorphization induced by ion implantation," *J. Appl. Phys.*, vol. 109, no. 12, pp. 0–5, 2011, doi: 10.1063/1.3592256.
 - [177] G. R. N. Defoort-Levkov, A. Bahm, and P. Philipp, "Influence of water contamination on the sputtering of silicon with low-energy argon ions investigated by molecular dynamics simulations," *Beilstein J. Nanotechnol.*, vol. 13, pp. 986–1003, 2022, doi: 10.3762/bjnano.13.86.
 - [178] J. Nord, K. Nordlund, and J. Keinonen, "Amorphization mechanism and defect structures in ion-beam-amorphized Si, Ge, and GaAs," *Phys. Rev. B - Condens. Matter Mater. Phys.*, vol. 65, no. 16, pp. 1–14, 2002, doi: 10.1103/PhysRevB.65.165329.
 - [179] A. Lopez-Cazalilla, A. Ilinov, K. Nordlund, and F. Djurabekova, "Modeling of high-fluence irradiation of amorphous Si and crystalline Al by linearly focused Ar ions," *J. Phys. Condens. Matter*, vol. 31, no. 7, 2019, doi: 10.1088/1361-648X/aaf59f.
 - [180] J. L. Murray, "The Al-Ga (Aluminum-Gallium) system," *Bull. Alloy Phase Diagrams*, vol. 4, no. 2, pp. 183–190, 1983, doi: 10.1007/BF02884877.
 - [181] R. W. Olesinski, N. Kanani, and G. J. Abbaschian, "The Ga-Si (Gallium-Silicon) system," *Bull. Alloy Phase Diagrams*, vol. 6, no. 4, pp. 362–364, 1985, doi: 10.1007/BF02880523.
 - [182] S. Estreicher, J. Weber, A. Derecskei-Kovacs, and D. Marynick, "Noble-gas-related defects in Si and the origin of the 1018 meV photoluminescence line," *Phys. Rev. B - Condens. Matter Mater. Phys.*, vol. 55, no. 8, pp. 5037–5044, 1997, doi: 10.1103/PhysRevB.55.5037.
 - [183] R. Li *et al.*, "Study of damage generation induced by focused helium ion beam in silicon," *J. Vac. Sci. Technol. B*, vol. 37, no. 3, p. 031804, 2019, doi: 10.1116/1.5096908.
 - [184] K. L. Wilson and G. J. Thomas, "Low-energy helium implantation of aluminum," *J. Nucl. Mater.*, vol. 63, no. C, pp. 266–272, 1976, doi: 10.1016/0022-3115(76)90337-8.
 - [185] O. Girka, O. Bizyukov, S. Bogatyrenko, and I. Bizyukov, "Aluminium surface morphology behaviour under high-flux helium ion bombardment," *Nucl. Instruments Methods Phys. Res. Sect. B Beam Interact. with Mater. Atoms*, vol. 405, pp. 31–35, 2017, doi: 10.1016/j.nimb.2017.05.019.
 - [186] A. Hedler, S. Klaumünzer, and W. Wesch, "Swift heavy ion irradiation of amorphous silicon," *Nucl. Instruments Methods Phys. Res. Sect. B Beam Interact. with Mater. Atoms*, vol. 242, no. 1–2, pp. 85–87, 2006, doi: 10.1016/j.nimb.2005.08.101.
 - [187] L. Frank and J. N. Pi, "About the information depth of backscattered electron imaging," vol. 00, no. 0, pp. 1–8, 2017, doi: 10.1111/jmi.12542.
 - [188] R. Van Bremen, D. R. Gomes, L. T. H. De Jeer, V. Ocelík, and J. T. M. De Hosson, "Ultramicroscopy On the optimum resolution of transmission-electron backscattered diffraction (t-EBSD)," *Ultramicroscopy*, vol. 160, pp. 256–264, 2016, doi: 10.1016/j.ultramic.2015.10.025.
 - [189] K. Nordlund, "Large fraction of crystal directions leads to ion channeling," *Physical Review B* 94,. vol. 214109, no.21, 2016, doi: 10.1103/PhysRevB.94.214109.
 - [190] R. Holeňák, S. Lohmann, and D. Primetzhofer, "Sensitive multi-element profiling with high depth resolution enabled by time-of-flight recoil detection in transmission using pulsed keV ion beams," *Vacuum*, vol. 204, June, 2022, doi: 10.1016/j.vacuum.2022.111343.
 - [191] E. P. Bellido, A. Manjavacas, Y. Zhang, Y. Cao, P. Nordlander, and G. A. Botton, "Electron Energy-Loss Spectroscopy of Multipolar Edge and Cavity Modes in Silver Nanosquares," *ACS Photonics*, vol. 3, no. 3, pp. 428–433, 2016, doi: 10.1021/acsp Photonics.5b00594.
 - [192] R. Blume, W. Eckstein, and H. Verbeek, "Electronic energy loss of H, D and He in Au below 20 keV," *Nucl. Instruments Methods*, vol. 168, no. 1–3, pp. 57–62, 1980, doi: 10.1016/0029-554X(80)91231-8.

- [193] E. Ntemou, R. Holeňák, and D. Primetzhofer, "Energy deposition by H and He ions at keV energies in self-supporting, single crystalline SiC foils," *Radiat. Phys. Chem.*, vol. 194, no. November 2021, pp. 0–4, 2022, doi: 10.1016/j.radphyschem.2022.110033.
- [194] S. Datz, C. D. Moak, T. S. Noggle, B. R. Appleton, and H. O. Lutz, "Potential-energy and differential-stopping-power functions from energy-loss spectra of fast ions channeled in gold single crystals," *Phys. Rev.*, vol. 179, no. 2, pp. 315–326, 1969, doi: 10.1103/PhysRev.179.315.
- [195] C. D. Archubi, J. C. Eckardt, G. H. Lantschner, and N. R. Arista, "Angular effects in the energy loss of slow protons and helium ions transmitted through thin Al and Au films," *Phys. Rev. A - At. Mol. Opt. Phys.*, vol. 73, no. 4, pp. 1–6, 2006, doi: 10.1103/PhysRevA.73.042901.
- [196] E. A. Figueroa, E. D. Cantero, J. C. Eckardt, G. H. Lantschner, M. L. Martiarena, and N. R. Arista, "Energy loss versus exit angle for H⁺ and He⁺ ions channeled in Au 100 at very low energies, and observation of a molecular effect for incident H₂⁺," *Phys. Rev. A - At. Mol. Opt. Phys.*, vol. 78, no. 3, pp. 1–9, 2008, doi: 10.1103/PhysRevA.78.032901.
- [197] M. Famá, G. H. Lantschner, J. C. Eckardt, C. D. Denton, and N. R. Arista, "Energy-angle distribution of low-energy hydrogen ions in thin aluminum and gold foils," *Nucl. Instruments Methods Phys. Res. Sect. B Beam Interact. with Mater. Atoms*, vol. 164, pp. 241–249, 2000, doi: 10.1016/S0168-583X(99)01086-1.
- [198] A. Mutzke *et al.*, "SDTrimSP Version 6.00," *IPP Report Max Planck Insitut fur Plasmaphysik*, 2019-02 pp. 1–92, 2019.
- [199] R. Nucl, L. Phase, L. F-, and S. Cedex, "Centre de Recherches Nucl~aires, Laboratoire PHASE, 23, rue du Loess F-67037 Strasbourg Cedex, France," vol. 20, pp. 501–506, 1987.
- [200] K. Inai, K. Ohya, and T. Ishitani, "Simulation study on image contrast and spatial resolution in helium ion microscope," *J. Electron Microsc. (Tokyo).*, vol. 56, no. 5, pp. 163–169, 2007, doi: 10.1093/jmicro/dfm024.
- [201] J. Notte *et al.*, "An introduction to the helium ion microscope," *AIP Conf. Proc.*, vol. 931, pp. 489–496, 2007, doi: 10.1063/1.2799423.
- [202] G. H. Bernstein, A. D. Carter, and D. C. Joy, "Do SEI electrons really degrade SEM image quality?," *The Journal of Scanning Microscopies*, vol. 35, no. 1, pp. 1–6, 2013, doi: 10.1002/sca.21027.
- [203] A. K. W. Chee and S. A. Boden, "Dopant profiling based on scanning electron and helium ion microscopy," *Ultramicroscopy*, vol. 161, pp. 51–58, 2016, doi: 10.1016/j.ultramic.2015.10.003.
- [204] E. Peiner, A. Schlachetzki, and D. Krüger, "Doping Profile Analysis in Si by Electrochemical Capacitance-Voltage Measurements," *J. Electrochem. Soc.*, vol. 142, no. 2, pp. 576–580, 1995, doi: 10.1149/1.2044101.
- [205] B. Sermage *et al.*, "Electrochemical capacitance voltage measurements in highly doped silicon and silicon-germanium alloys," *J. Appl. Phys.*, vol. 119, no. 15, 2016, doi: 10.1063/1.4946890.
- [206] F. G. Allen and G. W. Gobeli, "Work function, photoelectric threshold, and surface states of atomically clean silicon," *Phys. Rev.*, vol. 127, no. 1, pp. 150–158, 1962, doi: 10.1103/PhysRev.127.150.
- [207] F. Sahli *et al.*, "Fully textured monolithic perovskite/silicon tandem solar cells with 25.2% power conversion efficiency," *Nat. Mater.*, vol. 17, no. 9, pp. 820–826, 2018, doi: 10.1038/s41563-018-0115-4.
- [208] F. Sahli *et al.*, "Improved Optics in Monolithic Perovskite/Silicon Tandem Solar Cells with a Nanocrystalline Silicon Recombination Junction," *Adv. Energy Mater.*, vol. 8, no. 6, pp. 1–8, 2018, doi: 10.1002/aenm.201701609.
- [209] J. Warby *et al.*, "Understanding Performance Limiting Interfacial Recombination in pin Perovskite Solar Cells," *Adv. Energy Mater.*, vol. 12, no. 12, pp. 1–10, 2022, doi: 10.1002/aenm.202103567.
- [210] T. Wang, J. D. A. Ng, E. W. Y. Ong, K. H. Khoo, and Z. K. Tan, "The Role of Subsurface Valence Band

- Localization in the Passivation of Perovskite Nanocrystals,” *Adv. Opt. Mater.*, vol. 10, no. 3, pp. 1–6, 2022, doi: 10.1002/adom.202101914.
- [211] P. Tockhorn *et al.*, “Nano-optical designs for high-efficiency monolithic perovskite–silicon tandem solar cells,” *Nat. Nanotechnol.*, vol. 17, no. 11, pp. 1214–1221, 2022, doi: 10.1038/s41565-022-01228-8.
- [212] T. Song, D. J. Friedman, and N. Kopidakis, “Comprehensive Performance Calibration Guidance for Perovskites and Other Emerging Solar Cells,” *Adv. Energy Mater.*, vol. 11, no. 23, pp. 1–16, 2021, doi: 10.1002/aenm.202100728.
- [213] G. E. Eperon, S. D. Stranks, C. Menelaou, M. B. Johnston, L. M. Herz, and H. J. Snaith, “Formamidinium lead trihalide: a broadly tunable perovskite for efficient planar heterojunction solar cells,” *Energy Environ. Sci.*, vol. 7, no. 3, pp. 982–988, 2014, doi: 10.1039/C3EE43822H.
- [214] S.-H. Turren-Cruz, A. Hagfeldt, and M. Saliba, “Methylammonium-free, high-performance, and stable perovskite solar cells on a planar architecture,” *Science*, vol. 362, no. 6413, pp. 449–453, Oct. 2018, doi: 10.1126/science.aat3583.
- [215] H. Lu *et al.*, “Vapor-assisted deposition of highly efficient, stable black-phase FAPbI₃ perovskite solar cells,” *Science (80)*, vol. 370, no. 6512, p. eabb8985, 2020, doi: 10.1126/science.abb8985.
- [216] D. P. McMeekin *et al.*, “A mixed-cation lead mixed-halide perovskite absorber for tandem solar cells,” *Science (80)*, vol. 351, no. 6269, pp. 151–155, 2016, doi: 10.1126/science.aad5845.
- [217] W. Shockley and H. J. Queisser, “Detailed Balance Limit of Efficiency of p-n Junction Solar Cells,” *J. Appl. Phys.*, vol. 32, no. 3, pp. 510–519, Mar. 1961, doi: 10.1063/1.1736034.
- [218] T. Zhang *et al.*, “Profiling the organic cation-dependent degradation of organolead halide perovskite solar cells,” *J. Mater. Chem. A*, vol. 5, no. 3, pp. 1103–1111, 2017, doi: 10.1039/C6TA09687E.
- [219] D. H. Kim *et al.*, “300% Enhancement of Carrier Mobility in Uniaxial-Oriented Perovskite Films Formed by Topotactic-Oriented Attachment,” *Adv. Mater.*, vol. 29, no. 23, pp. 1–8, 2017, doi: 10.1002/adma.201606831.
- [220] O. J. Weber *et al.*, “Phase Behavior and Polymorphism of Formamidinium Lead Iodide,” *Chem. Mater.*, vol. 30, no. 11, pp. 3768–3778, 2018, doi: 10.1021/acs.chemmater.8b00862.
- [221] R. E. Beal *et al.*, “Cesium Lead Halide Perovskites with Improved Stability for Tandem Solar Cells,” *J. Phys. Chem. Lett.*, vol. 7, no. 5, pp. 746–751, Mar. 2016, doi: 10.1021/acs.jpclett.6b00002.
- [222] K. P. McKenna, “Electronic Properties of {111} Twin Boundaries in a Mixed-Ion Lead Halide Perovskite Solar Absorber,” *ACS Energy Lett.*, vol. 3, no. 11, pp. 2663–2668, Nov. 2018, doi: 10.1021/acsenenergylett.8b01700.
- [223] W. Li *et al.*, “The critical role of composition-dependent intragrain planar defects in the performance of MA1–xFAxPbI₃ perovskite solar cells,” *Nat. Energy*, vol. 6, no. 6, pp. 624–632, 2021, doi: 10.1038/s41560-021-00830-9.
- [224] L. Oesinghaus *et al.*, “Toward Tailored Film Morphologies: The Origin of Crystal Orientation in Hybrid Perovskite Thin Films,” *Adv. Mater. Interfaces*, vol. 3, no. 19, 2016, doi: 10.1002/admi.201600403.